REPORT DOCUMENTATION PAGE

Form Approved
OMB NO. 0704-0188

1. AGENCY USE ONLY (Leave Blank)	2. REPORT DATE 04/10/2003	3. REPORT TYPE AND DATES COVERED Final Progress Report: 07/01/1998-04/30/2002

4. TITLE AND SUBTITLE
Development of a Solid-State Microhydraulic Energy Harvesting Mechanism for Heel Strike Power Harvesting

5. FUNDING NUMBERS
DAAG55-98-1-0361

6. AUTHOR(S)
J. Lodewyk Steyn and Nesbitt W. Hagood IV

7. PERFORMING ORGANIZATION NAME(S) AND ADDRESS(ES)

8. PERFORMING ORGANIZATION REPORT NUMBER

9. SPONSORING / MONITORING AGENCY NAME(S) AND ADDRESS(ES)

U. S. Army Research Office
P.O. Box 12211
Research Triangle Park, NC 27709-2211

10. SPONSORING / MONITORING AGENCY REPORT NUMBER

38980.1-CH

11. SUPPLEMENTARY NOTES
The views, opinions and/or findings contained in this report are those of the author(s) and should not be construed as an official Department of the Army position, policy or decision, unless so designated by other documentation.

12 a. DISTRIBUTION / AVAILABILITY STATEMENT

Approved for public release; distribution unlimited.

12 b. DISTRIBUTION CODE

13. ABSTRACT (Maximum 200 words)

A Microhydraulic Transducer (MHT) device was developed with the goal of extracting energy from heel strike motion. The required power output is approximately 1W, with an associated power density of approximately 0.1-1kW/kg. The MHT relies on the incorporation of discrete piezoelectric elements into a microfabricated device to produce compact, high stiffness actuation at high frequencies. These piezoelectric elements, in conjunction with a piezoelectric piston, enable the design of a stiff, efficient fluidic to electric energy conversion mechanism with high power density. Using this mechanism in combination with hydraulic amplification, piezoelectric hydraulically amplified valves were produced that made it possible to create pulsing fluid pressure on a piezoelectric piston, and hence extract electrical power. The device relies on the DRIE fabrication of high-strength silicon membranes to form pistons with membrane tethers. These pistons are the moving elements of the device. A final device was built and tested, with a maximum power output of 1mW measured from the piezoelectric piston at a differential pressure of 450kPa. Good agreement with models was obtained and, although the device tested had a design limitation unaccounted for in the original modeling, future devices based on this concept should be able to reach the original design goals.

14. SUBJECT TERMS
Piezoelectric, Energy Harvesting, Microvalve, Hydraulic Amplification, Silicon Membrane, Silicon-on-Insulator (SOI), Die-Level Bonding, Heel Strike Power Generation, MicroElectroMechanical Systems (MEMS), Power MEMS, Active Valve, Fluid Filling, Microhydraulic Transducer (MHT), Deep Reactive Ion Etch (DRIE).

15. NUMBER OF PAGES
152 (w/out reprints/appendix)
1471 (with reprints/appendix)

16. PRICE CODE

17. SECURITY CLASSIFICATION OR REPORT UNCLASSIFIED	18. SECURITY CLASSIFICATION ON THIS PAGE UNCLASSIFIED	19. SECURITY CLASSIFICATION OF ABSTRACT UNCLASSIFIED	20. LIMITATION OF ABSTRACT UL

NSN 7540-01-280-5500

Standard Form 298 (Rev.2-89)
Prescribed by ANSI Std. 239-18
298-102

Enclosure 1

20030509 087

Development of a Solid-State Microhydraulic
Energy Harvesting Mechanism
for Heel Strike Power Harvesting

FINAL REPORT

Acknowledgments

Contents

List of Figures

List of Tables

1 Introduction

1.1 Objective

Currently, many research efforts around the world are underway to develop compact liquid micropumping systems, the term "micro" referring to devices which are created with fabrication procedures capable of μm-size tolerances and which produce overall micropump dimensions on the order of a few millimeters to a few centimeters. However, the vast majority of these systems are designed for low pressure and low flow rate applications [1] [2] [3] [4] [5] such as drug dispensing and microdosing [6] [7] [8]. The higher performing of these systems are capable of pumping liquids with flow rates on the order of $1000 - 3000\mu l/min$ $(0.017 - 0.050ml/s)$ against differential pressures of between 10kPa and 50kPa. With a typical device mass on the order of ~1 gram, these performance values correlate to device-level specific powers below $2.5W/kg$.

This research program at MIT has worked toward the development of high specific power micropumping technology (with specific powers $\sim 100 - 1000W/kg$). In order to realize this technology, which can be used for compact actuation systems, as well as for compact power generation applications (ie: for heel-strike power generation), a novel class of Micro-Hydraulic Transducer (MHT) devices has been introduced [9] [10] [11] [12] [13]. These devices combine bulk piezoelectric materials with stiff micro-machined structural elements and are designed to enable high frequency pumping of fluid (10-20kHz) against pressure differentials on the order of $\sim 1 - 2MPa$, creating flow rates near or in excess of $1ml/s$.

1.2 Motivation

Piezoelectric materials are well-suited for transducer applications because of their inherently high peak specific powers. Figure 1 provides a comparison of the single stroke specific energy (J/Kg), bandwidth (kHz), and theoretical peak specific power (W/kg) for a variety of transducer materials [14] [15] [16]. The product of a material's single stroke specific energy and its bandwidth provides a value for the material's specific power (W/kg). Shape-memory alloy materials (denoted SMA), for example, possess a relatively large single stroke specific work $(\sim 5000J/kg)$ in comparison to that of standard polycrystalline piezoelectric materials such as PZT-5H $(\sim 10J/kg)$. The maximum operational frequency, or bandwidth $(\sim 10Hz)$, of SMA materials, however, is significantly less than that of standard piezoelectrics $(\sim 100kHz)$. SMA materials and standard piezoelectrics both possess specific powers near $100W/kg$, however, their optimal implementation as actuation mechanisms is far different. In an application where low frequency, large stroke actuation is desired (such as an on-off microvalve), the use of an SMA material might be preferred over a standard piezoelectric material. Conversely, for an application whereby high frequency, low stroke actuation is required, a piezoelectric material may be preferred. In fact, for this reason, the vast majority of high frequency micropumping systems use piezoelectric materials as their actuation mechanism in conjunction with fast-acting valves. The recent development of single-crystal ferroelectric materials (e.g. PZN-PT), characterized by specific powers approaching $10kW/kg$ (~100x greater than those of standard polycrystalline PZT materials) [17], offers further advantages in strain capability over the standard piezoelectrics. These high performing materials, however, have yet to be integrated within high frequency micropumping systems.

The piezoelectric micropumping devices and systems that have been presented in the literature up until this time typically utilize one of two actuation methods as a means to pump fluid: either (1) a deposited thin-film, thick disk, or bimorph of piezoelectric material [2] [3] [6] in contact with a compliant membrane, or (2) a direct-drive stack actuator in contact with a moveable silicon diaphragm. The thin-film, thick-film, and bimorph structural designs presented are not conducive to both high force and high-frequency operation. The direct-drive stack actuation designs [18] [19] [20] are capable of achieving
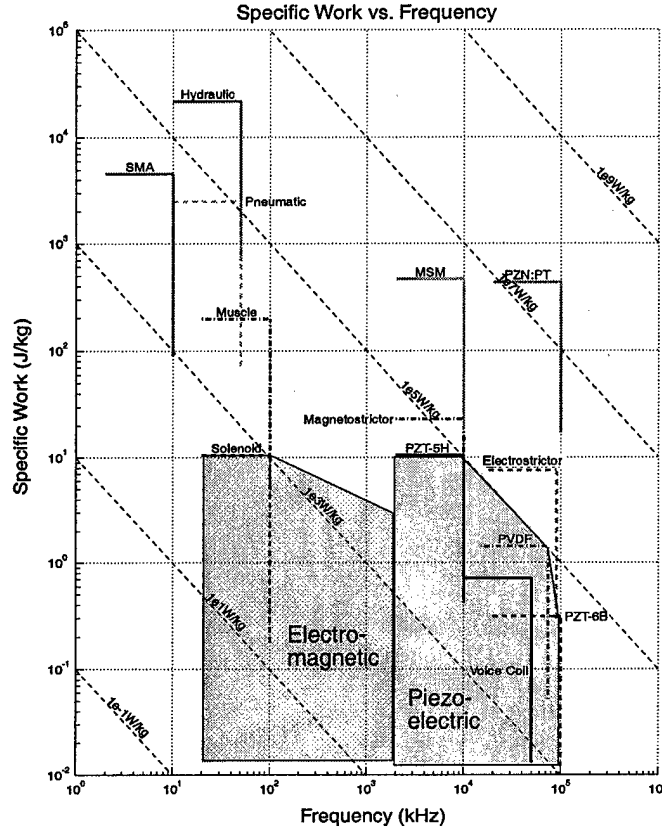
Figure 1: Upper bound on specific work vs. frequency for various actuation media. SMA is shape-memory alloy; PZN-PT is single-crystal piezoelectric; MSM is magnetic shape memory materials.

higher frequency operation than the thin-film, thick-film, and bimorph designs, however the presented micropump devices using these designs are limited in their flow rate, pressurization, and frequency capabilities due to inadequacies of the accompanying one-way passive valves used to regulate the fluid flow. Additionally, these previously presented direct-drive stack designs require a significant length of piezoelectric actuation material to create the deflection and fluid pumping volume required for reasonable fluid flow rates. Due to this significant actuator size, an epoxy bonding agent and a relatively compliant silicon diaphragm are required to tolerance the piezoelectric material within the structures. The key design feature which differentiates Micro-Hydraulic Transducer devices from these previous piezoelectric micropumps is the incorporation of a stiff micromachined structural "piston-like" actuation element not only within the pumping chamber of the device, but also within accompanying flow regulation active valves. The annularly-tethered micromachined "piston" structure, driven by miniature bulk piezoelectric elements (almost an order of magnitude smaller than those used in [18] [19] [20]) attached using a thin-film eutectic alloy bond, can achieve structural frequencies well above 10kHz and can actuate against fluid pressurizations near 1MPa. The implementation of such a stiff structure within fluidic systems can enable significantly higher frequency and pressurization capabilities than the previously presented

piezoelectric micropumps.

As shown in Figure 2, a Micro-Hydraulic Transducer system consists of a piezoelectric pump chamber, two actively controlled valves, and a low and high pressure fluid reservoir. In the MHT actuator, electrical energy supplied to the piezoelectric pump chamber results in a pumping of fluid through the valves from the low to high pressure reservoir. In the MHT power harvester, sequenced operation of the valves results in fluid flow from the high to low pressure reservoir, producing a "pinging" of the piezoelectric element within the pump chamber. This cyclic strain on the element induces electrical charge, which can be rectified and stored. For power harvesting operation, active valves are essential. For actuating (pumping operation), they are beneficial and also allows for bi-directional pumping. The specific power of these transducer devices scales linearly with the frequency of operation and the pressure drop across which the device can operate. Since structural frequencies scale inversely with the geometric size of the device, it is advantageous to build these systems as small as possible, hence the need for MEMS fabrication and process technologies.
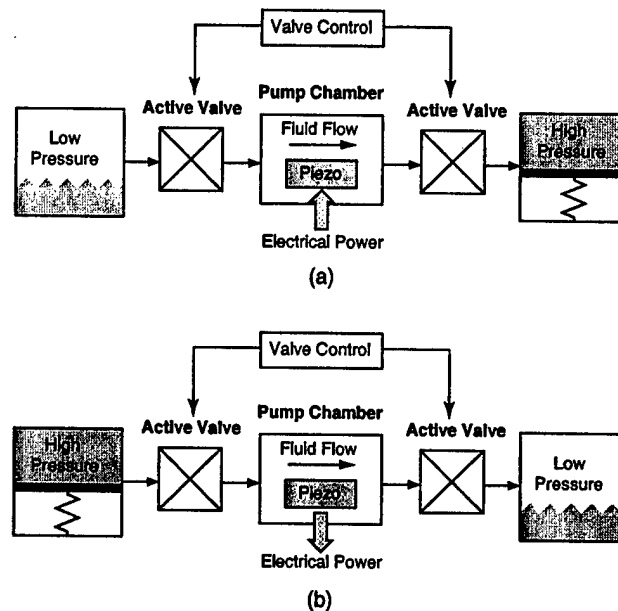
Figure 2: Schematics of Micro-Hydraulic Transducer systems: (a) MHT actuator system, (b) MHT power harvesting system. High specific power is achieved through the integration of piezoelectric material with structural stiff small-scale hydraulic systems.

1.3   The MHT Chip-Level Harvesting Device

In Section 1.2 a few basic functional requirements were implied for an MHT device:

- A piezoelectric pumping and generating chamber, with its piston attached to a piezoelectric element

- Two compact high frequency valves. These valves have to be actively controlled.

14

- Connection to two external reservoirs - a high pressure reservoir or HPR, and a low pressure reservoir or LPR.

A device to satisfy these requirements was built under this project. The completed device is shown in Figure 3. The result is a 9-layer device combining four microfabricated silicon layers with precision piezoelectric elements and five ultrasonically machined glass layers.

(a)   (b)
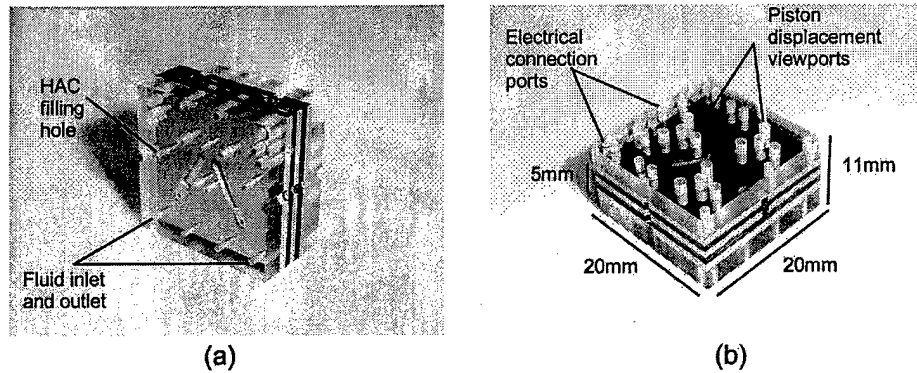
Figure 3: Photograph of a 9-layer silicon and glass chip-level MHT device. Dimensions of the device: 20mm x 20mm x 10mm.

A 3-D schematic of the MHT generator system, illustrating individual silicon and glass layers, is shown in Figure 4. The middle glass layer (Layer 3) forms the drive element support structure and the top (Layer 9 - not shown) and bottom (Layer 1 - not shown) glass layers provide structural support. The bottom silicon layer (Layer 2) and drive piston silicon layers (Layers 4,5) provide a path for electrical contact to the piezoelectric cylinders in each of the two active valves and within the harvesting chamber. The top four silicon layers (Layers 4,5,7,8) and glass layer (Layer 6) house the hydraulic amplification chamber (within the valves), valve cap and membrane structure, and fluid inlet and outlet channels. All silicon-silicon wafer interfaces are bonded with high-temperature ($\sim$1100^{o}C) fusion bonds, and all silicon-glass layer interfaces are bonded using low temperature ($\sim$300^{o}C) anodic bonds. Attachment of the top and bottom piezoelectric cylinder surfaces to the adjoining silicon is achieved with a low temperature ($\sim$300°C) AuSn eutectic bond.

1.3.1 The Active Valves - Enabling Power Generation

The performance of these MHT systems is directly governed by the capabilities of the active valves, which regulate flow into and out of the pump chamber. As a result, to achieve high specific power Micro-Hydraulic Transducer devices, a compact high frequency, high pressure active valve is required. The microvalve subcomponent is shown schematically in Figure 5. This device is desired to achieve large valve cap stroke (up to $\sim$40μm) against high pressure loads ($\sim$1-2MPa) through a novel hydraulic amplification mechanism that converts the small displacement ($\sim$1μm) of a piezoelectric material element into a significantly larger valve cap stroke. The inherent stiffness of the piezoelectric material and the hydraulic fluid chamber enable both high-frequency and high-force actuation capabilities.

The active valve consists of three primary components: a piezoelectric drive element, an enclosed fluid amplification chamber, and a membrane with attached valve cap. The drive element incorporates a circular piston structure supported from beneath by one or more small bulk piezoelectric cylinders and

15

3D Schematic View

Low Pressure   High Pressure

Valve Cap

Hydraulic
Amplification
Chamber

Piezoelectric
Material

Active Valve   Pump Chamber   Active Valve

—Silicon (Layer 8)
—Silicon (Layer 7)
—Glass   (Layer 6)
—Silicon (Layer 5)
—Silicon (Layer 4)
—Glass   (Layer 3)
—Silicon (Layer 2)

3D Sectional View
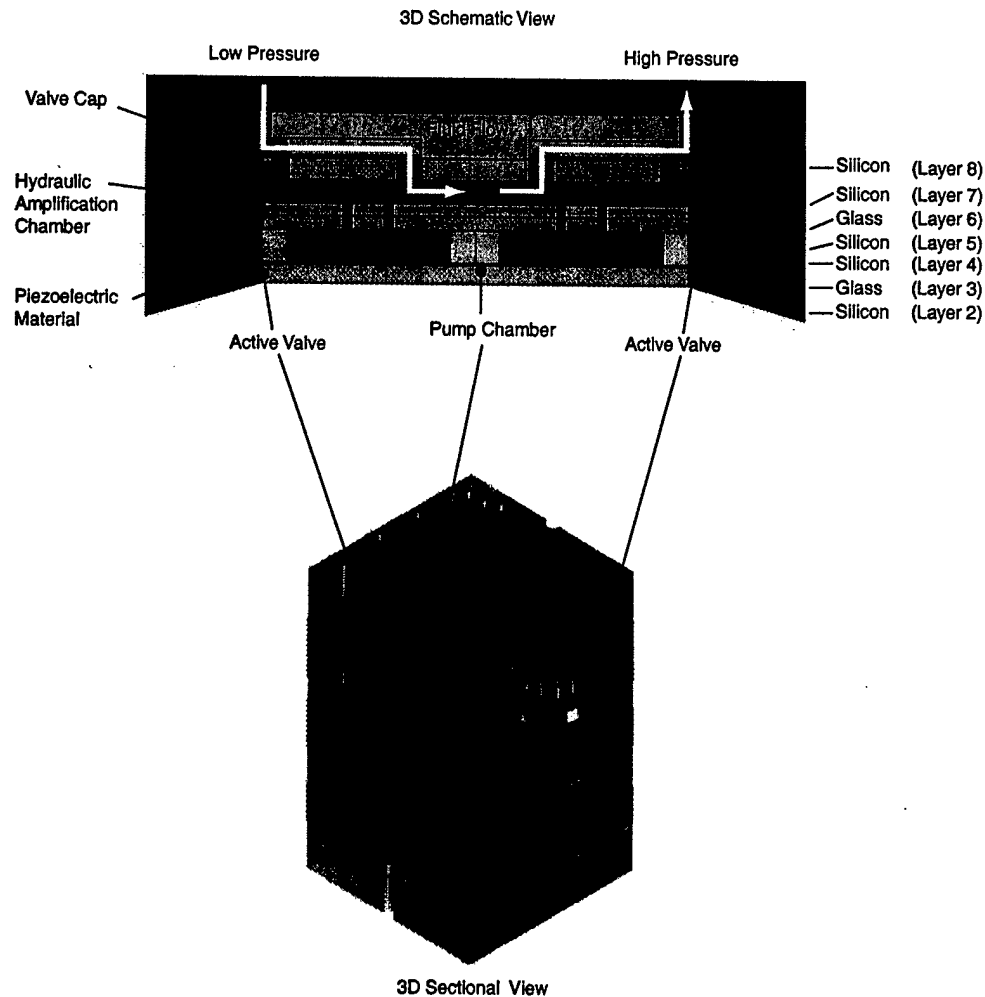
Figure 4: 3-D schematic of a Micro-Hydraulic Transducer multi-layer silicon and glass structure. Shown are both a linear 2D schematic and also a 3D section view of the device.

is suspended circumferentially from a surrounding support structure by thin annular micromachined tethers. This novel compact "piston-type" design enables high frequency actuation against a large external pressurization due to the high stiffness of the piston structure and integration of miniature bulk piezoelectric elements beneath the piston using a thin-film bond layer. The lateral dimensions of the tethers are designed to make the tethers compliant enough to allow for rigid piston motion up and down, yet stiff enough to resist bowing under pressurization caused by the hydraulic fluid above the tether during actuation. The tethers provide a seal between the hydraulic fluid above the piston and the piezoelectric chamber below the piston, and also provide a path for electrical contact to the top surface of the piezoelectric cylinders. The fluid chamber resides between the top surface of the drive element piston and the bottom surface of a thin, smaller diameter silicon micromachined valve cap membrane.

16
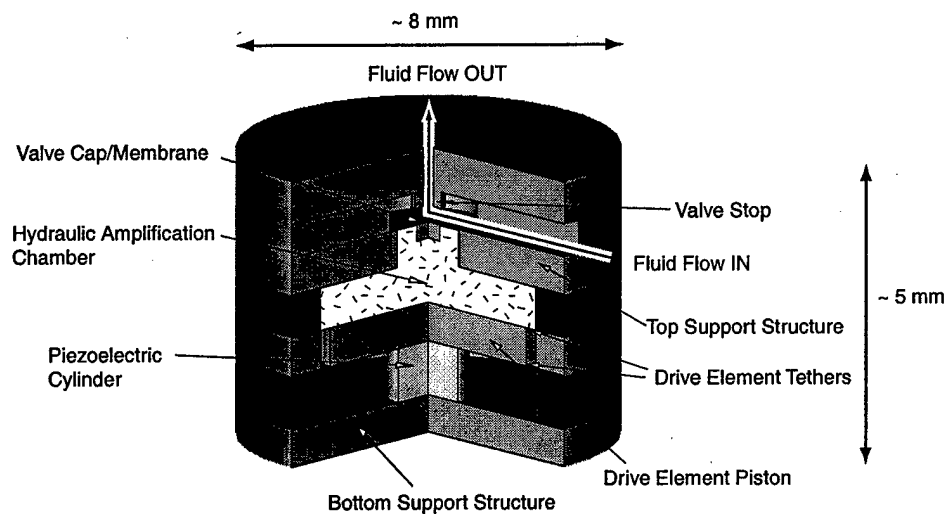
Figure 5: Schematic of a piezoelectrically-driven hydraulic amplification microvalve. The primary structural components are designated with arrows. External hydraulic system pressure loading is applied on the top surface of the valve cap and membrane.

In response to applied piezoelectric voltage, the piezoelectric material strains. The resulting deflection of the drive element piston generates a pressure within the hydraulic amplification chamber which in turn deflects the valve cap and membrane against a fluid orifice, thereby regulating fluid flow through the external hydraulic system. The pressure loadings on the valve cap and membrane during device operation depend on the external microfluidic system application. The piezoelectric material capabilities, the ratio of the piston diameter to the valve membrane diameter, the compliances of the fluid and structural elements in the chamber, the severity to which the valve cap membrane experiences nonlinear behavior, and the nature of the external loading all contribute to the performance of this microvalve device.

1.3.2   Features of the MHT Design

We now highlight more detailed design features of the MHT device. Some of these features will be discussed in further detail in later sections of this report. Using Figures 6 and 7 for reference, the following features were incorporated in the MHT device:

1. Pin contact for anodic bonding of Layer 3.

2. Viewport for displacement measurement of the piston.

3. Electrical contact (hole for spring pin contact) to piston layer.

4. Clearance in Layer 2 to prevent electrical short to contact to Layer 4. Also sufficient to prevent arcing.

5. Pin contact to Pyrex Layer 3 for anodic bonding.

17

6. Electrical pin contact to Layer 2.

7. Additional anodic bonding hole

8. Anodic bonding contact to SOI layer of layer 5 for bonding to Layer 6. (Eventually contacting Layer 4 was found to be sufficient for this design.

9. Piston membrane tethers. Proper design of these membranes for both strength and deflection was critical. Each device has six of these membranes attached to its three piezoelectrically driven pistons.

10. Piezoelectric piston. This particular one drives one of the active valves.

11. Piezo seat. These recesses, of order $20\mu m$ deep, were individually etched to accommodate different size piezoelectric elements.

12. Electrical isolation trench in Layer 2. All three pistons were fully isolated and were thus capable of being supplied with "ungrounded" power. This was a requirement for the central harvesting piston, which would be floating.

13. Electrical isolation trench in Layers 4 and 5. This forms the other side of the electrical isolation of the piezoelectric piston assembly. Note also that Layer 6 is a glass layer, thus preventing capacitive coupling to Layers 7 and 8, that are grounded.

14. Piezo recess clearance in the Pyrex. Recesses were ultrasonically machined for every piezoelectric element, simplifying pick-and-place positioning.

15. Piezoelectric element. Only one piezoelectric element per piston is shown in this schematic. All MHT devices had three piezoelectric elements per piston, for a total of nine per device.

16. Shallow recess in glass Layer 3, to allow piston motion.

17. Vent channels between Layers 4 and 5. This is to prevent a sealed cavity from forming during the fusion bonding process.

18. Inlet pressure sensing membrane. This membrane was to be used to sense dynamic pressure of the device inlet, and was machined in Layer 7.

19. Flow inlet (or outlet - the device was symmetric and bi-directional).

20. Entrance to the valve. Flow experiments have shown that the nature of the entrance "step" into the poppet valve has a significant effect on the flow losses through it.

21. Valve seat. The seat width was also designed for minimum pressure drop.

22. Valve outlet channel.

23. Valve cap (central boss). This cross-sectional schematic depicts the harvesting device with 10 dicrete valve caps per active valve unit, for a total of 20 per device. In addition, devices with one and two valve units were also microfabricated. Only the single valve devices were tested. Theoretically, a valve with 10 valve caps promised low pressure drops. Reliable fabrication of these membranes proved to be challenging.

24. Valve membrane tether.

25. Transfer port from Hydraulic Amplification Chamber (HAC) to valve cap.

26. Hydraulic Amplification Chamber. This was ultrasonically machined into Layer 6.

27. HAC filling port.

28. Main chamber.

29. Main chamber pressure sensor.

30. Outlet flow channel.

31. High frequency sealing channel for the hydraulic amplifier.

32. Central valve support. Care had to be taken to ensure the rigidity of this support. The compliance of the HAC had to be minimized to ensure proper amplification.

33. Flow outlet.

34. Outlet pressure sensor.

35. Electrical contact (pin contact) for anodic bonding of Layer 7 and 8 to Layer 9. (This hole was eventually deemed to be redundant.)

36. Electrical contact for anodic bonding of Layer 4 to Layer 3.
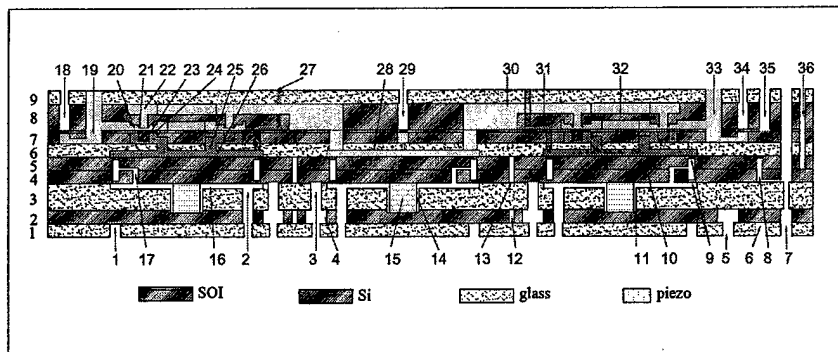
Figure 6: Cross-section schematic of the MHT device, highlighting major design features of the device.

1.4 Research Program Challenges

A significant number of challenges had to be overcome to realize a functional MHT system. These challenges, which can be organized into two major groupings: (1) modeling and design challenges and (2) fabrication, assembly, and testing challenges, are briefly introduced in this section and covered in detail in the remainder of this report.

1.4.1 Modeling and Design Challenges

The design philosophy for the MHT device was driven by requirements to produce a high power density, high performance, compact, energy generating device. As such, the design approach had to address the following issues and challenges. More attention will be given to these topics in Section 2.1:

19
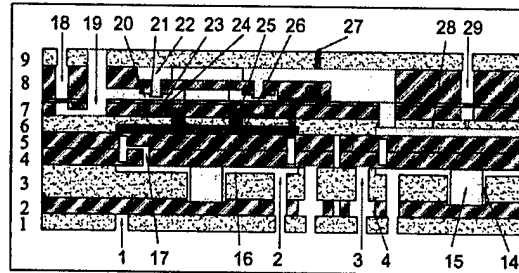
Figure 7: Cross-section schematic of the MHT device - a detail view.

Design for Manufacturability To design the MHT device, care had to be taken to ensure that the initial conceptual design was manufacturable using MEMS fabrication techniques. Where needed, enhancements could made to existing fabrication technologies. Although new technologies and techniques were developed under this project that were particular to the MHT device, the majority of the silicon and glass layer fabrication relied on previously developed Deep Reactive Ion Etch (DRIE) and ultrasonic machining technolgies. The same care had to be taken with the final design, to ensure that the device features were of dimensions that were manufacturable and not, for example, excessively fragile.

Design for Performance Perfomance of the device was of utmost importance. Therefore, many features of this device, structural, fluidic and electrical, were driven by a need to produce a well-performing MHT device. As in many MEMS devices there existed a strong coupling between the structural, fluidic and electrical energy domains, which required careful modeling to enable a design for maximal performance to be obtained.

Design for Reliability and Strength Hand in hand with performance came additional stresses on the materials used in the device, mainly silicon, glass, and the piezoelectric material of choice. working with these brittle materials at high stress levels presented unique challenges when trying to ensure that a reliable device was designed.

Design Refinement and Optimization The MHT device, as a complex, coupled system demanded that attention be given to the modeling strategies, to ensure that the system-level simulations could be done quickly and effectively.

1.4.2 Device Fabrication, Assembly, and Testing Challenges

Micromachining and Wafer-Bonding Micromachining of the valve membrane and drive element tether structures within the MHT device is a critical step in the fabrication process. To achieve precise dimensional control of these thin-membrane structures, silicon-on-insulator (SOI) wafers containing a buried oxide etch-stop layer are used. In performing deep etches in these wafers, the surface roughness of the etch and the tailoring of the fillet radius profiles at the base of the etch must be well-controlled so as to maintain the strength and robustness of the structures. Additionally, upon completing the etching of the various silicon layers, wafer-level silicon-silicon fusion bonding and wafer-level silicon-glass anodic bonding procedures must be carried out to form multi-layer wafer stack structures, in preparation for device assembly.

20

Piezoelectric Material Integration Integration of bulk piezoelectric material within the thin-tethered drive element structures is the most critical step in the MHT assembly. Preparation of the material, including polishing, thin-film deposition, and core-drilling, is performed to provide an optimal surface finish of the material in preparation for eutectic bonding to the adjoining silicon layers within the device. Additionally, accurate measurement of the individual piezoelectric element dimensional thicknesses, prior to integration, is required to ensure optimal static and operational deflections of the piston structure which result in minimal stresses in the etched piston tethers. Incorporation of multiple smaller area piezoelectric materials spread out beneath the piston membrane is desired over placement of a single larger area piezoelectric material at the piston center, so as to reduce system compliances and increase actuation efficiency. However, tolerance issues become even more important when dealing with the requirements of multiple bonded elements.

Fluid Filling and Sealing Encapsulation of a working fluid in the device is a significant challenge at the microscale because surface-to-volume ratios are typically quite large, with surface energies playing a dominant role. Any gas bubbles present in the sealed active valves can create enormous system compliances, potentially rendering the system useless. The elimination of trapped gases during filling of the device and during encapsulation of the fluid port used for filling is critical for high-level performance. The development of a systematic fluid degassing and filling procedure is required for successful realization of a working active valve device.

Device Testing Experimental testing of a complex microfabricated device can be an extremely challenging activity, due primarily to the lack of physical access to the structures within the device. To thoroughly characterize the performance of the MHT system, drive element piston and valve cap deflections in response to applied voltages must be measured real-time. Additionally, dynamic pressures (between 0 and 2 MPa) upstream and downstream of the valve orifice and real-time fluid flow rates (as low as 10 $\mu L/min$ and as high as 1 ml/s) must be monitored. Development of a test-rig apparatus for carrying out these measurements is a critical task for proper evaluation of the device behavior.

1.5   Research Program Sub-Component Development Plan

A detailed sub-component testing plan for the MHT system is presented in Figure 8. This plan breaks the MHT systems into manageable sub-component structures according to the primary challenges already detailed. The piezoelectric drive element sub-component study proves the ability to micromachine the tethered piston structure and integrate bulk piezoelectric material beneath the piston structure of the active valves and harvesting chamber. The valve cap and membrane sub-component study validates the deflection behavior of the valve membrane structures contained within the active valves. The successful completion of these sub-component studies enables realization of the active valve system components. All of the fabrication and assembly challenges inherent in the realization of the active valve component structures are shared by the full MHT device, and as a result this sub-component testing plan enables step-by-step development of complete MHT systems.

Schematic Cross-Sections of Test Articles in the Test Plan

Sub-Component Study:
Valve Cap and Membrane

Sub-Component Study:
Piezoelectric Drive Element

Sub-Component Study:
Hydraulic Amplification Chamber

Sub-Component Study:
Active Valve

High
Pressure

Low
Pressure

Full MHT Device Testing
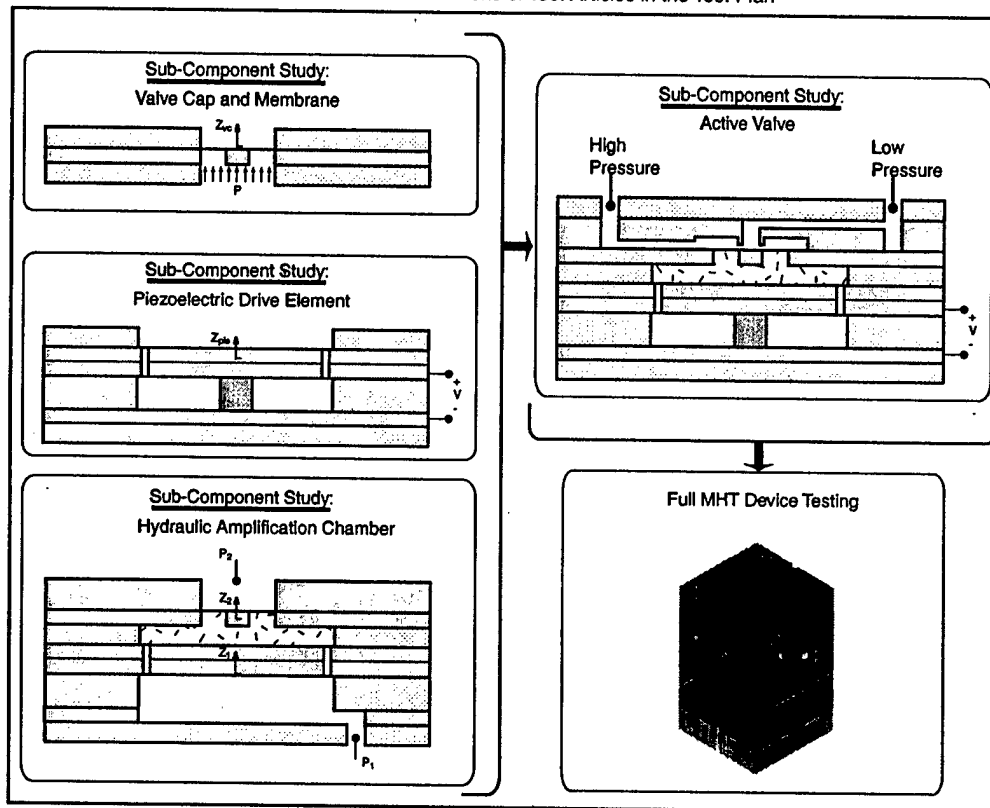
Figure 8: MHT sub-component testing plan. Realization of the full MHT system requires performance validation of piezoelectric drive element sub-component, valve cap and membrane sub-component, and active valve sub-component.

2 System Design and Modeling

Section 1 introduced the concept of the MHT system which, when operated in an energy harvesting mode of operation, can be summarized into the following main components:

- The MHT device itself. At the heart of the MHT system is the MHT device, manufactured using a combination of microfabrication and conventional fabrication techniques.

- The energy harvesting circuitry.

- The drive electronics for the active valves.

- The heel packaging system, made by conventional fabrication techniques.

The work described in this report focused primarily on the MHT device itself, with this component being by far the most challenging to design and manufacture. The design of this device was therefore approached in a systematic fashion, and this section deals with both the general approach and though process that resulted in the design of the MHT device, as well as a discussion of the simulation tools that were developed to produce the final design.

2.1 Approach to the design of the MHT device

We will now expand on the basic elements of the design process as described in Section 1.4.1. Presented here is a more detailed discussion of the design approach that led to the MHT device with the features as described in Section 1.3.2. This process is also represented schematically in Figure 9. Throughout this discussion, for references to items numbers and layers, the reader is referred back to Figures 6 and 7.
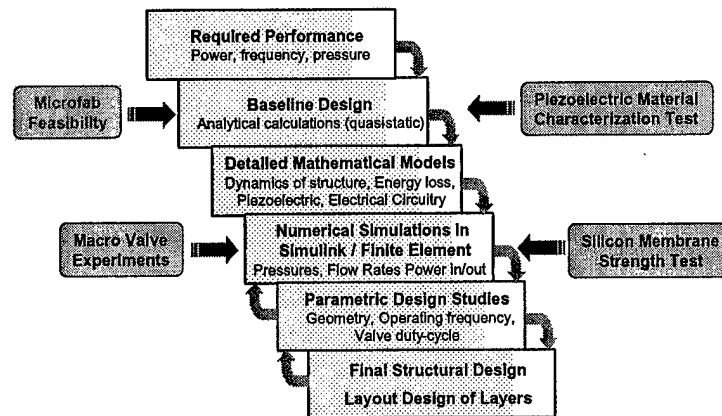
Figure 9: MHT Design procedure.

Design for Manufacturability Throughout the design procedure, manufacturability was a key consideration and determined, to a large extent, the layout and structure of the MHT device. What resulted was number of features that were mentioned in Section 1.3.2, and are discussed here in more detail.

23

1. Deep Reactive Ion Etching (DRIE) of silicon substrates. Using DRIE, which yields, in most instances, reliable "extruded" features, simplified mask layout and etching process development.

2. Ultrasonic machining for glass layers. Reliable, but limited in its capability to produce small features, ultrasonic machining was nonetheless chosen as the means for shaping the glass layers. All critical dimensions were therefore limited to the silicon layers.

3. Silicon-glass sandwich structure enabling die-level anodic bonding. By having been able to assemble devices on a one-by-one basis, it was possible to significantly increase the yield during the prototype development stage. Although this method is not desirable for large-scale production, it served well to yield devices that could be tested for performance.

4. Minimum thickness of SOI layers. The minimum thickness of the SOI layers was deemed to be $7\mu m$ and this was then also the specified thickness for the valve membranes.

5. Recessed ultrasonic machining to make piezo alignment "pockets". By providing pockets in Layer 3 for aligning the piezoelectric elements, the "pick-and-place" assembly was greatly simplified.

6. Holes for anodic bonding. Spread throughout the device were holes for bonding almost any layer to any other layer, therefore giving various options for making electrical contact during assembly.

7. Individually etched piezo recesses. Due to unavoidable height variations in the piezoelectric elements, Layer 2 was designed to be etched on a die-by-die basis. Eventually, to obtain the desired depths, part-die masking was used to tailor individual piezo recesses. This procedure, once again, enabled the fabrication of prototype devices but is not desirable for mass production.

Design for Performance The following features in the design resulted primarily from an attempt to enhance the performance of the MHT device:

1. Double layer, double-tethered drive piston. This feature increases the first natural frequency of the drive piston. In addition, the stiffer piston provides for a less compliant chamber and hence a better performing device. See Section 6.2.

2. Stiff structure in general. The entire device was designed such that it would be sufficiently stiff to ensure that a minimal amount of energy is stored elastically, enabling maximum power transfer between the piezoelectric elements and the fluid.

3. Optimized stiffness of the membrane tether structures. As the most compliant members in the device, their flexibility contributed to a large extent to the compliance of the device, and as such had to be minimized, bearing in mind that a stiffer membrane would deflect less, giving less motion for a valve. It would also see higher stresses for a given deflection. This study is discussed in Section 2.2.7.

4. Pump chamber and hydraulic amplification chamber height of approximately $200\mu m$. This was found to be the lowest height that would not cause severe squeeze film damping effects.

5. Multiple valves instead of one large valve. This gives more flow area for a given valve opening, with less flow losses. This feature proved challenging to fabricate.

6. Three piezoelectric elements instead of a single one. Once again, to stiffen the system and raise the structural natural frequencies. Using this type of tripod configuration also ensured that the first vibrational mode of the piston, a tilt mode, was eliminated.

24

7. Deep electrical isolation trenches in Layer 2 and the Layer 4-5 pair. Electrical isolation was achieved during the dicing operation. This yielded a device with three fully isolated piezoelectric drive units.

8. In conjunction with the deep isolation trenches, by making Layers 1, 3 and 6 from glass, capacitive coupling to ground is minimized, and maximum power can be harvested from the piezo. The alternative, using the buried oxide layers of the SOI wafers, is a much less attractive alternative.

9. Flow channel geometries chosen to exploit fluidic resonant behavior at the design frequency. Helmholtz resonator models were used.

10. Small sealing channels for dynamically sealing the hydraulic amplification units. These channels eliminated the need for a static seal for the prototype MHT devices. This allowed for the pressurization of the hydraulic amplification chambers to balance them with respect to the high and low pressure reservoirs.

11. The use of single crystal PZN-PT piezoelectric material for its superior electromechanical conversion capabilities.

12. The use of a low-viscosity ($0.65cst$) silicone oil with good silicon wetting properties reduced viscous losses in the device.

Design for Reliability and Strength The following steps, in terms of design and supporting investigations were taken to ensure that the final device would be reliable and functional:

1. Bonded SOI wafers ensure the use of single crystal device layers to form membranes of uniform thickness. (SOI wafers made using the SIMOX[1] process were found to be inadequate.)

2. Carefully controlled fillet radii at the bottom of the trenches that formed the membranes. This ensured reduced stress concentrations which allowed the membrane-piston structures to operate at larger deflections. The geometry of the fillet radii was specified after a set of membrane strength tests, described in Section 3.4, to ensure that the maximum stress in any tether structure does not exceed $1GPa$ under the assembly and operating conditions of the device. For the valve membranes, this stress would be encountered during operation where the valves would deflect as much as $15\mu m$ for the single valve devices and $10\mu m$ for the ten-valve devices, experiencing fluid pressures as high as $2MPa$. For the pistons, this stress would be seen during assembly, and also during the poling step for the piezoelectric material. The combined oversizing of the piezoelectric elements and the additional deflection during poling could add up to as much as $8\mu m$, with the expected tolerances that were to be attained.

3. Determining the maximum stress limits of the piezoelectric materials to prevent compressive depolarization. (See Section 3.3)

Design Refinement and Optimization The remainder of Section 2 will address the design refinement procedure which took place whilst giving consideration to aspects of manufacturability, performance, reliability, strength and functionality.

---

[1]SIMOX: Separation by the IMplantation of OXygen
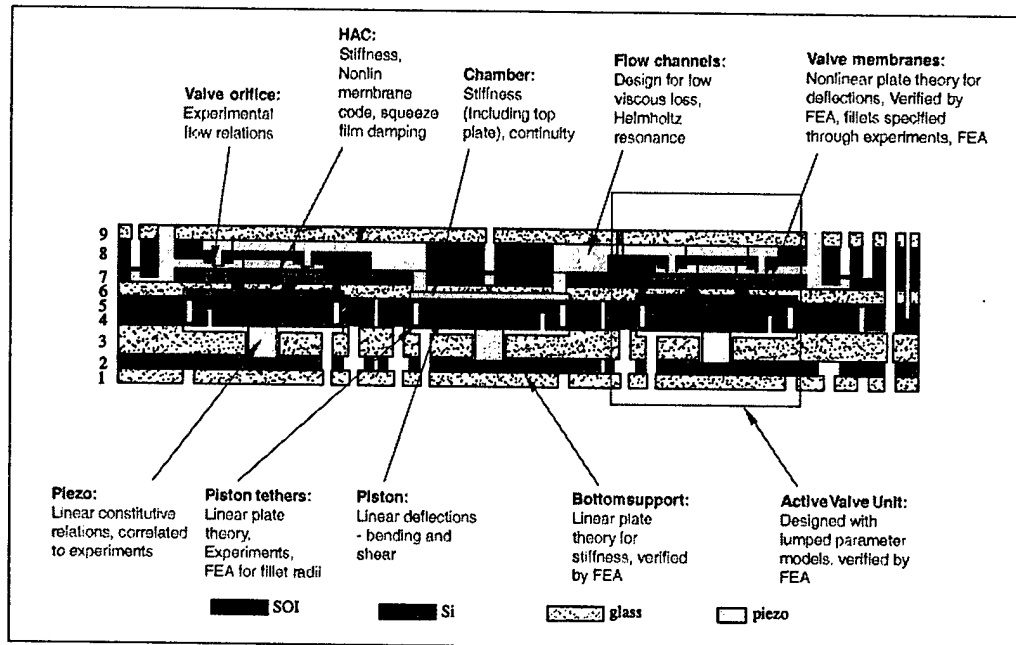
Figure 10: Main aspects of the modeling performed on the MHT device.

2.2 Development of Simulation Tools

2.2.1 Objective

Given the complexity of MHT devices, comprehensive simulation tools were needed to produce a good design. Operation of each subcomponent of the device was coupled to the others and every design decision had to be made with remaining components in mind. In this case the approach was to create a system level simulation tool that enabled the monitoring of important parameters such as chamber pressure, flowrate, and various structural component deflections and stresses. This tool also combined the different energy domains, namely fluidic, structural, piezoelectric material and electrical (circuitry). The system level simulation tool was supplemented by more detailed modeling and experimental methods in the following ways (See also Figure 10):

- Microscale fluid flow - by means of experimental investigations.

- Detailed finite element analysis of the structural components - the pistons, tethers and also the entire active valve unit.

- Including the nonlinear membrane behavior in the model using lookup tables to reduce the computational overhead.

Figure 11 depicts the entire system level simulation approach. For the purposes of designing the MHT device, most emphasis was placed on the "chip level simulation", and the Low Pressure Reservoir (LPR) and High Pressure Reservoir (HPR) were taken as constant pressure sources. In addition, the valve drive electronics were not incorporated explicitly, but the harvesting electronics were.

26
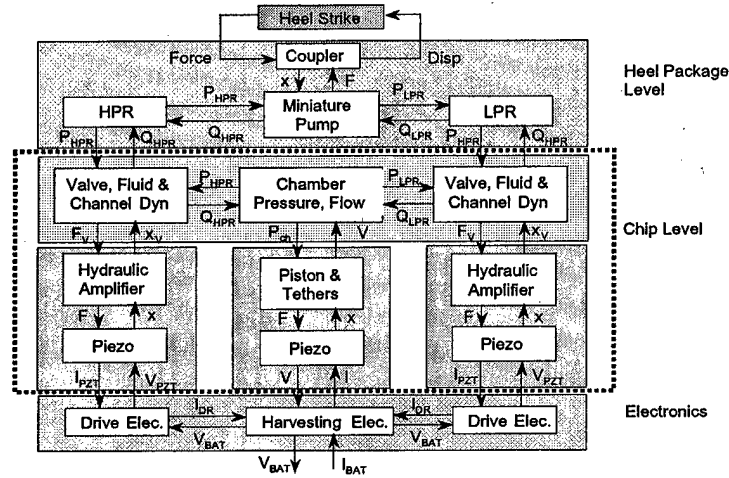
Figure 11: Energy harvester system simulation schematic.

2.2.2 Piezoelectric Power Generation

Piezoelectric materials are mostly used as sensors and actuators. Since they are capable of electromechanical energy conversion and some have high coupling coefficients, which is an indication of the efficiency of the electromechanical energy conversion, they can be also used as power generators from ambient vibration or impact energy, and as structural vibration dampers. The idea and the governing principles are the same for power generation and structural vibration damping, using piezoelectric elements and passive circuit elements. The coupling between mechanical and electrical domains provided by the piezoelectric effect allows the damping mechanism to be implemented as electrical circuit elements rather than physical masses, springs and dampers. Most of the discussions which are valid for the structural damping applications with piezoelectric elements are valid for the power generation from ambient vibration or impact energy with piezoelectric elements. In both cases, the purpose is to transfer as much energy from the mechanical to the electrical domain. The transferred energy to the electrical domain can be either dissipated or stored. If a piezoelectric element is shunted with a resistor or with a resistor and inductor network, the converted electrical energy is dissipated. However, if the piezoelectric element is connected to a rectifier circuit, a diode bridge for example, with a capacitor or battery, the converted electrical energy can be stored.

Circuitry Considerations In the literature various mechanisms for piezoelectric power generation have been presented and some studies were performed on piezoelectric material characterization for power generation. However, no detailed analysis has been presented in terms of effective coupling factor, energy density and piezoelectric material comparison. This section analyzes the diode bridge rectifier circuit for rectifying and storing the electrical energy generated by the piezoelectric element. This circuit constitutes one of the simplest examples of nonlinear shunting of piezoelectric elements.

The piezoelectric element is modeled using linear piezoelectric constitutive relationships. The governing equations for the diode bridge are derived using Kirchoff's laws and diode equations.

27

(a) Full Bridge Rectifier   (b) Full Bridge Rectifier and Voltage Detector
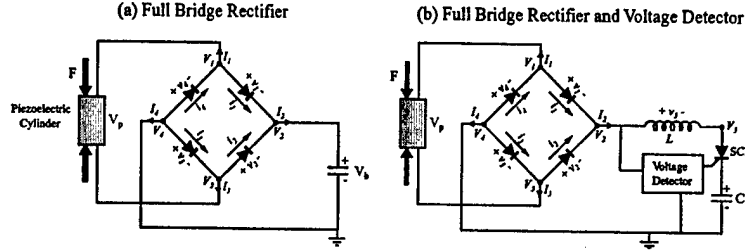
Figure 12: Diode bridge rectifier.

Analysis The operation at steady state can be summarized as follows: During the compression of the piezoelectric element the voltage across its terminals increases. When it reaches the battery voltage, current starts to flow through the battery. The amount which the piezoelectric element voltage exceeds the battery voltage during this interval depends on the diode properties and other resistances in the system. When the force on the piezoelectric element starts decreasing, the voltage decreases along with it and when it becomes less than the battery voltage, current stops flowing through the battery. As the force on the piezoelectric element keeps decreasing, the voltage on the piezoelectric elements keep decreasing until it reaches the negative value of the battery voltage. At this point, current begins to flow through the battery, now, however, from a different branch of the diode bridge. Again, during this interval the voltage on the piezoelectric element exceeds the battery voltage a little bit (in this case it is lower than the negative value of the battery voltage). When the force starts increasing, the voltage starts increasing too and again no current flows through the battery. Throughout the operation, the voltage on the piezoelectric element fluctuates between the negative and positive values of the battery voltage.

In order to obtain insight into the energy conversion mechanism and to derive the governing equations it is worthwhile to look at the force-deflection plots of the piezoelectric element, which are obtained from the simulation of the piezoelectric element attached to the diode bridge. These are plotted in Figure 13. The most important observation is that there are two major regimes during the operation: Operation under open circuit conditions, where the compliance of the piezoelectric element is small, i.e. the piezoelectric element is hard; and operation under closed circuit conditions, where the compliance of the piezoelectric element is large, i.e. the piezoelectric element is soft. The compliances in these regimes are s_{33}^D and s_{33}^E for open circuit and closed circuit conditions respectively. The shaded region in Figure 13 corresponds to the stored electrical energy in one cycle. The generated power is then simply this energy times the operation frequency.

The generated power by the piezoelectric element can be expressed as:

$$W = \frac{1}{4}(s_{33}^E - s_{33}^D)\sigma^2 V_p f \tag{1}$$

where V_p is the volume of the piezoelectric element and f is the operation frequency. From the above equation it can be seen that the power depends heavily on the stress on the piezoelectric element, which suggests that the power will heavily depend on the pressure band in the energy harvesting chamber. The most important limitation on piezoelectric power generation is the depolarization stress. For stresses larger than this, piezoelectric element coefficients degrade and performance decreases drastically. Each piezoelectric element has a different depolarization stress, which constitute an important factor when determining their feasibility as power generators.

28
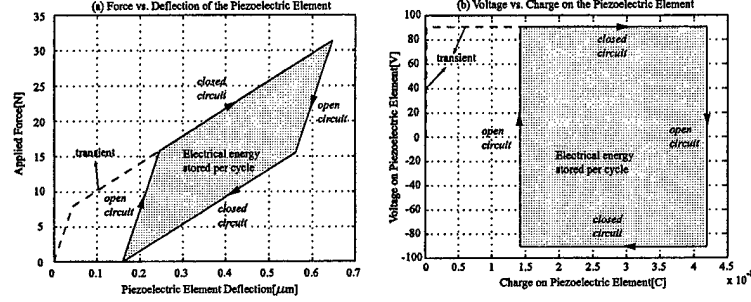
Figure 13: Force vs. Deflection of the piezoelectric element under cyclic compression attached to diode bridge rectifier.

2.2.3 The Energy Harvesting Chamber

The Energy Harvesting Chamber (EHC) consists of a fluid chamber, a piston and a piezoelectric cylinder. The piston converts the pressure in the chamber to a force on the piezoelectric cylinder. The inlet and outlet valves operate $180°$ out of phase at high frequency and convert the static pressure differential $(P_{HPR} - P_{LPR})$ into pressure fluctuations in the chamber. This results in cyclic compression of the piezoelectric cylinder, which is coupled to the circuitry. The generic operation and typical duty cycles are shown in Figure 14.

In the chamber, the hydraulic energy is converted into mechanical energy, which is converted into electrical energy in the piezoelectric element and then the electrical energy is stored in the battery. A strong coupling exists between the hydraulic/mechanical system and the circuitry. The electrical circuit affects the behavior of the system - an aspect which was analyzed in detail.

Figure 15 shows the structural components and the corresponding deformations which were used in the formulations of the governing equations. These deformations inside the energy harvesting chamber can be adequately represented by linear plate theory [36]. Each component is modeled as a plate with applied loading and boundary conditions to determine the deflections and swept volumes. In general, a symmetrically loaded circular plate will experience deflections due to bending as well as shearing. Since the radii of the structural components analyzed were significantly larger than the corresponding thicknesses, deformations only due to bending will be considered.

The equation governing the chamber continuity is:

$$P_{ch} = \frac{\beta_f}{V_o} \left(\int_0^t (Q_{in} - Q_{out}) dt + \Delta V_{pis} + \Delta V_{pb} + \Delta V_{te} - \Delta V_{tp} \right) \tag{2}$$

where ΔV_{pis}, ΔV_{pb}, ΔV_{te}, ΔV_{tp} represent the swept volume due to the motion of the piston, deformation of the piston, deformation of the top tether and deformation of the top support structure respectively.

The elastic equations along with the chamber continuity equation and piezoelectric element constitutive relationships are solved in Maple and the coefficients required by the simulation architecture is calculated and fed to Simulink. The simulation architecture allows for integration of the elastic equations into the dynamic simulations as well as for monitoring important parameters like deflections and swept volumes of the individual structural components and stresses in the tethers.

29
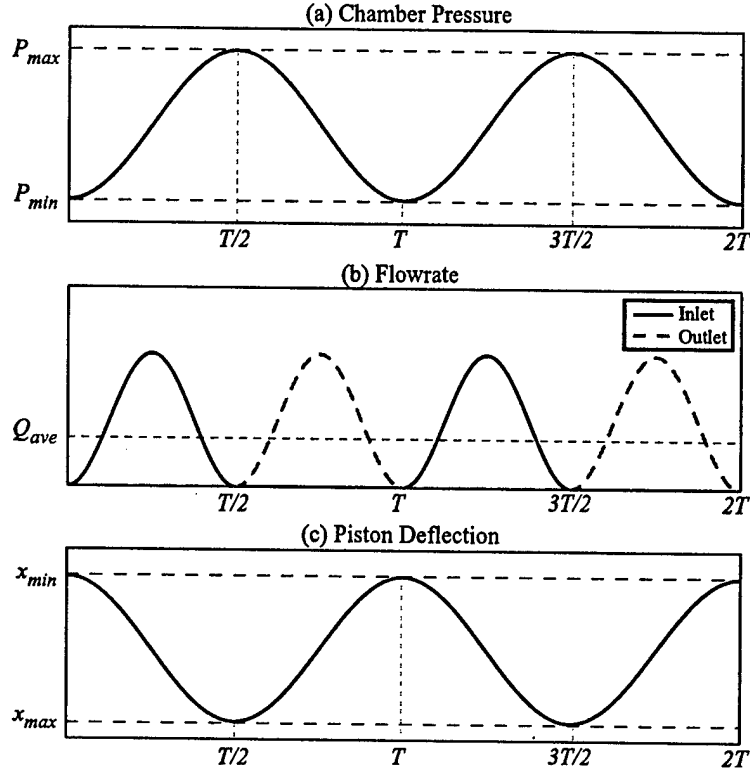
Figure 14: Duty cycles of generic operation of the energy harvesting chamber. The valve openings have the same duty cycle as the flowrates and are not shown here.

2.2.4 Active Valve

The layout of the active valve is shown in Figure 16. The active valve structural components are modeled similarly using linear plate theory, with the exception of the valve membranes, whose deformation is nonlinear and a numerical code is used to calculate the deformation and stress of the membrane. The nonlinearity of the membrane structure is incorporated into the system level simulation using look-up tables that are generated using the numerical code by running it for different pressure loading conditions on the active valve membrane. The simulink architecture of the active valve is shown in Figure 17.

2.2.5 Fluid Models

The schematic of the device with pressures at different locations within the system is shown in Figure 18 where P_{int-in} is the intermediate pressure at the exit of the inlet channel, and $P_{int-out}$ is the intermediate pressure at the entrance to the outlet valve. Inlet and outlet channels have the same geometry.

Valve Orifice Flow Relations Work by previous researches has shown that for small openings, poppet valves, such as the valve cap in the active valves within the MHT systems, behave as long orifices in which the effects of flow separation and subsequent re-attachment dominate the valve flow dynamics[13].

30
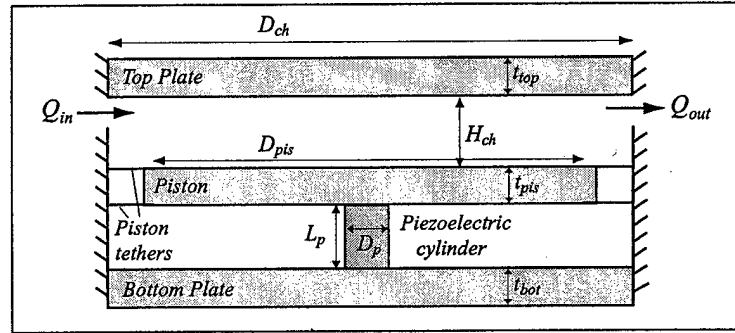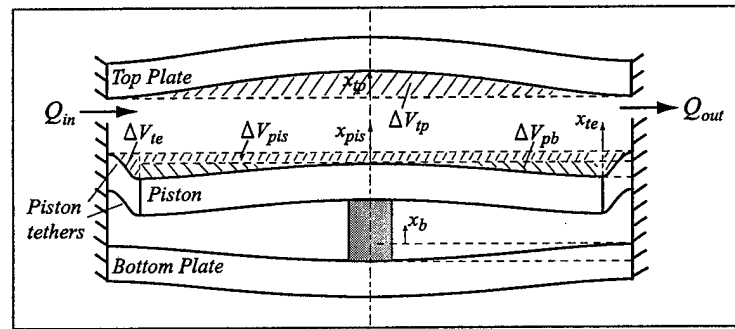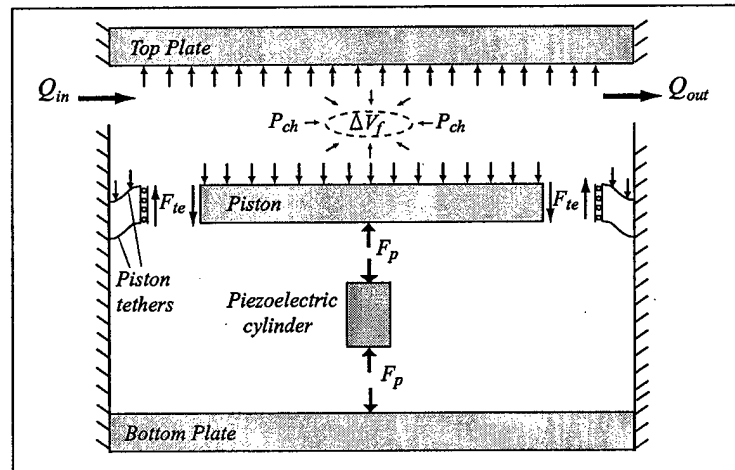
Figure 15: Energy Harvesting Chamber Model.

The valve orifice may be characterized as a flow contraction followed by a flow expansion. In the MHT
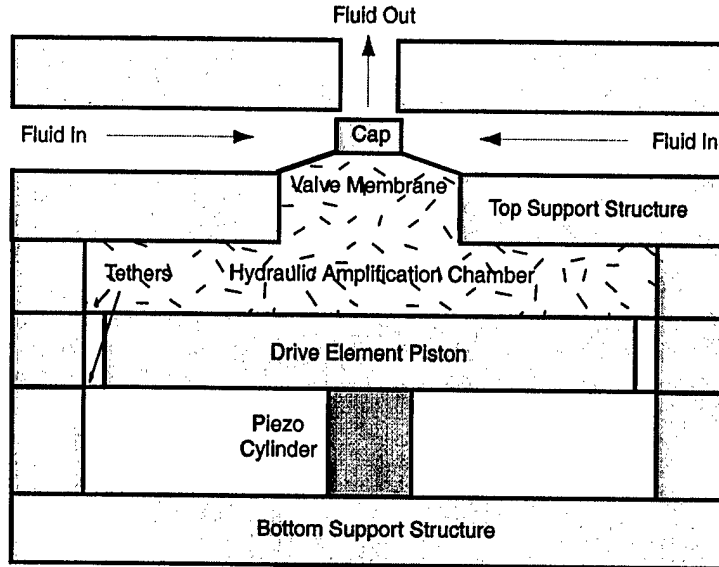
Figure 16: Schematics of the active valve.
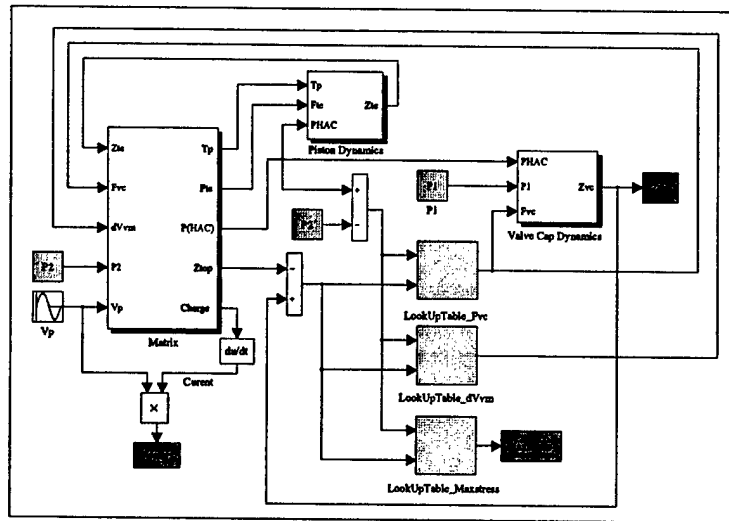
Figure 17: Simulation architecture of the active valve.

power generator, Reynolds numbers are expected to fluctuate between approximately 10 and 20,000 as the valves open and close. For this reason, correction factors obtained from experimental results need to be employed to obtain estimates of the loss coefficients for these low turbulence and laminar flow regimes [35]. A loss coefficient for each of the contraction and expansion geometries, $\zeta_{contraction}$ and
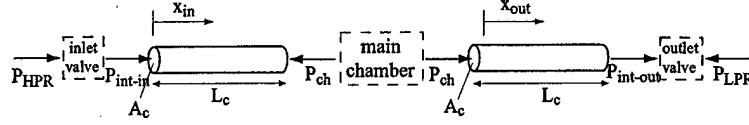
Figure 18: Device schematics showing pressures at different locations.

$\zeta_{expansion}$, respectively, is used to approximate the total loss coefficient through the valve as detailed in the following relation:

$$\zeta_{orifice} = \zeta_{contraction}(f(Re), \frac{A_o}{A_2}) + \zeta_{expansion}(f(Re), \frac{A_o}{A_1}) \tag{3}$$

where the Reynolds number is defined as:

$$f(Re) = \frac{1}{\pi} \frac{Q}{R_{vc}\nu} \tag{4}$$

The pressure-flow relation for the full valve orifice geometry can be written as:

$$\Delta P = \frac{1}{2}\rho \zeta_{orifice} \left(\frac{Q^2}{A_o^2} \right) \tag{5}$$

These flow models are based on steady flow phenomena and do not capture frequency dependent losses. For a specific value of valve cap opening at a given time during the cycle, a relationship therefore exists for the instantaneous fluid flow through the valve as a function of the pressure drop across the valve.

Flow in the Channels Due to the high Reynolds numbers, the flow in the channels is expected to be inertia dominated. Furthermore, the compliance in the fluid channels is usually negligible due to the fact that the channels are surrounded by rigid walls and their volume is much smaller than that of the chamber. Under these assumptions the flow inside the channels is modeled as one dimensional inviscid and incompressible flow. The pressure-flowrate relationship in this case is given as:

$$\Delta P = I \frac{dQ}{dt} = \left(\frac{\rho L_c}{A_c} \right) \frac{dQ}{dt} \tag{6}$$

where I is defined as the fluid inductance inside the channel, ρ is the fluid density and L_c and A_c are the length and cross-sectional area of the fluid channel respectively. For a long channel with small cross-sectional area, one can expect fluid inertial effects to play a significant role as the pressure difference builds up to accelerate the fluid slug into the chamber. Conversely, for short channels with large cross-sectional areas, the inertial effects are negligible and the pressure P_{int-in} and P_{ch} or P_{ch} and $P_{int-out}$ will not differ much. It is important to consider inertial effects when designing hydraulic systems containing small channels.

The governing equations for the fluid flow in the system, which are integrated into the system level simulation, can be obtained as:

$$P_{HPR} - P_{ch}(t) = R_{in}(Q_{in}, vo_{in})Q_{in}^2 + \left(\frac{\rho L_c}{A_c} \right) \frac{dQ_{in}}{dt} \tag{7}$$

$$P_{ch}(t) - P_{LPR} = R_{out}(Q_{out}, vo_{out})Q_{out}^2 + \left(\frac{\rho L_c}{A_c} \right) \frac{dQ_{out}}{dt} \tag{8}$$

where R_{in} and R_{out} are the fluid resistances of the inlet and outlet valves respectively.

2.2.6   Simulation and Analysis

The work cycle of the piezoelectric element is identical to the work cycle obtained from the analysis of the piezoelectric element which deforms under an applied force. The net deflection of the piston can be derived using the work cycle as follows:

$$\Delta x_p = \frac{1}{2}\sigma_d L_p(s_{33}^E + s_{33}^D) \tag{9}$$

Integrating the flowrate and using the continuity equation, the required average flowrate for a given power requirement and maximum chamber pressure can be derived as follows:

$$Q = \frac{2(s_{33}^E + s_{33}^D)W}{(s_{33}^E - s_{33}^D)P_{HPR}} + C_{eff}P_{HPR}f \tag{10}$$

where C_{eff} represents the effective chamber compliance. The first term in equation 10 corresponds to the flowrate which is required just to move the piston. The second term corresponds to the additional flowrate required due to the chamber compliance.

In order to evaluate the performance of the energy harvesting chamber, we can define the efficiency of the chamber as follows:

$$\eta_{ch} = \frac{ElectricalPowerOut}{HydraulicPowerIn} = \frac{W}{QP_{HPR}} \tag{11}$$

In the extreme case, where the effective chamber compliance is zero, the efficiency has its maximum value, which can be obtained from equations 10 and 11 as:

$$\eta_{ch\,max} = \frac{(s_{33}^E - s_{33}^D)}{2(s_{33}^E + s_{33}^D)} = \frac{k_{33}^2}{4 - 2k_{33}^2} \tag{12}$$

It is interesting to note that the maximum efficiency of the chamber depends only on the coupling coefficient of the piezoelectric material. This suggests that, regardless of the geometry and operation conditions, the above expression puts an upper bound on the system efficiency, which is only a function of the piezoelectric element chosen. It is important to note that the above definition of the efficiency corresponds only to the energy harvesting chamber. If the overall system is considered, the electrical power consumption in the active valves should be taken into consideration. It is also interesting to note that even if $k_{33} = 1$ and the effective chamber compliance is zero, which are not possible, the system efficiency cannot exceed 50%.

The system efficiency, defined in equation 11, is plotted as a function of the effective chamber compliance in Figure 19 for different piezoelectric materials. It can be noted that, as the effective chamber compliance gets smaller and smaller, in other words, as the chamber gets less and less compliant, the efficiency values approach their maximum values which were given in equations 12. As mentioned earlier, these maximum efficiency value depends only on the piezoelectric material used. PZN-PT is the most efficient material due to its high coupling coefficient($k_{33} = 0.89$) and PZT-8 is the least efficient material due to its low coupling coefficient ($k_{33} = 0.64$). We can conclude that the performance of the energy harvesting chamber heavily depends on the piezoelectric material used (k_{33}) and the chamber compliance (C_{eff}).

34

(a) Rectifier
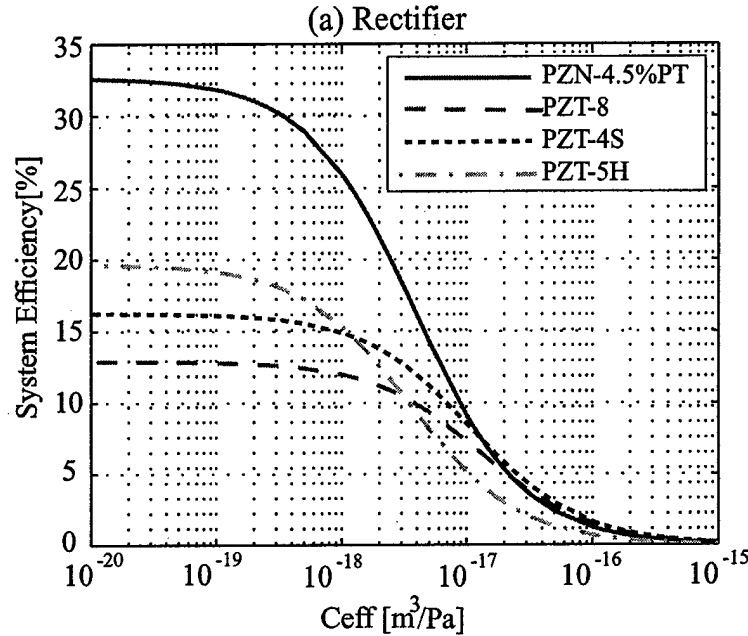
Figure 19: Comparison of different piezoelectric element in terms of efficiency.

2.2.7 Design Issues

Fluidic Oscillations Inertial effects should be considered when designing hydraulic systems containing small channels. In the MHT devices the fluid channels and the main chamber constitute a resonant system similar to a Helmholtz resonator which comprises a fluid channel and a chamber with an effective compliance. The fluidic channels have to be designed such that the device will operate at resonance condition when operated at the design frequency. As mentioned earlier, the generated power heavily depends on the pressure band in the chamber. The motivation for operating at resonance is that the same pressure band can be achieved with smaller valve cap sizes or valve openings compared to the case of negligible or very large fluid inductance in the channels, resulting in reduced power consumption in the active valves.

Chamber filling and evacuation In order to attain the desired pressure bands inside the chamber, it is important to design the valve sizes, openings and the operating frequency accordingly. The combination of the valve size and the valve opening define the overall valve resistance. For a given operating frequency and pressure band, it is important to design the valve size and opening such that they will provide just enough filling and evacuation of the chamber in the required time interval, so that the chamber pressure fluctuates between the reservoir pressures in the most economical way.

Tether Structure Optimization Accurate design of the piston tether structure is very crucial for system operation. The tethers should be flexible enough to allow sufficient motion of the piston, yet stiff enough to avoid introduction of excessive compliance into the system. The tethers have to be designed to allow maximum piezoelectric element compression for a given net fluid volume into the chamber, which occurs
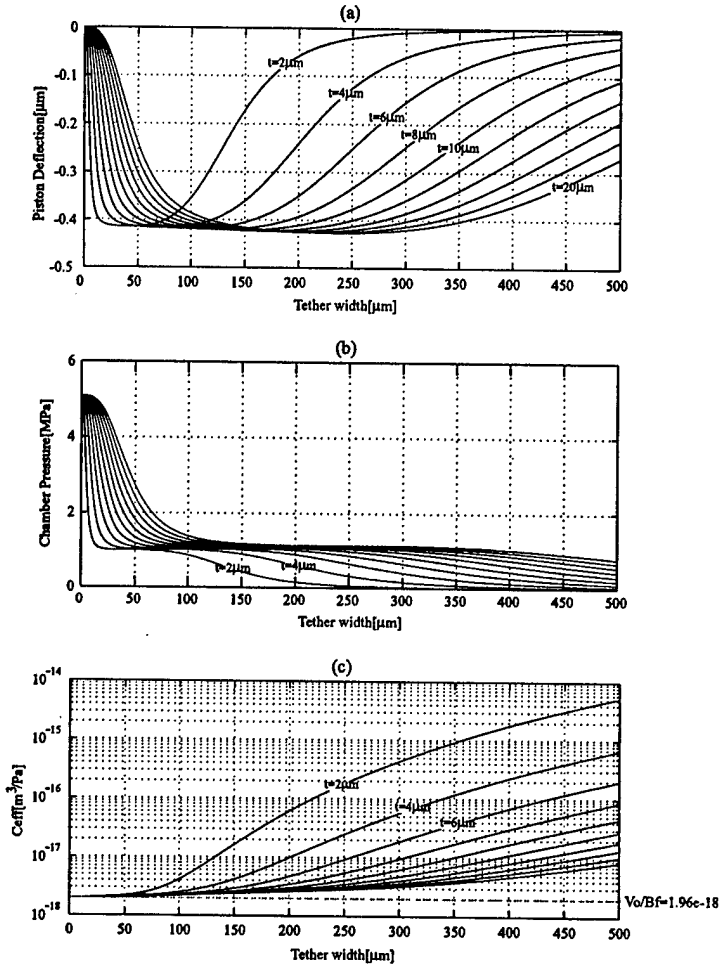
Figure 20: Piston deflection for different tether thicknesses and widths

at every cycle during system operation. If the tether is either too thin or the tether width is very large, this results in low pressure in the chamber and small compression of the piezoelectric element since the compliance introduced by the tether is very large. In other words, pressure doesn't built up inside the chamber because of the excessive bending of the tether. If the tether is either too thick or the tether width is very small, the pressure in the chamber is high but the compression of the piezoelectric element is still very small since the very stiff tethers do not allow the piston to move although they introduce very small additional compliance into the system. This suggests that for a design where the chamber diameter(or piston diameter) is determined, the tether structure has to be optimized in conjunction with fabrication limitations, such as thickness of the tether, which is determined by the SOI wafer.

Consider a chamber of the following geometric parameters: $D_{ch} = 5mm$, $D_p = 1mm$, $L_p = 1mm$, and $H_{ch} = 200\mu m$. An additional fluid volume, $\Delta V_f = 10^{-11}m^3$, is introduced into the chamber. Figure 20 shows piston deflection/piezoelectric element deflection for different tether thicknesses and widths.

36

The tether width is varied by keeping the chamber diameter the same and changing the piston diameter. It can be seen that, for a given tether thickness, there exists a range of optimum tether widths.

The stresses calculated using linear theory give a reasonable estimate and provide a first order prediction about stresses seen in the piston membranes. However, for the final, refined design, consideration was also given to the membrane fillet feature. The work described in Section 3.4 highlighted the importance of having a sufficient, but not too large, fillet feature to reduce stress concentrations in these tethered membrane structures.

Operating Conditions and Trade-offs   For a given desired power output, the following factors were considered as design guidelines:

- The operating frequency should be kept as small as possible due to the bandwidth limitations imposed by the active valve structure.

- The flowrate should be kept as small as possible to minimize valve size and reduce power consumption in the valves.

- The maximum pressure in the chamber should be kept as small as possible in order to avoid high stresses in the tethers and active valve membranes.

This section describes the choice of chamber geometry and operating conditions for a given power requirement and will discuss trade-offs between different operating conditions.

Required operating frequency for a given power requirement   The required frequency in order to generate a certain amount of power, W, is given by:

$$f = \frac{4W}{(s_{33}^E - s_{33}^D)\sigma_d^2 A_p L_p} \tag{13}$$

where s_{33}^E and s_{33}^D are the closed circuit and open circuit compliances of the piezoelectric element respectively. Figure 21 shows the plot of the required frequency for a $0.5W$ power requirement at different chamber diameters and reservoir pressures for PZN-PT as piezoelectric element. It should be noted that the required frequency does not depend on the chamber compliance, as can be seen from equation 13.

It is important to note that there is a trade-off between the maximum chamber pressure(P_{HPR}) and the operating frequency. For lower chamber pressures, higher operating frequencies are needed. In fact, for a given piston diameter the required frequency is inversely proportional to the reservoir pressure. It can be also seen that, for larger chamber diameters, the required operating frequency is smaller since for larger chamber diameters, piezoelectric elements having larger diameter will be used, which results in lower frequency requirement due to the increased piezoelectric element volume.

Required flowrate for a given power requirement   Figure 22 shows the required flowrate at different reservoir pressures and chamber diameters. It can be noted that, for larger chamber diameters, higher flowrates are required. For larger chamber diameters, lower frequencies are needed, as shown in Figure 21, which suggest lower flowrates. However, larger chamber diameters result in increased chamber compliance, which is the dominating factor resulting in higher flowrates. In this case, a trade-off exists between the required flowrate and maximum chamber pressure, namely for lower chamber pressures, higher flowrates are required.
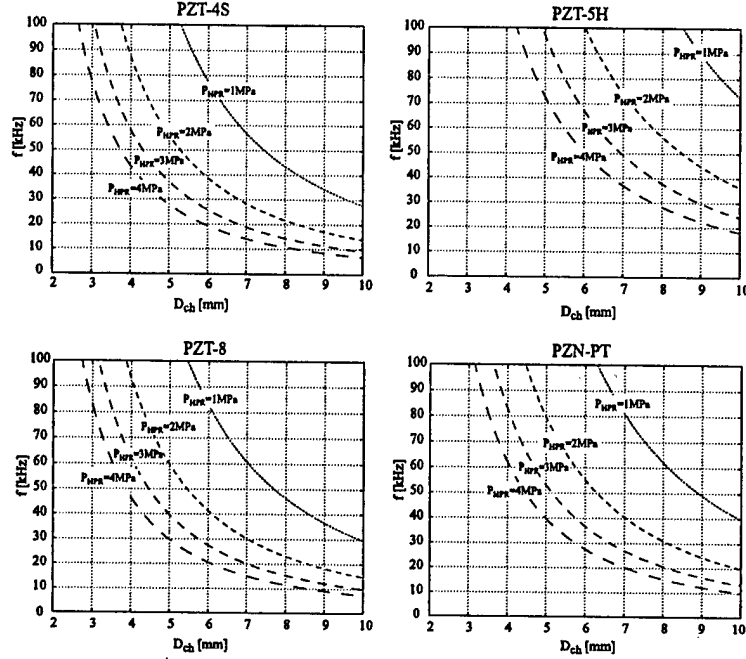
Figure 21: Effect of chamber diameter and maximum pressure on required frequency.

Efficiency The chamber conversion efficiency of the device is given by:

$$\eta = \frac{W}{QP_{HPR}} \tag{14}$$

where the power consumption in the active valves is not considered. Figure 23 shows the efficiency for different reservoir pressures and chamber diameters. For larger chamber diameters, the efficiency is lower due to the fact that the flowrate is higher at larger chamber diameters, as shown in Figure 22. It is also important to note that the efficiency decreases as the reservoir pressure increases. It is also possible to observe that efficiency does not depend on the generated power.

Preliminary design decisions The working fluid is chosen to be silicone oil due to its low viscosity and low density. It also has a comparable bulk modulus to that of water. PZN-PT is chosen as the piezoelectric element due to its high coupling coefficient, which results in efficient electromechanical energy conversion. The chamber height is chosen to be $200\mu m$. A preliminary study has shown that chamber heights smaller than this could cause squeeze film damping effect inside the chamber. On the other hand, larger chamber heights would increase the chamber compliance, which would decrease the efficiency of the system. The length of the piezoelectric element is chosen to be $1mm$. This parameter is determined by considering the actuation in the active valves, since all the piezoelectric cylinders within the system, namely the ones in the active valves and the one in the energy harvesting chamber, have the same length because of the layered structure of the device.

Parameters imposed by active valve design The basic limitation of the active valves is their bandwidth and the maximum pressure they can work against. Typical trade-offs in the active valve design are stroke,

38
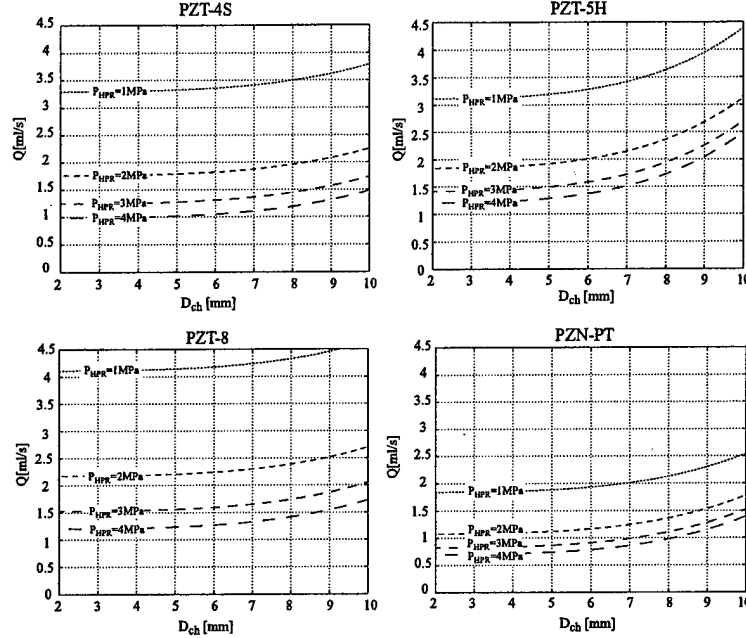
Figure 22: Effect of chamber diameter and maximum pressure on the required flowrate.

bandwidth and force. Also, the active valves impose a minimum pressure requirement, the bias pressure, due to cavitation considerations in the hydraulic amplification chamber(HAC) within the active valve structure.

Parameters imposed by fabrication processes The device consists of silicon and Pyrex micromachined layers. The thickness of the layers dictate the thicknesses of individual components. For example, a double layer piston structure, which consist of two silicon layers bonded to each other, will have a thickness of $t_{pis} = 800\mu m$. Since the tethers are created through deep reactive ion etching(DRIE) of a SOI wafer, the tether thickness is defined by the SOI layer. Also, the fillet radius control during the fabrication process imposes some limitations on the tether width. For example narrow tethers would be very stiff due to the relatively large fillet radius and the predictions of the linear theory used for the optimization would not valid beyond a certain tether width. The tether thickness was chosen to be $10\mu m$. The thicknesses of the top and bottom support structures are determined by the number of layers used, including the packaging layers on top and bottom portions of the device. The compliance of the system is very important in terms of system performance and they should be kept as small as possible. Therefore it is desirable to have very thick top and bottom support structures. The effective thickness would also depend on the structure of the auxiliary system in which the device is packaged.

2.2.8 Design Refinement Procedure

Figure 24 presents a design refinement procedure, which was followed after the initial design decisions were made using the considerations mentioned in the previous sections. The first part consists of analytical design calculations. The pressure band in the chamber is dictated by the bias pressure, P_b, and
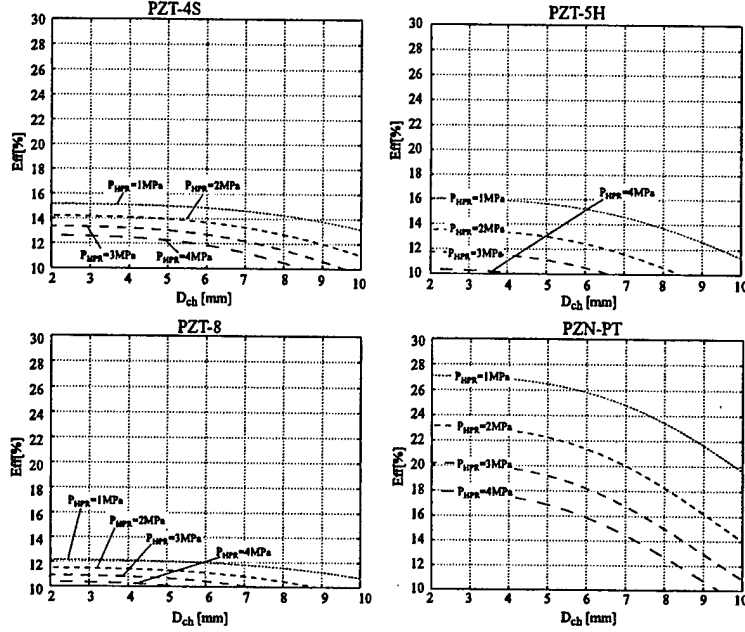
Figure 23: Effect of chamber diameter and maximum pressure on efficiency.

high pressure reservoir pressure, P_{HPR}. The piston diameter, piezoelectric element diameter and battery voltage are calculated using analytical expressions derived. These calculations are followed by the tether structure optimization, which determines the optimum tether width, w_t, for the given tether thicknesses and piston diameter. The designed tether width also determines the chamber diameter, D_{ch}. The geometric parameters along with the operation conditions are then fed to the system level simulation. The simulation architecture is shown 25.

First, simulations are performed to determine the optimum length to area ratio of the fluid channels, using arbitrary valve resistance, i.e. arbitrary valve cap size or valve openings. It is helpful to run these simulations with very small valve resistance, namely with very large valve opening or very large valve cap, since the fluidic oscillations are much more pronounced with lower valve resistances and it is easier to determine the optimum length to area ratio of the channels. Then, the valve cap size and valve opening are designed such that the chamber pressure fluctuates between reservoir pressures, namely between P_{HPR} and P_{LPR}. At this stage, it is important to consider structural limitations, which might be imposed by the active valves. For example, a large valve cap size requires a large membrane to allow sufficient valve motion, however this may cause excessive stresses in the membrane. Or, a very large valve opening can cause the same problem. Since the same effective valve resistance can be achieved with different combinations of valve opening and valve cap size, coupled iterations may be necessary with the active valve design procedure, which is shown in Figure 26. Finally, the system is simulated, stresses in the tethers and on the piezoelectric element are checked, and design iterations are performed if necessary to compensate for dynamic effects. The design procedure presented above is followed by the layout and mask design for the fabrication.

Calculate $\left(\frac{D_{pis}}{D_p}\right)$ ratio ◄——— depolarization stress, σ_d, and max. pressure, P_{HPR}

Calculate the stress band, $\Delta\sigma$ on the piezo ◄——— bias pressure, P_b and P_{HPR}

analytical calculations (quasistatic)

Calculate D_{pis} and D_p ◄——— power Requirement, W, frequency, f, and length of piezo L_p

Calculate optimum battery voltage ◄——— length of piezo L_p

structural optimization (quasistatic)

Design tether width and thickness ◄——— maximum allowable tether stress (silicon membrane strength test)

microfabrication feasibility

(dynamic effects)

simulation (dynamic)

Determine optimum $\left(\frac{L_c}{A_c}\right)$ ratio for maximum pressure fluctuation

Determine valve cap size, R_{vc}, and valve openings, vo_{in} and vo_{out}, such that chamber pressure fluctuates between P_{HPR} and P_{LPR} ◄——— active valve design

Check the design for maximum allowable tether stress and piezoelectric element stress(dynamic effects might be important)

layout/ mask design

Design fluid channels ◄——— microfabrication feasibility

Figure 24: Refinement procedure.

2.2.9 Design Parameters

This section presents the design parameters of the MHT Energy Harvester. The preliminary design decisions, parameters imposed by fabrication process and material limitations are summarized in Table 1. The final design parameters are listed in Table 2.

2.3 Contributions: Modeling

The contributions of the modeling of the MHT device can be summarized as follows:

1. A detailed systems level model of the MHT device that includes all the major parameters has been developed.

2. As a subset of this effort, a model has been developed for a annular plate with a rigid center boss undergoing large deflections. This enabled the taking into account of the large deflections of the valve membrane structures. This model was also used extensively in the active valve design effort.

3. A tether width optimization scheme was introduced to determine the optimal width for the piston and valve tethers.

41

Design Decisions		
Piezoelectric material	PZN-PT	lowest flowrate requirement
Working fluid	silicone oil	low viscosity and density
Piezoelectric element length, L_p	$1mm$	active valve actuation
Chamber height, H_{ch}	$200\mu m$	squeeze film damping
Parameters imposed by fabrication process		
Piston thickness, t_{pis}	$800\mu m$	double layer piston
Top and bottom support structure thickness	$2.5mm$	packaging layers
Tether thickness	$10\mu m$	fabrication feasibility
Material Limitations		
Depolarization stress of piezoelectric element, σ_d	$10MPa$	shouldn't be exceeded
Maximum allowable stress in tethers	$1GPa$	shouldn't be exceeded

Table 1: Summary of preliminary design decisions.

Power Requirement	$0.5W$	Electrical power output
Parameters imposed by active valve design		
Operation frequency, f	$15kHz$	bandwidth of active valves
Bias Pressure, P_b	$0.4MPa$	cavitation in HAC chamber
High Pressure Reservoir Pressure, P_{HPR}	$2.4MPa$	membrane stress limitation
Important parameters resulting from operation conditions		
Pressure band in the chamber, ΔP_{ch}	$2MPa$	-
Stress band on piezoelectric element, $\Delta\sigma$	$8.33MPa$	-
Designed parameters		
Piston Diameter, D_{pis}	$6.85mm$	-
Piezoelectric cylinder diameter, D_p	$2.05mm$	-
Battery voltage, V_b	$90V$	-
Tether width, w_t	$225\mu m$	optimization
Chamber diameter, D_{ch}	$7.3mm$	-
Fluid channel length to area ratio, $\frac{L_c}{A_c}$	$2000m^{-1}$	same for inlet and outlet
Valve cap radius, R_{vc}	$300\mu m$	same for inlet and outlet
Valve opening, vo_{in}, vo_{out}	$30\mu m$	same for inlet and outlet
Performance parameters		
Net flowrate, Q_{net}	$1ml/s$	-
Hydraulic power input	$1.3W$	$(P_{HPR} - P_{LPR})Q_{net}$
Efficiency, η	19.2%	$\frac{Electrical power output}{Hydraulic power input}$

Table 2: Summary of design and performance parameters.

4. A number of design features were introduced to improve either the manufacturability or the performance of the MHR device, or both.

5. As a final result, a detailed design for a bench top MHT device was produced. The eventual experimental results, discussed in Section 7, correlated well with this design.

(a)

(b)

(c)
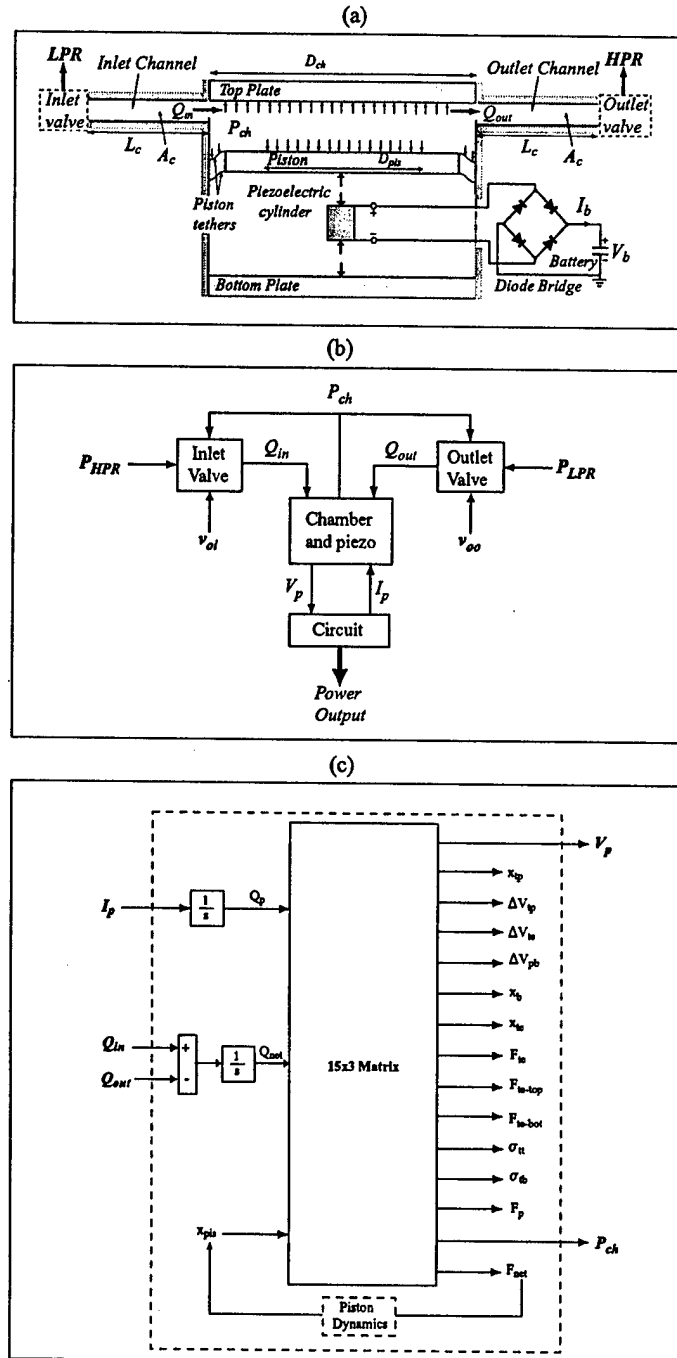
Figure 25: System level simulation architecture.
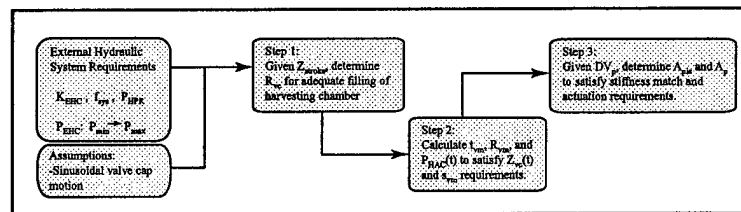
Figure 26: Design procedure of the active valve.

3 Supporting Experimental Investigations

3.1 Investigation of Flow Losses Through Microscale Orifices

The rapid increase in the development of complex microfluidic devices has revealed a need for more accurate modeling of fluid behavior in small-scale microfabricated geometries. Microvalves tend to be one of the dominating elements in such systems, but at the same time their detailed behavior remains poorly understood and systematic studies of microvalve fluid mechanics are lacking.

In the case of the Micro Hydraulic Transducer program at MIT, the requirements on valve modeling take a different perspective. In this case the valve and head loss models are used as design tools. Typical orifice models will not capture geometry related sensitivities necessary for design and optimization. Furthermore, one of the goals of the MHT project is to harvest energy with this device, for this reason, and considering that the valve is the dominating head loss, it becomes critical to determine accurately the corresponding head losses and sensitivities. Only then will it be possible to design a more efficient valve.

The major fluid mechanics challenge is to model the steady and unsteady fluid behavior in these micron-scale geometries. The Reynolds number during one cycle varies between 1 and 20,000 with a Strouhal number of order 1. In this regime both inertial and viscous forces are important and unsteady effects cannot be ignored. The model needs to be accurate, yet implemented in a flexible manner suitable for design purposes and integration into full system simulations. Unfortunately, such models do not presently exist, and where partial models are available, they are typically neither calibrated nor validated for the small scales and unique geometries that are found in microfluidic systems. The purpose of this work is to provide such calibration and validation.

3.1.1 Microsystems Fluidic Modeling Strategies

Previous experiences by Olsson, Bourouina and Gravesen have proven that the lumped element model is useful for the analysis of microfluidic systems. The lumped model has the added advantage that due to its similarity with circuit system-analysis existing software, such as SPICE and SIMULINK, can be used to obtain solutions. In this case the behavior of localized components needs to be characterized separately. In our case the microvalve dominates the flow regime and therefore is the focus of this work.

3.1.2 Results

Numerical and analytical techniques are inadequate for characterizing valve flows in the low turbulence to transition regime therefore a experimental approach was favored. The experiments were carried out on a scaled up version of the valve for ease of instrumentation.

3.1.3 Transition Reynolds number

Observing the experimental results for different valve sizes a unified formula for predicting the transition Reynolds number was formulated. The transition Reynolds number is described as a function of the valve opening ratio (h^*) and the valve diameter (d^*) ratio. Having an expression that predicts the transition Reynolds number for different valves and openings we can define a modified Reynolds number (Re_m) such that all curves will experience transition at the same point. The curve is empirical in nature and no attempt is made to relate it to physical variables. The modified Reynolds number (Re_m) is defined as
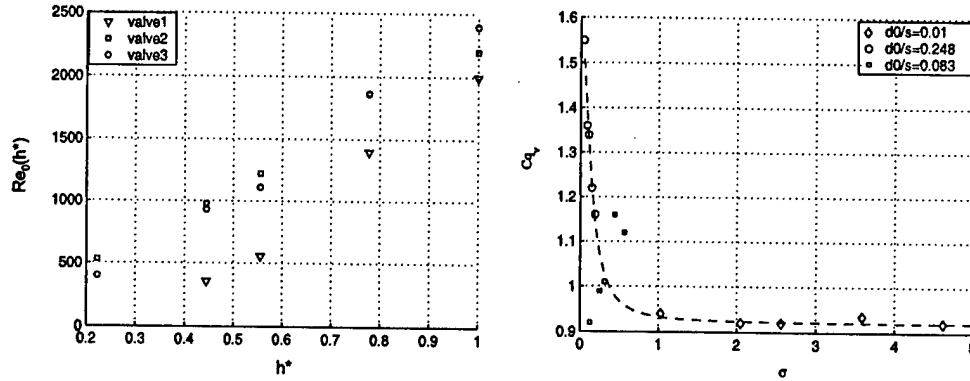
Figure 27: Transition Reynolds number vs valve opening ratio and ,Discharge coefficient (C_q) vs. non-dimensional valve opening (h^*) for the three valves; plate separation (h_p) 450 μm. h^*

$$Re_m = Re_0 - h^* \left(\frac{1 - 0.692d^*}{2.483e^{-3} - 2.818e^{-3}d^*} \right) + \left(\frac{2942 - 2205d^*}{1 - 1.88d^*} \right) \tag{15}$$

where $Re_0 = 4Q/(\pi d_0 \nu)$ is the Reynolds number based on the valve inlet diameter (d_0), h^* is the valve opening ratio and d^* is the valve diameter ratio. The results of the scaling can be seen in Figure 27.

3.1.4 Valve Seat Width Dependence

The effect of the valve seat width was investigated with three valves of different seat widths (s). The results are shown in Figure 27 where the x-axis shows the ratio of valve opening (h_v) to seat width (s), defined as (σ). The y-axis uses the modified discharge coefficient $C_m = C_q/(4h^*)$ where $C_q = 4Q/(\pi d_0 h_p)\sqrt{\rho/(2\Delta P)}$. One interesting result is that for values of $\sigma > 1$ the modified discharge coefficient is not affected by the seat width, s. Once this threshold is passed, however, the discharge coefficient becomes very sensitive to the seat width and rises rapidly. Significant pressure recovery is observed, even surpassing C_m=1. This increase in discharge coefficient may be explained by drawing an analogy to thick orifices. For a thick orifice, the separation bubble tends to reattach within the throat area as shown by Sahin et al. The reattachment reduces the flow losses across the orifice. For the case where the non-dimensional seat width $\sigma < 1$ the same phenomenon is observed and we theorize that the separated flow undergoes reattachment with the accompanying pressure recovery.

A curve fit for the discharge coefficient (C_m) as a function of σ, the valve opening over seat width ratio, is given by

$$C_m = \left\{ 0.9203 + \frac{0.6755}{1 + \left(\frac{\sigma}{0.1327} \right)^{1.9361}} \right\} (h^*)^{-b}. \tag{16}$$

$$b = \frac{\frac{0.1}{1 + \exp\left(\frac{Re_m - 2050}{200} \right)}}{1 + 10^{\left(\frac{\ln(s/0.25)}{0.5} \right)}} \tag{17}$$

which is a function of the valve seat width (s) and the modified Reynolds number.

The curve shown in Figure 28 can be approximated by using equation 18 as suggested by Lichtarowicz. The curve however requires different coefficients which were obtained using the curve fitting program DATAFIT. The equation is then given by :

48
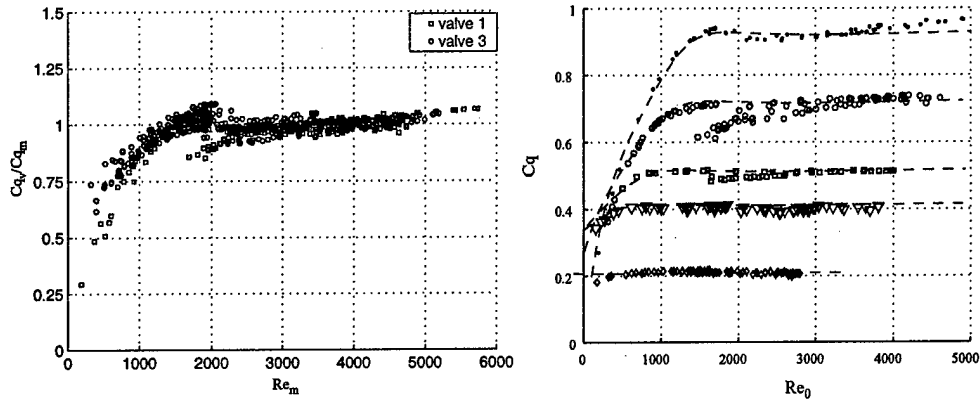
Figure 28: Scaled data for valve #1 and valve #3, Curve fitting using 18 for valve #1

$$\frac{1}{C_n} = \frac{Cm}{Cq} = 0.956 + \frac{364.89}{Re_m} - \frac{0.194}{1 + 2.608(\ln(0.000718 Re_m))^2}. \tag{18}$$

where C_m (Equation 16) gives the magnitude of C_q at the turbulent regime limit and C_n (Equation 18) gives the necessary correction factors to account for the Reynolds number dependence in the transition and laminar flow regimes. The quality of the curve fit can be appreciated when compared to the original data. The results for valve #1 can be seen in Figure 28 showing that the curve fit describes accurately the valve behavior for different valve openings and Reynolds numbers.

3.1.5 Contributions

An hydraulic model for the Micro-Hydraulic Transducer was constructed based on a low-order lumped element model. The valve flow characteristics were investigated experimentally and parametric studies were carried out to obtain the flow dependencies and allow for a better estimation of the head losses. Data reduction and curve fitting resulted in a model comprised of three formulas which can be used to predict the discharge coefficient C_q of a poppet valve based on the Reynolds number and valve dimensions. The results presented can in turn be used as part a systems simulation for design and optimization purposes.

3.2 Determination of Fluid Filling and Sealing Procedures at the Microscale

3.2.1 Objectives

For effective hydraulic amplification, the compliance of the hydraulic amplification chambers had to be minimized. Hence, reliable filling and sealing techniques were required to ensure the stiffest hydraulic amplification chamber possible. This section describes filling techniques developed in conjunction with Boston MicroSystems. It also addresses the sealing techniques that were developed to properly seal the hydraulic amplification chambers for either static or dynamic sealing purposes.

3.2.2 Filling techniques

Fluid requirements For the full MHT device, the working fluid had to satisfy the following requirements:

- Low viscosity, for minimal viscous losses.

- High bulk modulus, for minimal compliance.

- Should wet silicon surfaces well, to ease filling of small cavities.

- Should be dielectric, due to the high voltage operation of the device.

Based on these requirements a volatile silicone oil, Hexamethyldisiloxane (Produced by Dow Corning under the trade name DC200 0.65cst), was chosen as the system fluid. This was also the fluid used in all devices tested in this document.
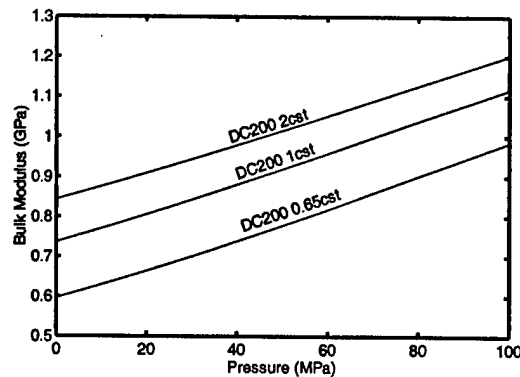
Figure 29: Bulk modulus vs. fluid pressure for a selection of volatile silicone oils, adapted from data as supplied by Dow Corning. Note that the amount of outgassing performed on these fluids is unknown.

The properties of various silicone oils indicate that there is a tradeoff between viscosity and bulk modulus. This is also shown in Figure 29. In the case where it is possible to use a different fluid in the HAC, it might pay off to investigate slightly more viscous fluids with higher bulk moduli. Note, however, that filling of the HAC, as described in the previous section, relies on the working fluid also possessing a high vapor pressure. This requirement eliminates most of the high viscosity oils. (See Figure 30)
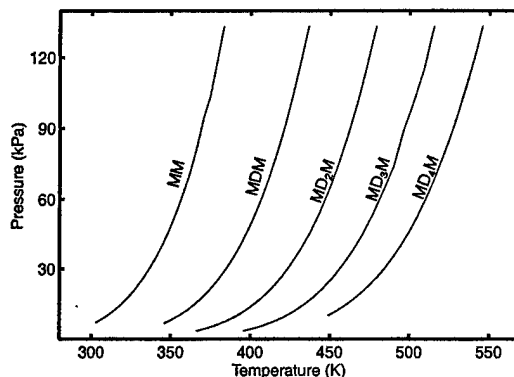
Figure 30: Vapor lines for a selection of linear siloxanes. The graphs show the vapor lines for Hexamethyldisiloxane (MM), Octamethyltrisiloxane (MDM), Decamethyltetrasiloxane (MD_2M), Dodecamethylpentasiloxane (MD_3M) and Tetradecamethylhexasiloxane (MD_4M). Dow Corning DC200 0.65cst consists of MM and trace impurities. The other viscosities may contain blends of the compounds mentioned above.

Filling process To ensure bubble-free filling of the HAC, a filling system and associated filling process was developed. Figure 31 shows a schematic of the apparatus and Figure 32 is a photograph of the same apparatus.

To fill and seal an HAC, the following process was developed:

1. Set the initial condition of the system: All valves closed.

2. Open Tank B, and place the device test jig (Discussed in Section 6.1.3), as well as the device, inside. Do not mount the device in the jig yet. This will be done after filling. Also do not install any o-rings in the jig. They are installed after filling. Close Tank B.

3. Start vacuum pump VP1.

4. When sufficient vacuum has been attained in the cold traps, CT1 and CT2, fill CT1 and CT2 with liquid nitrogen. Open ball valves V5 and V1.

5. *Substep if Tank A is not already filled with silicone oil:* Connect silicone oil reservoir (not shown) to Tank A via V6. FT1 will filter the inlet stream. Open V6 and V2. This will draw the silicone oil into Tank A, and simultaneously outgas the oil. Dissolved gases tend to reduce the effective bulk modulus of the oil, an undesired effect. After Tank A is filled, Close V6 and V2. Disconnect silicone oil reservoir and vent Tank A to atmosphere through V6.

6. Open V3. Evacuate Tank B to $5mmHg$ or less.

7. *Vapor purging step:* Slowly open V4 and allow a small amount of silicone oil to flow into Tank B. In this case, a fluid level of approximately $10mm$ was used in Tank B. Close V4.

8. Continue pumping on Tank B for approximately 90 minutes. All of the oil in Tank B should have evaporated, and would have been caught in CT1. Ensure that Tank B is at a pressure of $5mmHg$ or less.

51
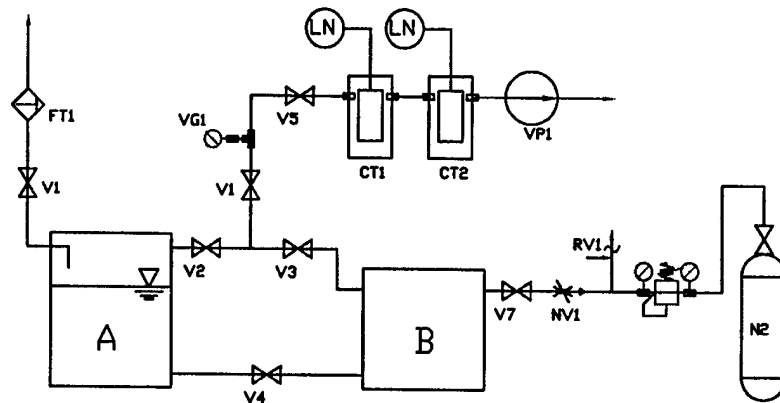
Figure 31: Schematic representation of the filling system
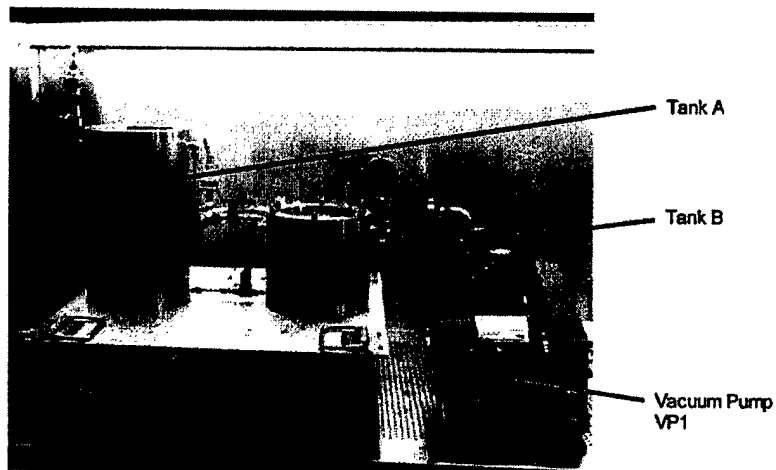
Figure 32: The fluid filling system. The cold traps are not shown in this photograph.
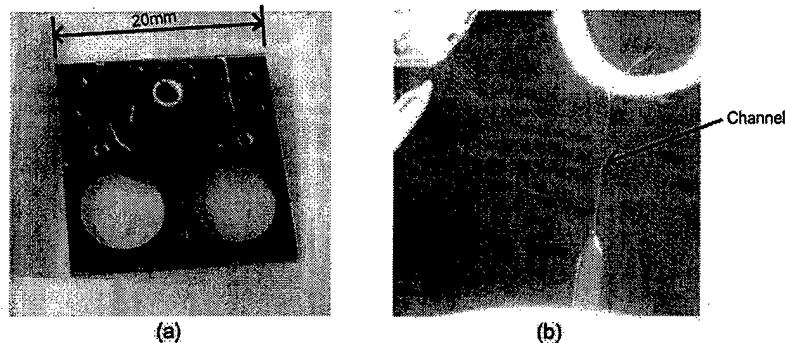
Figure 33: (a) Experimental filling test chip with two $10\mu m \times 10\mu m \times 1mm$ channels and matching dead volumes. (b) Detail of the filling channel. The dead volume had to be evacuated through this channel prior to filling.

9. *Filling:* Close V3. Slowly open V4 and allow the fluid to submerge the jig and the device. Close V4 when the contents of Tank B are submerged.

10. *Pressurising:* Open V7 and needle valve NV1. Adjust the regulator, APR1, to provide an absolute pressure of $1.5atm$. This will ensure that the pressure in the HAC asymptotes to a slightly higher pressure than atmosphere.

11. Reduce the pressure in Tank B to $1atm$ absolute pressure, and open Tank B.

12. With the device and the jig still submerged, insert the o-ring seals into the jig, mount the device and clamp to seal.

Initial tests In this work it was necessary to fill a dead volume of approximately $8.3\mu l$ through a channel of dimensions $10\mu m \times 10\mu m \times 1mm$. The motivation for this channel will be discussed in Section 3.2.3. The nature of the design of the devices prevented any visual inspection of the HAC for bubbles after filling. It was therefore essential to verify the filling procedure described in Section 3.2.2, and to ensure that it was very robust. To this end, a set of experimental devices was fabricated in such a manner that the filling procedure could be seen through a suitable glass window. A device consisting of a glass-silicon-glass sandwich structure was fabricated using DRIE and a simple two step lithography process. A completed filling test chip is shown in Figure 33. Assembly was performed on the die level, using simultaneous anodic bonding of the top and bottom glass layers. In this case, conventional machining, using diamond tools, was used to drill holes in the top glass layer.

Using the procedure as described above, and visually monitoring the filling of each chamber using a microscope, it was verified that bubble-free filling could be obtained. The filling time after initiating the pressurization step was found to be approximately 7 minutes. After this time, no visible bubbles were detected. Two of these devices were assembled, giving a total of four chambers to be filled. Both chips were filled successfully on the first attempts to fill them. These results provided the needed confidence to fill and test the full hydraulic amplification devices.

O-ring for
preloading

Brass Spreader

PTFE Film

Seal extrusion can
cause pressure rise
in the HAC

Significantly less
seal extrusion

(a)

(b)
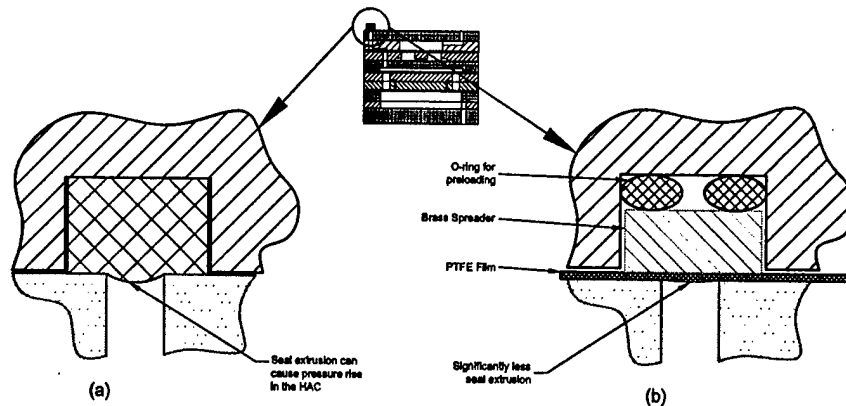
Figure 34: Static sealing of the hydraulic amplifier: a) The basic concept of a elastomeric or plastic seal. Seal compression could introduce large pressure changes in the HAC. b) Using a PTFE film for sealing, with a load spreader and a preloading element.

3.2.3 Sealing concepts

Sealing of an hydraulic amplifier can be challenging. One would like to maximize the stiffness of the hydraulic coupler. This also means that any imposed volume change, as might be introduced by a seal pressing against an opening and subsequently bulging could introduce a large pressure increase in the hydraulic amplification chamber. (See Figure 34a). This led to the development of two sealing strategies for the two different types of tests performed on the hydraulic amplifiers evaluated in this work. The first type is a traditional static seal, as described above, and the second type, for high frequency hydraulic amplifiers, is a dynamic seal relying on a flow restriction.

Static sealing For static sealing of the hydraulic amplifiers a seal consisting of a Teflon sheet, $125\mu m$ thick, backed by a brass plate and preloaded with an o-ring was used, as illustrated in Figure 34b. This method enabled reliable sealing of the hydraulic amplifiers while giving minimal seal compression and volume change in the HAC, even with a sealing hole diameter in the glass layer of $800\mu m$. Should seal compression be of greater concern, the sealing hole diameter can be further reduced by micromachining the inlet port to the HAC.

Dynamic sealing If the hydraulic amplifier is to be operated only at high frequencies, another sealing technique can be used. By providing a suitable flow restriction on the inlet port to the HAC, it can be shown that high frequency pressure fluctuations generated by the large piston inside the HAC will not be transmitted to the outside. This restriction will have the effect of a low pass filter, allowing low frequency pressure variations to enter and leave the HAC. Using this sealing technique, the concerns related to seal compression are eliminated and it becomes easier to control the static pressure in the HAC. These benefits come at the cost of an external pressurization system that must be added to the device. For experimental purposes, this was not a concern. Figure 35 illustrates the basic principle. In addition, the external pressurization system provides the benefit of setting a constant pressure bias in the HAC. This in turn allows for balancing of the steady-state pressure on the small piston, and can also be used to control the static position of the small piston, should an offset be desired as, for example, in the case of a valve [33]. Furthermore, placing a bias pressure on the HAC reduces the likelihood of

54
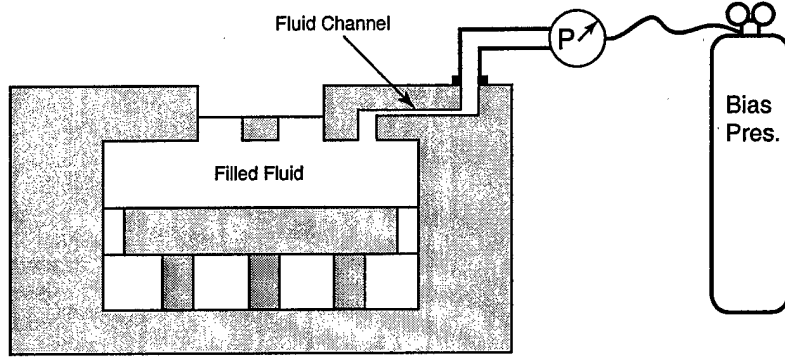
Figure 35: Schematic of the high resistance fluid channel between the HAC and an external bias pressure regulator. This channel was etched into the underside of Layer 7.
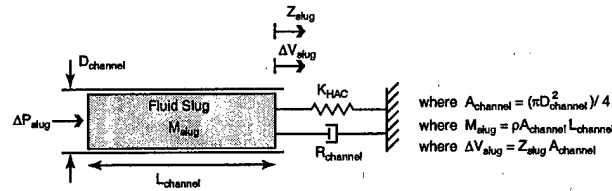
Figure 36: Model of the high resistance fluid channel between the HAC and an external bias pressure regulator. A fluid slug within the channel is modeled. This slug is acted upon by an external stiffness associated with the HAC chamber stiffness. Additionally, the flow resistance of this slug through the channel is modeled using laminar Hagen-Poiseuille flow relations.

cavitation that could be induced by high frequency operation of the large piston.

A simple way to design this type of seal is to assume it to be a channel of suitable dimensions, containing a fluid slug. (See Figure 36.) By selecting the appropriate boundary conditions for the fluid slug in the channel, and by estimating the losses in the channel using Hagen-Poiseuille flow, one can predict the cutoff frequency of such a channel. As discussed in [33], such a channel was designed using the following equation of motion, as given by Roberts, as a starting point:

$$\left(\frac{M_{slug}}{A_{channel}^2}\right) \Delta \ddot{V}_{slug} + R_{channel}\Delta \dot{V}_{slug} + K_{HAC}\Delta V_{slug} = \Delta P_{slug} \tag{19}$$

A channel of dimensions $10\mu m \times 10\mu m \times 1mm$ was designed. Letting $L_{channel} = 1mm$, $D_{channel} = 11.3\mu m$, $K_{HAC} = 1.0e^{17}Pa/m^3$, $\rho_{fluid} = 760kg/m^3$, and $\mu_{fluid} = 6.5e^{-4}kg/(ms)$ gives a frequency of $48Hz$ for which ΔV_{slug} is 1% of the large piston volume change. For a further treatment of this subject, the reader is referred to [33].

Test results, as shown in Figure 37 clearly indicate the effectiveness of this channel. A lower cutoff frequency of approximately $0.1Hz$ was observed. This frequency is even less than the design cutoff frequency. It is also significantly less than the design frequency for the hydraulic amplifier, of between 1 and $15kHz$. This ensures that the full pressure swing created by the piezoelectric actuators acting on the large piston is transferred to the smaller piston.

55
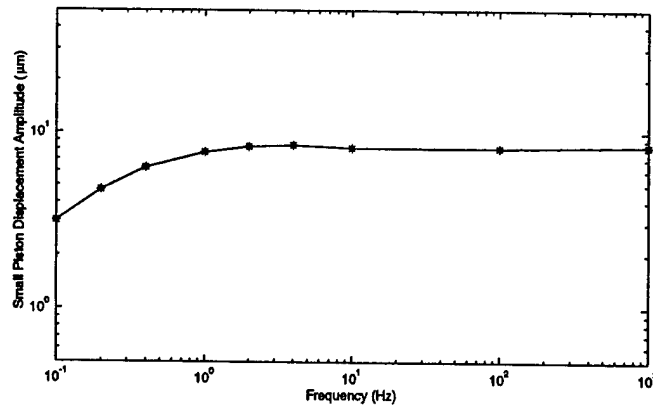
Figure 37: Experimental results of tests performed on a flow restriction-type dynamic seal. This test was performed by applying a sinusoidal excitation of $200V_{p-p}$ to the piezoelectric element of the large piston, and measuring the displacement of the small piston for the frequencies shown. Note the good quasi-static performance down to 1Hz.

3.2.4 Accomplishments

The accomplishments in terms of filling and sealing of hydraulic amplifiers can be summarized as follows:

- Successful filling of micromachined dead volumes of approximately $10\mu l$ in volume

- Successful static sealing of such volumes with minimal seal extrusion.

- Successful dynamic sealing of such volumes.

3.3 Evaluation of Piezoelectric Material Energy Harvesting Capabilities

3.3.1 Objective

As has been mentioned before, a useful feature of piezoelectric materials is that one can generate electric power by squeezing it very hard and fast. However, it is a major concern that the high compression parallel to the piezoelectric polarization direction may depolarize the materials [39]. Therefore, engineers desire to know the limit of compressive load without degenerating the materials. Another concern is the frequency dependency. A previous study [40] shows that piezoelectric generation using a resistive load has low efficiency at high frequency. However, the present study in this work shows that the frequency dependency depends on type of circuitry used in the power harvesting scheme. In this work, using a diode bridge configuration demonstrates that the energy can be harvested and stored in a battery and the efficiency is independent of the frequency below the specimen natural frequency.

This section will fully investigate the rate and stress effects. The common commercial piezoceramic PZT-5H [2] was selected for test because its moderate piezoelectric constant, stiffness, availability and low cost. Other modern engineered materials such as single crystal PZN-PT [3] and PMN-PT [4] were also evaluated because of their high piezoelectric constants and promise of high performance. PZN-PT was also the material of choice for the energy harvester.

3.3.2 Resistive Load vs. Rectifying Circuitry

In order to study the difference between a resistive load and a rectifying circuit, a linear electromechanically coupled model was built using SIMULINK by Mathworks Inc. In this model, the material constant is assumed to be independent of stress and frequency. This model can be used to simulate the response of a piezoelectric specimen subjected to a mechanical load and connected to a given circuit topology, whether be it a resistor or a diode bridge. More details of this model can be found in [38].

Before simulating the resistive circuitry, an understanding of a piezoelectric element as a capacitor with a limited current source must be obtained. Due to this limited current source and the capacitive impedance of the piezoelectric material itself, the current flowing to resistor is frequency dependent. As shown in Figure 38, in order to maximize the current flowing through the resistor, the value of the resistor (R) must match the impedance of the specimen (C):

$$|R| = \left| \frac{1}{j 2\pi f C} \right| \tag{20}$$

or

$$R = \frac{1}{2\pi f C} \tag{21}$$

where j equals $\sqrt{-1}$ and f is the driving frequency of mechanical load. Figure 39 shows the simulated force-displacement relation of specimen connected to a resistor. The area enclosed by this force-displacement relation represents the mechanical energy transformed into electrical energy. As a result, for a given amplitude of input force, the larger the enclosed area , the higher the efficiency. As shown in the Figure 39, for a 100pF specimen with a $10^9/(2\pi)$ Ω resistor, the maximum efficiency occurs at

---

[2] 6.35mm cube supplied by Staveley Sensors in E. Hartford, CT.
[3] PZN-4.5%PT, 5.5mm cube ,supplied by TRS Ceramics, Inc., State College, PA.
[4] 6mm × 6mm × 4mm supplied by Crystal Associates Inc., East Hanover, NJ.

10 Hz. This correlates to the experimental results obtained by Goldfarb. However, the same efficiency at different frequencies can be obtained by matching the impedance, for instance, by using a resistor of $10^{10}/(2\pi)$ Ω at 1 Hz or a resistor of $10^8/(2\pi)$ Ω at 100 Hz. This analysis demonstrates that the frequency dependency comes from the mismatch between the resistor and the impedance of the specimen. Unfortunately, the factor of impedance mismatch had not been not considered by Goldfarb.
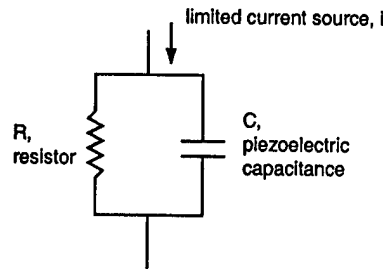
Figure 38: Effect of the limited current source on a RC circuit.
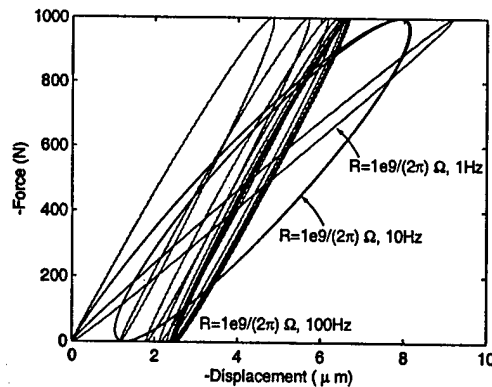
Figure 39: Simulation of force-displacement relation of piezoelectric specimen with resistive load.

In contrast to a resistive load, a rectifying circuit shown in Figure 40 will result in an efficiency which is independent of frequency, if ideal diodes are used. Figure 41 shows the comparison of the simulated force-displacement relation of a properly matched resistive load and a rectifying circuit. Although the maximum efficiency of the rectifying circuit is slightly smaller than that of the resistive circuit, the benefit of using rectifying circuitry includes frequency independence and the fact that the electric power can be stored in a battery instead of merely being dissipated.

3.3.3 Characterization of Generalized Material Constants

The simulation used in the previous discussion is based on the assumption that the material properties are independent of stress and frequency. This linearity may not be true in practice. As a result, it is of
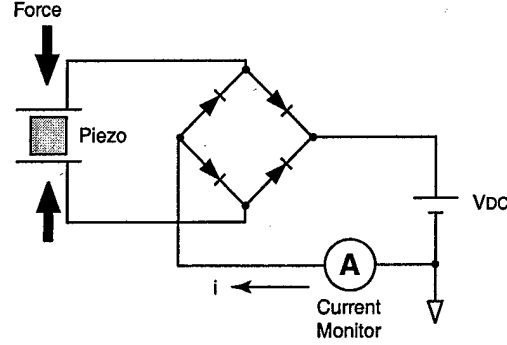
Figure 40: Diode bridge circuitry
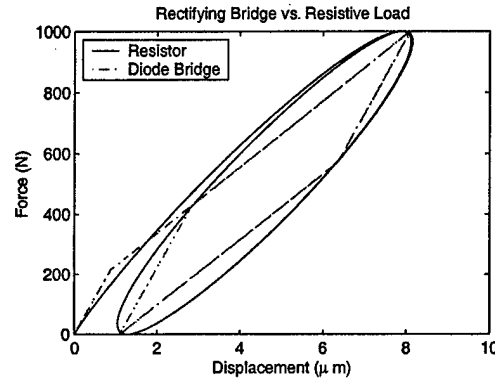
Figure 41: Simulation of force-displacement relation of piezoelectric specimen with a resistor or a rectifying diode bridge.

interest to obtain experimental data of material constants as a function of stress and frequency. To do so, a generalized material constant is first defined as the linear slope of material response with respect to the stress at different amplitudes and frequencies of the input stress. These generalized material constants include piezoelectric coupling constants d_{33} and g_{33}, and compliance s_{33}^E and s_{33}^D, which are required inputs of the simulation model. The d_{33} constant can determine how much current can be drawn from the specimen at short circuit condition. The g_{33} constant can determine how much potential can be generated on the specimen at open circuit condition. The stiffness can determine how much displacement the specimen deforms to and how much power is delivered into the specimen for a given input force.

Figure 42 shows the data of s_{33}^E, s_{33}^D, d_{33} and g_{33} as a function of stress at 10 Hz and 400 Hz for PZT-5H, PZN-PT and PMN-PT. As can be seen, the material properties is a strong function of the driving stress but only a weak function of the driving frequency. Each data set can be fitted using a polynomial function of compressive stress T in MPa:

$$d_{33}^{PZT5H} = 679.186002848395 + 11.035909394745T - 0.284348262482T^2 \qquad (22)$$

$$d_{33}^{PMNPT} = 958.755747212946 + 17.235290861948T - 0.720369973552T^2 \tag{23}$$

$$d_{33}^{PZNPT} = 1576.85195818796 + 47.839603507060T - 1.819780741040T^2 \tag{24}$$

$$g_{33}^{PZT5H} = 0.02019638833093 + 0.00012746071745T - 0.00004193544098T^2 +$$
$$0.000000232408964T^3 - 0.00000005774398T^4 + 0.00000000053195T^5 \tag{25}$$

$$g_{33}^{PMNPT} = 0.02701591972747 + 0.00051050517351T - 0.00010711068484T^2 +$$
$$0.00000316972139T^3 - 0.000000002843305T^4 \tag{26}$$

$$g_{33}^{PZNPT} = 0.036175902695820.00071800517313T - 0.00019501199244T^2 +$$
$$0.00000674820968T^3 - 0.00000007130516T^4 \tag{27}$$

$$s_{33}^{E\,PZT5H} = 23.75337763095130 + 0.117736406993360T - 0.00526783476887T^2 \tag{28}$$

$$s_{33}^{E\,PMNPT} = 39.28579064087646 + 0.706615572652481T - 0.00809493733445T^2 \tag{29}$$

$$s_{33}^{E\,PZNPT} = 78.07645545991812 + 0.71686410336253T0.00661863533739T^2 \tag{30}$$

$$s_{33}^{D\,PZT5H} = 10.27658431341368 - 0.03504827381062T + 0.00128025014264T^2 \tag{31}$$

$$s_{33}^{D\,PMNPT} = 15.52573085816073 + 0.599939995921106T + 0.01433878548882T^2 \tag{32}$$

$$s_{33}^{D\,PZNPT} = 15.79245215972361 + 0.10767853031487T - 0.15070056364832T^2 +$$
$$0.040328220016655T^3 - 0.00179313481186T^4 + 0.000023619910797T^5 \tag{33}$$

The variation in properties for the single crystal data at different frequencies might be due to the variation of different samples. A slight misalignment of the cutting of a single crystal specimen may result in a large variation in material properties, while the cutting has no major effect on a polycrystalline PZT-5H specimen. Amongst the four constants, g_{33} decreases most rapidly as the compression is increased. This also results in the sharp degeneration of the coupling coefficient k_{33} shown in Figure 43 and defined as:

$$k_{33}^2 = \frac{d_{33}g_{33}}{s_{33}^E} \tag{34}$$

3.3.4 Characterization of Material Energy Density

Using the rectifying circuit shown in Figure 40, one can obtain the power output by

$$P = i \times V_{DC} \tag{35}$$

where V_{DC} is the DC voltage of battery and i is the current flowing into the battery. The specimens of the different materials were tested under different frequencies, forces and battery voltages. Using the generalized material properties measured earlier, one can simulate the response using the Simulink model developed earlier.

Figures 44-(a), -(b) and -(c) show good correlation between the measured and simulated response of PZN-PT under low stress at which the material behaves linearly. Unfortunately, the material does not behave linearly under high stress conditions. The simulation does not correlate well to the measured data, as shown in Figures 44-(c), -(d) and -(e). This is due to the nonlinearity of the material. Figure 45 shows the measured and simulated power as a function of the battery voltage at both low stress and high stress conditions. As can be seen again, the linear simulation predicts the power output much better at
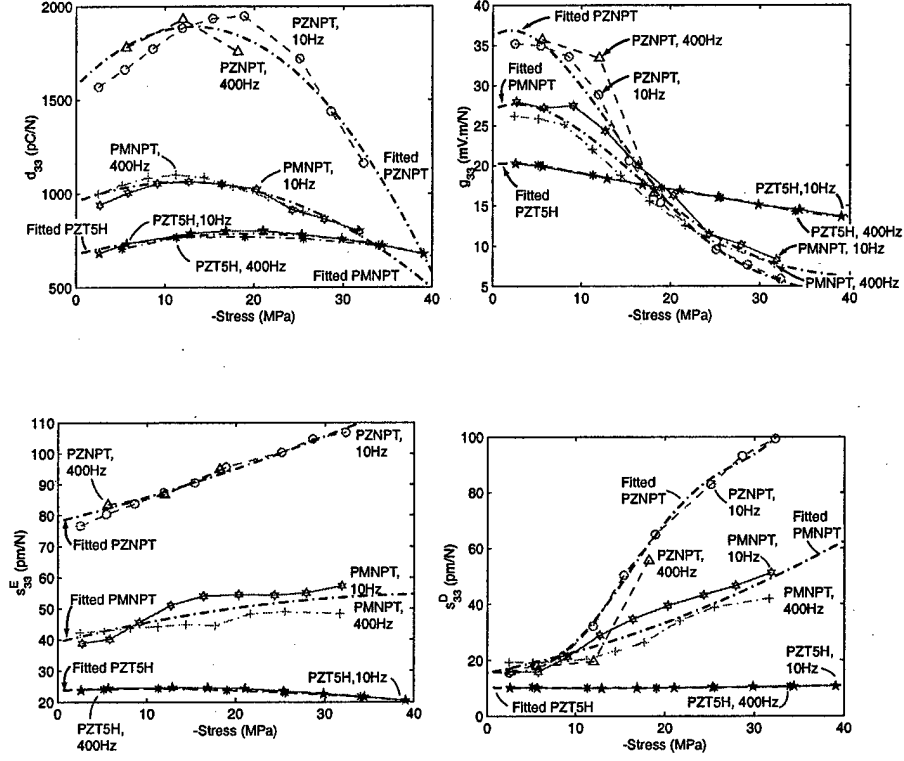
Figure 42: Generalized material constants d_{33}, g_{33}, s_{33}^E and s_{33}^D as a function of stress at 10Hz and 400 Hz for PZT-5H, PZN-PT and PMN-PT.

low stress than at high stress.

In order to compare the harvested electric energy for different sizes of specimens and different driving frequency, it is convenient to normalize the power P by the frequency f and the specimen volume V and to define an energy density:

$$\Omega = \frac{P}{fV} \tag{36}$$

If the material properties are linear, the maximum energy density obtained using rectifying circuitry is proportional to the square of stress and is given by [34]:

$$\Omega_{max} = \frac{1}{4}k_{33}^2 T_{33}^2 s_{33}^E \tag{37}$$

or

$$\Omega_{max} = \frac{1}{4}g_{33}d_{33}T_{33}^2 \tag{38}$$

where T_{33} is the compressive stress. Figure 46 shows the maximum energy density of different materials as a function of compressive stress using rectifying circuitry. The dashed lines are obtained assuming the materials are linear; however, the experiment shows that the materials degenerate at higher stress. The generalized material constants are also useful to predict this result. Substituting Eq. 22, 23, 24,

61
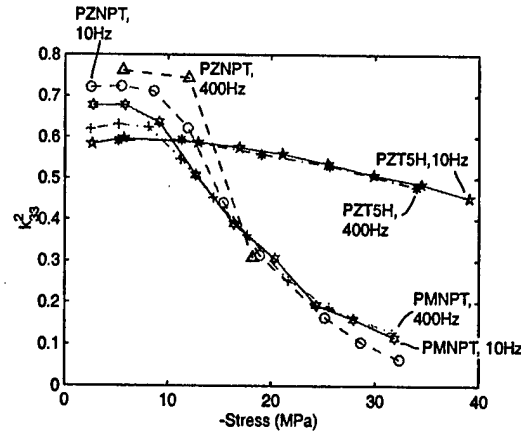
Figure 43: k_{33}

25, 26 and 27 into Eq. 38 yields a good approximation of maximum energy density, as shown in Figure 46.

3.3.5 Accomplishments

In this work, the material properties for application to the energy harvester were tested and show a significant function of applied stress but not a significant function of frequency. These material properties can be presented as generalized material constants as a function of stress, as shown in Figure 42. For PZT-5H, the material starts to depole when the compression is higher than 22MPa, while the material starts to degenerate at stress higher than 11Mpa for PZN-PT, and 15MPa for PMN-PT. Among others, PZN-PT at low stress has the largest energy density. However, at higher stress levels, the results indicate that ceramic piezoelectric materials such as PZT-5H may be a better alternative, as also shown in Figure 46.
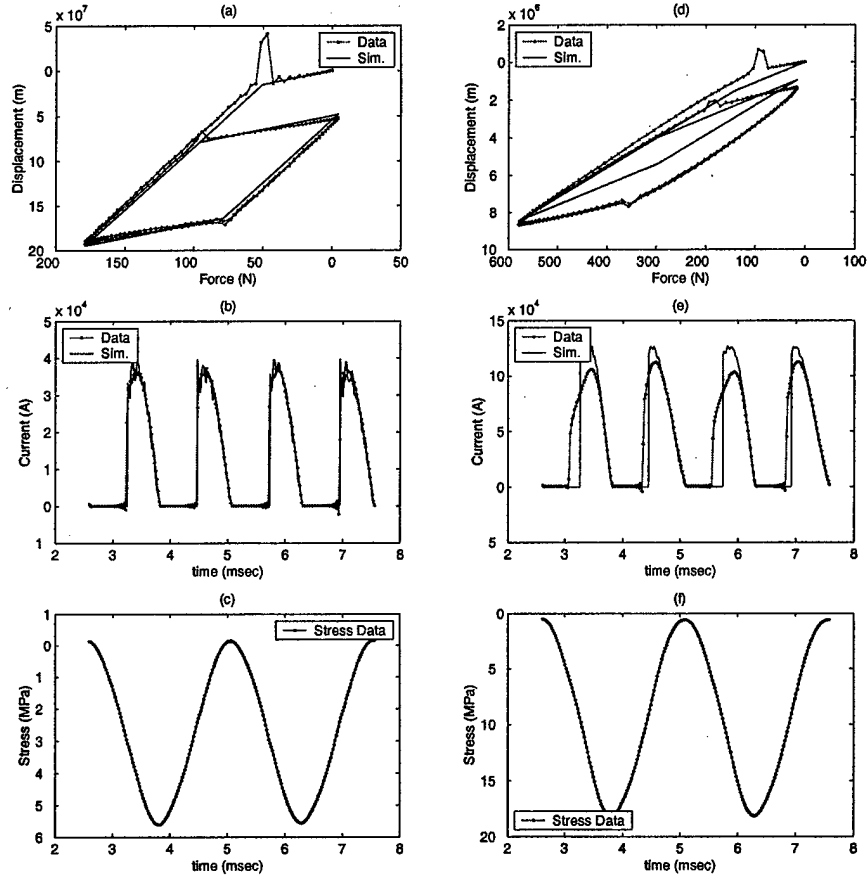
Figure 44: Data and simulation of low and high stress response (PZN-PT): (a) the force-displacement relation at low stress, 400Hz, V_{DC} =300V, (b) the simulated and measured current at low stress 400Hz, V_{DC} =300V, (c)driving force history of low stress condition, (d) the force-displacement relation at high stress, 400Hz, V_{DC} =400V, (e) the simulated and measured current at high stress 400Hz, V_{DC} =400V, (f)driving force history of high stress condition.
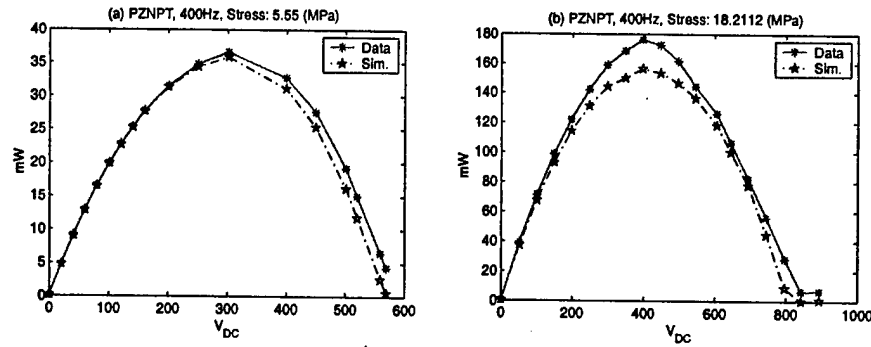
Figure 45: PZN-PT: Power vs. V_{DC}
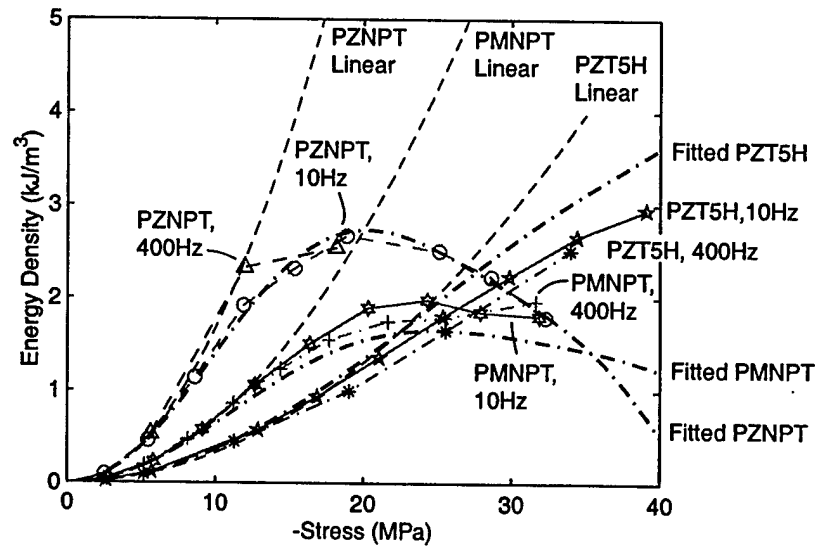
Figure 46: Maximum energy density using rectifying circuitry. The curves labeled as "Fitted" are obtained from Eq. 38 using generalized material constants described in Eq. 22, 23, 24, 25, 26 and 27. The curve labeled as "Linear" are obtained from Eq. 38 assuming constant material coefficients d_{33} and g_{33} at zero stress

64

3.4 Identification of SOI Membrane Stress Limits

3.4.1 Objectives

The drive elements and valves in the MHT device rely on thin single crystal silicon membranes. The membranes are fabricated by patterning the backside of a silicon-on-insulator (SOI) wafer and deep reactive ion etching (DRIE) to the buried oxide which acts as an etch stop. Maximizing the strength of the membranes is critical for device operation, thus a systematic study was performed to measure the strength of membranes fabricated using this technique. The primary objectives of this study was to understand the resulting etched geometry and to measure the fracture strength of such structures. Understanding the geometry and knowing the fracture strength are essential in designing MHT devices.

3.4.2 Accomplishments

The test structure employed mirrored the actual pistons in the MHT device. Figure 47 is a scanning electron microscope (SEM) micrograph of a test specimen that has been cross-sectioned. The specimen consists of an etched circular trench that forms a central boss supported by a thin tether membrane. A test system that applies a controlled displacement at the center of the central boss and measures load was constructed. Specimens were loaded until failure and the load measured. Through SEM examination of the etched features, the geometry of the fillet was determined so that it could be accurately modelled in finite element analyses of the test specimen and the device. Figure 48 is a SEM micrograph of the fillet at the base of the etched trench and demonstrates that the fillet has an elliptical shape.
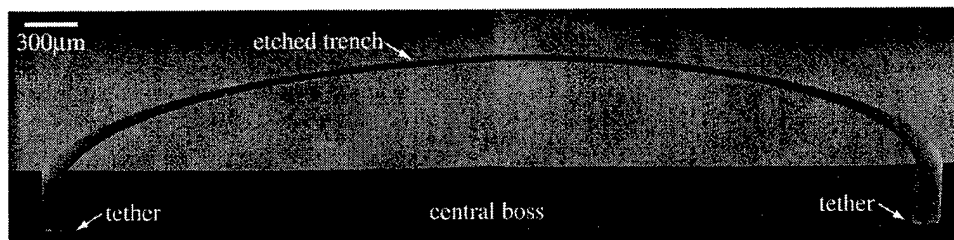
Figure 47: A SEM micrograph showing the fracture test specimen employed in this work.

A total of 129 specimens were fabricated and tested according to the above procedure. SOI wafers from two manufacturers, Motorola and BCO Technologies (now Analog Devices), were used in the tests. In addition, the study sought to address whether the oxide layer at the base the etched trench should be removed. Thus, there are four groups of specimens that were fabricated and tested. Details about the groups and the measured fracture strengths are listed in Table 3. The scatter in the strength results listed is result of variability in the fabrication process.

From the results listed in Table 3 two clear trends are observed. First, it is clear that removal of the oxide at the base of the trench reduces the fracture strength of the membranes by approximately 0.3 GPa. The other fact that is observed is that membranes fabricated from BCO SOI wafers are significantly stronger than the Motorola SOI wafers employed. This data and these trends provided critical information that guided the fabrication of actual MHT devices. Namely it lead to the use of all BCO SOI wafers for critical membrane elements and second it provided design stress guidelines. Further information about this work is provided in reference [27].
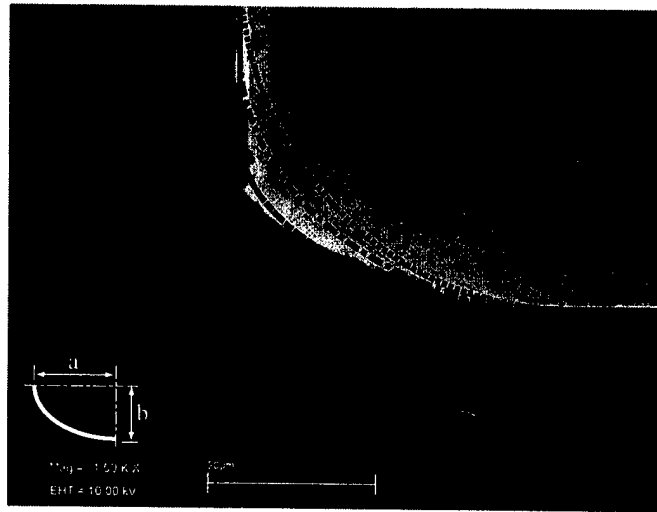
Figure 48: Typical shape of etched fillet.

Table 3: Fracture strength values.

Group	Manufacturer	Buried oxide present?	Mean (GPa)	C.V.	Number of Specimens
I	BCO	present	1.67	0.27	10
II	Motorola	present	0.77	0.22	12
III	BCO	removed	1.30	0.37	19
IV	Motorola	removed	0.48	0.26	88

3.5 Contributions: Supporting Experimental Investigations

A number of experimental studies were conducted to assist in the design of the MHT device. The contributions made with these studies are:

1. Empirical models for flow losses through microfabricated poppet-type valves were obtained. These results were found to correlate very well with eventual flow testing of the MHT valve units.

2. A technique was developed for the bubble-free filling of the Hydraulic Amplification Chambers (HAC's) of the MHT device. This technique proved to be robust and all devices tested were properly filled.

3. A static sealing option was introduced for the HAC, and used in the static hydraulic amplification tests.

4. A dynamic sealing technique was also introduced, which enabled pressure balancing of the active valve structures. This sealing technique proved to be very reliable for bench top testing.

5. A detailed characterization was performed on the energy harvesting capabilities of various piezo-electric materials, for use in the MHT device. For the final device, the chosen material was single crystal PZN-PT.

6. The strength of silicon membrane tethered structures was determined through extensive test specimen preparation and testing. A design value of $1 GPa$ was determined as a result of these tests. In addition, the tests also reconfirmed that a good fillet feature is essential to producing a strong membrane.

4 Heel Strike Energy Harvesting Mechanism

4.1 Overview

This section presents a brief summary of a set of studies performed on the feasibility of a heel packaging system for an energy harvesting device. A final design was conceived that could function as a bench-top testbed for testing the functionality of a harvesting device in a packaged system. Therefore, for this design, the requirements of light weight, durability and environmental protection were not addressed. The schematic layout for such a heel strike harvesting mechanism is shown in Figure 49, and the final design is shown in Figure 50.
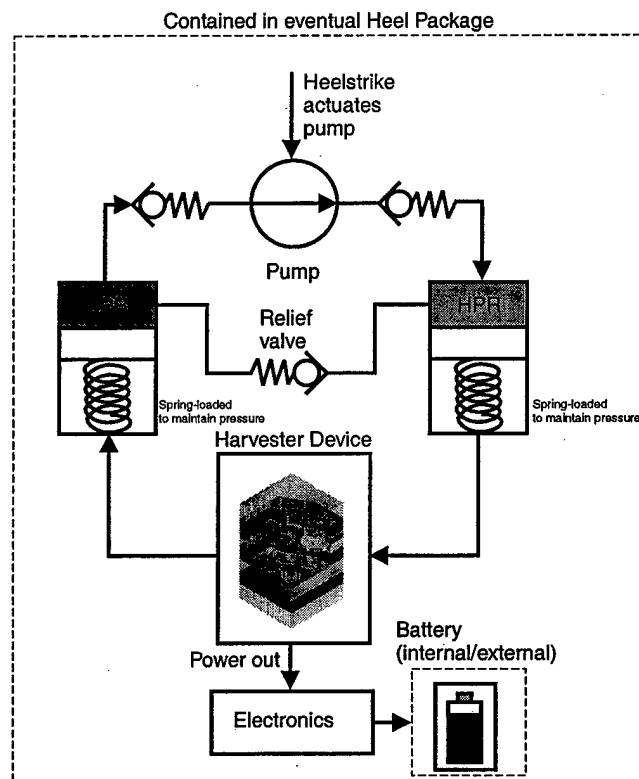
Figure 49: Schematic of the harvester heel strike packaging layout.

4.2 Design of the bench top heel packaging system

Parameters The following parameters were used in the mechanical design of the bench top heel packaging system.

- Harvester Pressure: $\sim 2.3 MPa$

- Harvester Flow: $2.7 ml/s$
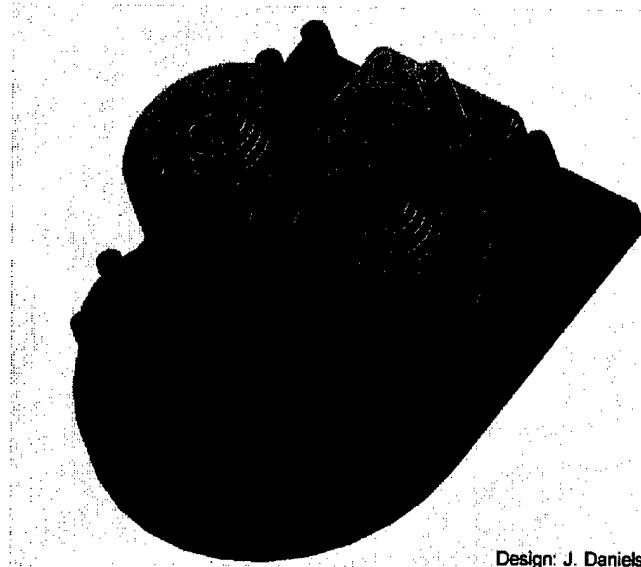
Design: J. Daniels

Figure 50: 3D view of a heel packaging concept for bench top demonstration. In this case, conventional small hydraulic cylinders were used.

	Low Pressure Reservoir	High Pressure Reservoir
Minimum Pressure (MPa)	0.1	1.80
Maximum Pressure (MPa)	0.3	2.30
Minimum Force (N)	28.5	513
Maximum Force (N)	85.5	656

Table 4: Reservoir Pressures

- Mass of Person: $70kg$

- Weight of Person: $686N$

- Actuator Deflection: $1cm$

- Kinematic Fluid Viscosity: $0.65cSt$

- Fluid Density: $780kg/m^3$

The pump unit In order for the energy harvester to operate properly, the pump pressure must vary between 2.3E+6 Pa. For this bench top demonstration design, an off-the-shelf pump cylinder from Compact Air Products Inc (http://www.compactair.com) with a stroke of 1cm was specified.

Reservoirs The reservoirs were also specified to be piston-type devices from Compact Air Products. The reservoirs had the following pressures, based on the operating conditions of the pump:

From the values in Table 4, return springs were specified for the reservoirs. For this application, conical springs were specified due to their smaller compressed length and also their stiffening nature.

This provides additional energy storage in a more compact configuration. Both spring for the HPR and the spring for the LPR have 5 coils in a cone configuration, which fit inside one another thus making the dead length approximately equal to the spring thickness.

The potential of using metal bellows For the specified pressures, strokes and life cycles, it was not possible to find off-the-shelf metal bellows that would satisfy the requirements of the pump or the reservoirs. Formed metal bellows proved to have a rather short fatigue life and limited stroke, despite their high pressure capabilities. Welded metal bellows, on the other hand, were able to provide, barely, the stroke needed, but not at the desired pressures. Ultimately, in such a heel, bellows would most likely be preferred, but further studies will be needed to locate or develop suitable bellows that will satisfy the specifications.

System design The mechanical design combined the HPR, the LPR, the pump as well as the chip packaging (or flow restrictor in case a simple substitute for the harvester was needed) on a base plate that included the flow channels between the various reservoirs. An exploded view of this design is shown in Figure 51.
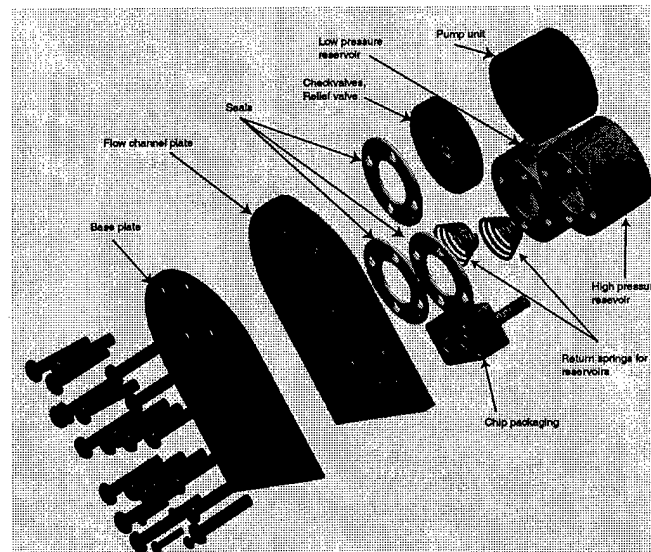
Figure 51: Exploded view of the heel packaging concept. The conical coil springs ensure that a spring can be made with sufficient stiffness that also remains compact with a small compressed length. These springs are also nonlinear, stiffening, which aids in providing sufficient stiffness in a compact form.

4.3   Contributions: Heel Packaging Design

With respect to the heel strike power harvesting mechanism, the following was achieved:

1. A preliminary design for a bench top heel packaging unit was produced.

2. A model for the heel strike harvesting mechanism was also produced.

In this project, the effort was focused mostly on development of the core technologies centered around the harvesting device itself. This study has proven that a suitable heel strike mechanism for an energy harvesting device could be conceived, and that the mechanical design for such a heel is feasible. This mechanism was not fabricated, with everything suggesting that the most challenging part of heel strike power generation using MHT technology was the design and fabrication of the MHT device itself.

5 Device Fabrication and Assembly

5.1 Fabrication and Assembly Procedures for Chip-Level Harvesting Device

5.1.1 Overview

The full MHT harvesting system is fabricated using a combination of microscale (silicon patterning and etching) and macroscale (piezoelectric material integration) procedures. The chip-level harvesting device consists of multiple layers of silicon and glass (Pyrex 7740) with integrated piezoelectric elements, all bonded together to form the important structural features of the device. These features are the tethered-piston piezoelectric drive element, the enclosed hydraulic amplification chamber, the valve membrane and orifice structure, and the fluid channels connecting the inlet and outlet valves to the central harvesting chamber.

A cross-section of a full MHT system, with an embedded harvesting chamber and two multi-layered active valves, is shown in Figure 52. Layers 1, 3, 6, and 9 of the device are each borosilicate glass (Pyrex 7740), the features of which are formed through wafer-level ultrasonic machining. Layers 2 and 8 are formed from standard silicon wafers and are etched using deep-reactive ion etching procedures. Layers 4, 5, and 7 are created from silicon-on-insulator (SOI) wafers. The drive element tethers supporting the piston structures in Layers 4 and 5 and the valve membrane and cap structures in Layer 7 are produced using deep-reactive etching, with the buried oxide acting as an etch stop for precise control of tether and membrane thicknesses. The three primary bonding mechanisms used to realize the device are silicon-silicon fusion bonding, silicon-glass anodic bonding, and silicon-piezoelectric material eutectic bonding.
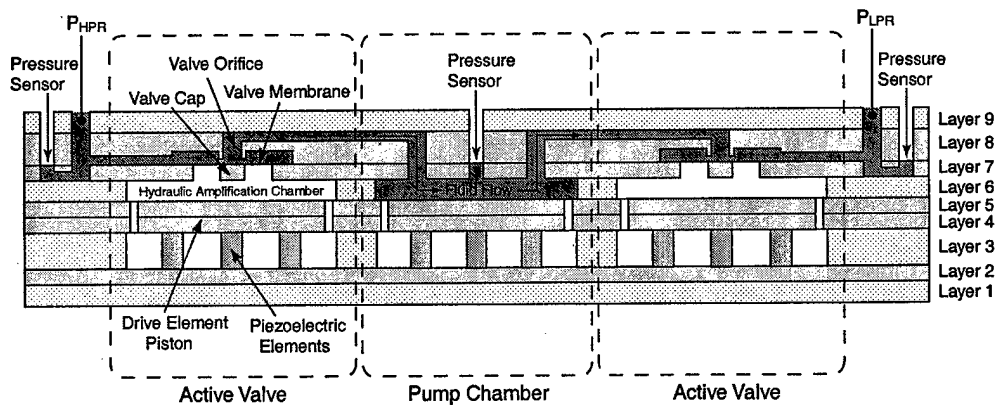
Figure 52: Cross-section schematic of a nine-layer multiple wafer MHT system with two embedded active valve structures. Realization of this system requires robust bonding of silicon-to-silicon and silicon-to-glass at the wafer-level and integration and bonding of piezoelectric material elements with silicon at the die-level.

73

5.1.2 Challenges and Procedures

The critical challenges associated with the fabrication and assembly of this multi-layer harvesting device were: (1) etching of the high-aspect ratio features in the silicon-on-insulator wafers to form the tethered drive element piston and valve membrane structures, (2) wafer-level silicon-silicon fusion bonding and wafer-level silicon-glass anodic bonding, (3) preparation, integration, and bonding of the bulk piezo-electric material elements within the drive element structure, (4) die-level assembly and bonding of the silicon and glass layers, and (5) fluid filling and sealing of the hydraulic amplification chamber. The procedures developed to overcome these challenges are detailed in the following sections.

Etching of the Tethered Drive Elements and Valve Membranes The drive element tethers and valve membranes within the harvesting chamber and active valves are designed to be quite thin (on the order of $7 - 10 \mu m$). To achieve precise dimensional control of these features, SOI wafers containing a buried oxide layer a preset distance from one side of the wafer were used. In performing deep etches into the silicon wafer down to the buried oxide layer, it was critical that the surface roughness of the etch and the tailoring of fillet radii profiles at the base of the etched profiles be well-controlled so as to maintain strength and robustness of the thin-membrane structures. Figure 53 illustrates etch profiles at the SOI interface of a typical drive element piston that can result, depending on the process chosen and care given to performing the etch. Ideally, one would like to create a fillet radius between the thin tether and the much thicker ($\sim400 \mu m$) central piston structure to minimize stress concentrations, as shown in Figure 53(c). It is essential to avoid etch profiles such as the sharp corner shown in Figure 53(b) and the "footing" or "notching" profile shown in Figure 53(d). These serve to magnify stresses at these interface regions, thereby compromising the overall strength of the structure.

Considerable research work has been done in developing and optimizing deep etching processes for single-crystal silicon materials [21] [22]. The Deep-Reactive Ion Etching (DRIE) process used to create the MHT harvesting device is known as the Bosch Process [21]. This method involves repetitive cycles of plasma etching and passivation to create high aspect ratio deep trenches in silicon. Using photoresist as a masking agent, a timed plasma etch using SF_6 is carried out. Following this timed etch, a passivating film using C_4F_8 is deposited over all exposed surfaces of the wafer, including the etched trench bottom and sidewalls. During the next timed plasma etch, this passivating film is preferentially removed from the bottom of the trenches through ion bombardment, while the film on the sidewalls remains intact. This cyclic process is repeated until the buried-oxide etch stop layer is reached. At this juncture, carefully monitoring of the etch process is performed to ensure that fillet radii of a desired size (based on modeling specifications) are created. Figures 53(e)-(g) show SEM images of a successfully etched drive element piston structure with properly tailored fillet radii.

This final "fillet tailoring" step is a difficult one because once the silicon has been etched away such that portions of the oxide are visible, very little time is required for lateral etching of the remaining silicon above the oxide layer to be completely etched away, resulting in potential "footing" profiles at the interface. The rapid lateral etching has been studied and investigated by numerous individuals, and it is believed to result from plasma charging effects at the silicon/oxide interface [23] [24] [25]. Consistently controlling these fillet profiles is extremely hard to achieve, as etch parameters such as etch time, passivation time, SF_6 flow rate, electrode power during etching, electrode power during passivation, and C_4F_8 flow rate must be tuned and optimized. Procedures were developed within this program to adequately control fillet radius profiles within the membrane structures of the MHT device.

Wafer-Level Bonding For the multi-layer active valve structure presented in this thesis, various silicon-silicon and silicon-glass wafer-level bonds were performed. A silicon-silicon wafer-level fusion bonding process was used to bond Layers 4 and 5 together to form Stack 4-5 and Layers 7 and 8 together to
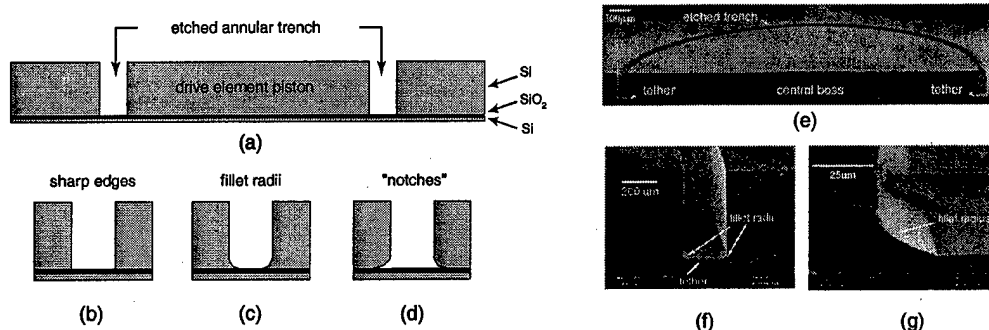
Figure 53: Etching of a typical drive element piston structure: (a) cross-section view of drive piston, (b) sharp corner etch features, (c) fillet radius features, and (d) "notching" or "footing" features, (e) SEM cross-section view of SOI piston structure, (f) SEM close-up of etched trench, and (g) further SEM close-up of fillet radius feature. In this structure, a $20 - 25\mu m$ fillet radius was achieved. Debris in background was generated during die-saw procedures.

form Stack 7-8. A silicon-glass wafer-level anodic bonding process was used to bond Layers 1 and 2 together to form Stack 1-2, Stack 4-5 and Layer 6 together to form Stack 4-5-6, and Stack 7-8 and Layer 9 together to form Stack 7-8-9. Following these wafer-level bonding steps, the stacks were die-sawed into individual dies and cleaned in preparation for die-level bonding and piezoelectric material integration. Figure 54 illustrates the various wafer-level silicon-silicon and silicon-glass bonding steps.
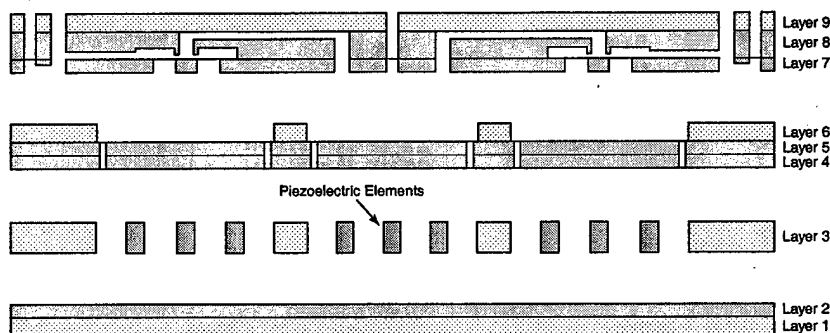
Figure 54: Wafer-level silicon-silicon fusion and silicon-glass anodic bonding steps are carried out prior to piezoelectric material integration.

The silicon-silicon fusion bonding process used to create wafer-level stacks for the active valve device is a well developed process and consists of three primary steps [26]: (1) preparation and treatment of the silicon wafer surface to produce a hydrophilic surface, (2) alignment and adhesion of two wafers together (weak van der Waals or hydrogen bonds maintain wafer-wafer adhesion) in a clean room-temperature environment, either in air, inert atmosphere, or vacuum , and (3) high temperature annealing of the wafer stack at 1000°C to promote strong covalent bonding. The strength of this fusion bond is dependent on the annealing temperature and time [27]. Paramount in the bonding process is the cleanliness of the silicon wafers prior to bonding and of the alignment and bonding apparatus itself. Particulate matter

present between the silicon wafers during adhesion can result in significant defect regions characterized by little or no bonding.

The silicon-glass anodic bonding process used to create wafer-level stacks also is a well-developed process. This process involves three primary steps: (1) preparation and cleaning of the silicon and glass surfaces using a piranha soak and an oxygen ashing step, (2) alignment and clamping of the two wafers together, and (3) application of a voltage (1000V) across the wafer interface at elevated temperature (300°). The negative electrode is applied to glass wafer surface not being bonded with the silicon wafer held at ground potential. As for the fusion bonding process, cleanliness of the wafers and the bonding apparatus is paramount for achieving high-quality and low-defect wafer-level bonds.

Integration of the Bulk Piezoelectric Elements Integration of the piezoelectric elements within the device constitutes a critical task in the assembly of the active valve device. The top and bottom surfaces of the piezoelectric elements are covered with a thin-film gold-tin (Au-Sn) eutectic alloy for bonding to the adjoining silicon layers at an elevated temperature. In order to achieve good bonding over the complete interface area, the piezoelectric material must possess smooth top and bottom surfaces. A rough surface of the piezoelectric material (and therefore of the metallized layer), would result in only pinpoint contacts between the piezoelectric material and the silicon and therefore a weak bond. Prior to bonding, sizing of the piezoelectric elements with respect to the surrounding Layer 3 glass and etching of seats in the Layer 2 silicon to compensate for thickness mismatch between the piezoelectric material and glass is critical for ensuring a deflection of the drive element piston below levels of fracture stress in the tethers. Each of these piezoelectric material integration issues is covered in detail in the following sections.

Piezoelectric Material Preparation Virgin piezoelectric materials are obtained from vendors in the form of thin plates, each with a thickness of $\sim 1.1mm$ and diameter between 1 cm and 5 cm. As received, these plates possess a surface roughness as large as $5\mu m$. In order to achieve adequate eutectic bonding during device assembly, a surface roughness near $0.5\mu m$ is required prior to metallization. To achieve this, the piezoelectric material plates are polished using coarse and fine grain diamond slurry polishing procedures. During polishing, each plate is sized to yield a thickness of $1mm \pm 10\mu m$ with thickness variation across the plate of $\sim 2\mu m$. Prior to metallization, the material plates are solvent cleaned with a series of acetone, methanol, and isopropanol steps. Additionally, a further cleaning soak in a 20:1 water:nitric acid solution is carried out for 1 minute to remove particulate matter. At this point, the piezoelectric material plates are ready for metallization.

AuSn Eutectic Bonding To bond mechanically and to connect electrically the piezoelectric material cylinders to the adjoining silicon layers in the active valve device, a reliable bonding mechanism must be employed. This bonding mechanism must allow for tight dimensional control over the bond layer thickness and allow for a bonding temperature and environment that is compatible with the rest of the die-level assembly process. Numerous bonding methods that could potentially work in this device, ranging from polyimides and epoxies to brazing and soldering to gold-based eutectic alloys, have been presented in the literature. A detailed discussion of these research efforts, with application toward the development of MHT technology, is found in [27]. The resulting conclusion of initial work by Mlcak [28] and the subsequent work by Turner [27] was to employ a thin-film AuSn eutectic alloy (composition: 80 wt. % Au and 20 wt. % Sn) as the bonding mechanism within MHT devices.

A four layer film structure on the piezoelectric material and a three layer film structure on each of the adjoining silicon layers is deposited in preparation for bonding, as shown in Figure 55(a). The four layer structure on the piezoelectric material consists of 50 nm Ti, 250 nm Pt, 4000 nm AuSn, and 50 nm Au. The Ti serves as an adhesion layer, the Pt as a diffusion barrier, and the final Au as a capping

layer to prevent oxidation of Sn in the AuSn alloy. The AuSn layer, chosen to be thick enough (4 μm) to compensate for the piezoelectric material surface roughness ($\sim 0.5 \mu m$), is sputtered from an alloy target with 80 wt. % Au and 20 wt. % Sn composition. Sputtering is chosen over evaporation because sputtering allows the stoichiometry of the target to be maintained in the deposited film [29]. The three layer Ti-Pt-Au structure on each of the adjoining silicon pieces enables the eutectic alloy to wet the silicon and is deposited on the die-level using e-beam evaporation procedures.

Dicing/Core-Drilling of Piezoelectric Elements Following deposition of the eutectic alloy, the metallized piezoelectric material plates are core-drilled or diced to produce either cylindrical or square piezoelectric elements. As detailed in subsequent chapters of this thesis, devices integrating both cylindrical and square elements have been successfully fabricated and tested. The advantage of using square piezoelectric elements over cylindrical ones is that the process of dicing a piezoelectric material plate in a grid pattern results in the production of 2-3 times the number of elements than can be produced from core-drilling from a identical size plate. By sheer numbers and by the fact that closely located elements will possess almost identical thicknesses (relatively insensitive to variations in thickness across the material plates), the use of square elements increases the odds of being able to select multiple elements of identical thickness to insert into drive element structures. Once the material plate has been either core-drilled or diced, the resulting piezoelectric elements are individually measured for thickness using a hand-held precision micrometer. By calibrating the micrometer before each measurement with a precise thickness gauge block (1mm $\pm$ 0.01 μm) and averaging repeated series of measurements of the same elements, these thickness measurements are estimated to be accurate within $\sim 0.5 \mu m$. The elements are then organized and sorted according to the thickness.

Etching of the Piezoelectric Element Seats One of the critical issues during integration of the piezoelectric material elements is guaranteeing an upward deflection of the drive element piston large enough to ensure a preload on the eutectic alloy interface during bonding, yet small enough to ensure stresses in the piston tethers below the critical value of 1 GPa. Typically, in the drive element structures designed, fabricated, and tested in this thesis, the piston tethers will reach a tensile stress of 1 GPa for displacements near $\sim 9 \mu m$. Therefore, at any time during the bonding, poling, and operation of a device, it is desired to maintain piston displacements no greater than a safe value of $\sim 6 \mu m$. In terms of preload on the eutectic interface, it is desired to ensure a "piston push-up" of $\sim 2 \mu m$. These requirements therefore dictate that at the instant of eutectic bonding, the piezoelectric element(s) beneath the drive element piston must be forcing the piston upward by $\sim 2 \mu m$ and that for all time after that the piston must not be forced to displacements greater than $\sim 6 \mu m$. Considering that this $4 \mu m$ range is 0.4% of the total piezoelectric element thickness, this task represents quite a challenge.

In preparation for piezoelectric element integration, the Layer 3 glass wafer was diced into individual dies, and each of these dies was measured using the micrometer. As received from the vendor, each of the ultrasonically-machined Layer 3 glass wafers possesses a thickness between 967 μm and 974 μm, with thickness variation across a given wafer less than $1 \mu m$. At the time of integration, since the piezoelectric elements (with deposited eutectic alloy films) have thicknesses near 1000 μm and the Layer 3 glass dies have thickness near 970 μm, it is necessary to have the capability to remove this thickness difference of $\sim 30 \mu m$ between the piezoelectric material and the surrounding glass. Ideally, once integrated into the device, the piezoelectric elements' top surfaces should be slightly above level with the Layer 3 glass top surface so as to produce predictable upward displacement of the drive element piston from its equilibrium position ("push-up").

This thickness matching is achieved by plasma etching shallow seats for all of the piezoelectric elements in the Layer 2 bottom silicon wafer, as shown in Figure 55(b). An iterative process of carefully timed etches followed by depth measurements using a scanning profilometer can result in etch depth

77

(a)   (b)
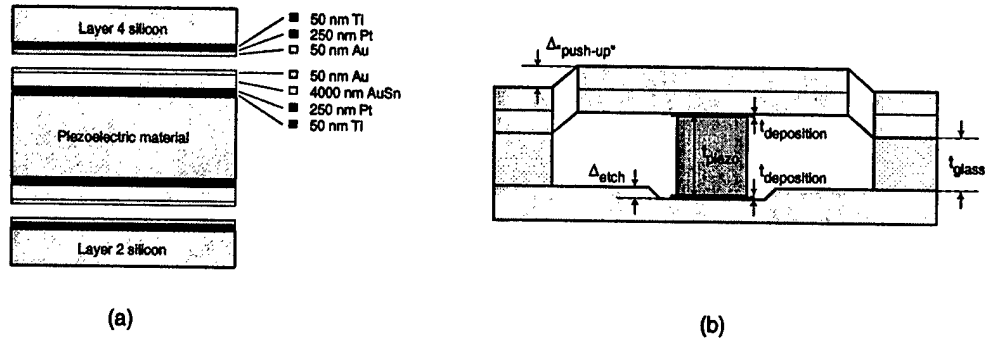
Figure 55: Piezoelectric integration within the drive element structure: (a) eutectic alloy deposition on the piezoelectric material and adjoining silicon layers. The piezoelectric material contains a 4 layer film structure and each of the silicon layers contains a 3 layer film structure, and (b) Tolerancing of the piezoelectric element within the structure by plasma etching shallow seats in the Layer 2 bottom silicon die. Precise control of the etch depth was necessary to achieve the desired "push-up" of the drive element piston.

control to within $\sim 0.5 \mu m$. With this capability to compensate for thickness mismatch between the piezoelectric elements and the surrounding Layer 3 glass, proper "push-up" of the drive element piston can be achieved during assembly and bonding. On the die-level, each Layer 2 silicon die is matched with a pre-measured (t_{piezo}) grouping of one or three piezoelectric elements (depending on whether a single or multiple piezoelectric valve is being fabricated) and with a pre-measured (t_{glass}) Layer 3 glass die. With knowledge of the three-layer film thickness $t_{deposition}$ that will subsequently be deposited on the underside of the drive element piston in Layer 4 and on the top surface of the "to be etched" seats in Layer 2, and with the value of $\Delta_{"push-up"}$ desired after device assembly, the required etch depth (Δ_{etch}) in Layer 2 is determined, according to Equation 39.

$$\Delta_{etch} = t_{piezo} + 2t_{deposition} - t_{glass} - \Delta_{"push-up"} \tag{39}$$

Following etching of the seats, the Layer 1-2 silicon dies were cleaned and combined with Stack 4-5-6 silicon dies for deposition of the three-layer Ti-Pt-Au film structure required for eutectic bonding. This deposition was performed using e-beam evaporation through specially-machined shadow masks to allow for selective coating of the dies. For the Stack 4-5-6 dies, the underside of the drive element piston was coated, and for Layer 2 dies the inside of each of the etch seats was coated.

Die-Level Assembly and Bonding

Assembly and Bonding Procedure The final assembly of the MHT harvesting device was performed at the die-level. As shown in Figure 56(a), which illustrates the procedures through the building of one of the active valves, wafer-level etching and bonding procedures, followed by dicing of the stacks into individual dies result in the creation of a Stack 7-8-9 die, a Stack 4-5-6 die, a Stack 1-2 die, and a Layer 3 die. Additionally, piezoelectric material preparations create individual piezoelectric elements ready for insertion. It was desirable to perform these bonding steps at the die-level, rather than the wafer-level, so as to allow for individual measurements of the Layer 3 glass die thickness and to enable individual control of the seat etching in Layer 2. Additionally, die-level bonding significantly reduced the risk of

losing an entire multi-layer wafer structure during wafer-level processing. The die-level assembly process consists of four main steps, as shown in Figure 56(b), (c), (d).

1. Die-level anodic bonding of Stack 4-5-6 to Stack 7-8-9 at a temperature of 300°C and an applied voltage of 1000V across the Layer 6 - Layer 7 interface. This bond was performed at atmospheric pressure. Time of bond = approximately 2 minutes.

2. Die-level anodic bonding of Stack 1-2 to Layer 3 at a temperature of 300°C and an applied voltage of 1000V across the Layer 2 - Layer 3 interface. This bond was performed at atmospheric pressure. Time of bond = approximately 2 minutes.

3. Alignment and placement of one or more piezoelectric material elements within the Stack 1-2-3 die.

4. Simultaneous die-level anodic bonding of Stack 1-2-3 to Stack 4-5-6-7-8-9 and eutectic bonding of piezoelectric element(s) to Layer 2 and Layer 4 silicon. This bond was performed in a reducing atmosphere of $Ar-5\%H_2$ gas at pressure 10^{-2} torr and temperature 300°C. Additionally, a voltage of 1000V was applied across the Layer 3 - Layer 4 interface. Time of bond = approximately 2 minutes.

A reducing atmosphere was chosen for the final simultaneous anodic/eutectic bond to ensure no oxidation of the Sn within the AuSn alloy and to achieve a void-free eutectic bond [27]. Additionally, following this bond, the device was cooled under vacuum to ensure removal of all trapped gases within the bond. Completion of these four die-level bonding steps produced an MHT structure that was ready for filling of the hydraulic amplification chamber.

Assembly Jigs   The die-level anodic bonding discussed above was performed using the specially machined alignment and bonding jigs shown in Figure 57. The 1st-generation jig, shown in Figure 57(a), provided a large central contact surface onto which a die could be placed and the bottom surface held at either positive or negative voltage. An outer ring with attached spring clamps for clamping of one die onto another was held at ground potential. Once inserted into an oven, electrical contact was made through attached feet on the underside of the jig. Alignment, placement, and clamping of a dies and insertion of piezoelectric elements was facilitated by a vacuum chuck with 3-axis motion capability and a range in each of these directions of 1 cm. The 2nd-generation jig, shown in Figure 57(b), was more compact than the 1st-generation jig. It likewise provided electrical contact through thin wire clamps, but additionally allowed for edge alignment of the dies to a central area with ceramic insulating locator pins. Figure 58 illustrates an MHT device in the final bonding step using the 2nd-generation anodic bonding jig.

Fluid Filling/Sealing of HAC   Introducing fluid into the hydraulic amplification chamber of the active valve was a critical step in preparing the device for operation. Any bubbles or trapped residual gas within the amplification chamber would significantly increase its compliance, thereby eliminating efficient coupling between the drive element and valve membrane structure. The techniques and procedures used to fill and seal the device were presented in Section 3.2.

5.1.3   Conclusions

The following critical challenges associated with the fabrication and assembly of this multi-layer harvesting device were overcome:(1) etching of the high-aspect ratio features in the silicon-on-insulator wafers to form the tethered drive element piston and valve membrane structures, (2) wafer-level silicon-silicon

79
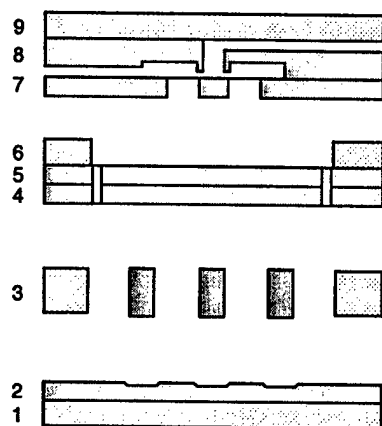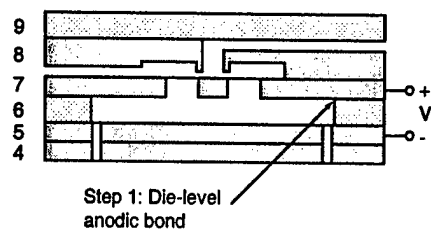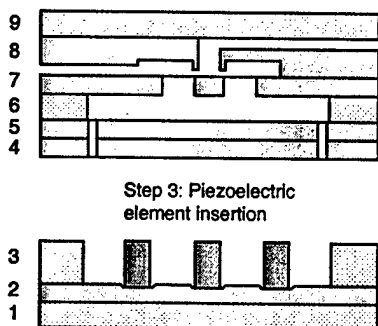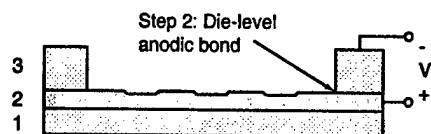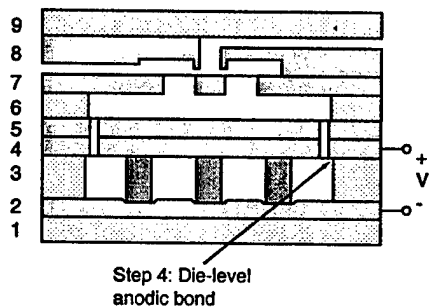
Figure 56: Die-level bonding procedure for the active valve portion of an MHT device: (a) beginning dies ready for assembly, (b) Step 1: anodic bonding of Stack 4-5-6 to Stack 7-8-9 ; Step 2: anodic bonding of Stack 1-2 to Layer 3, (c) Step 3: insertion of piezoelectric element(s), and (d) Step 4: anodic bonding of Stack 1-2-3 to Stack 4-5-6-7-8-9.
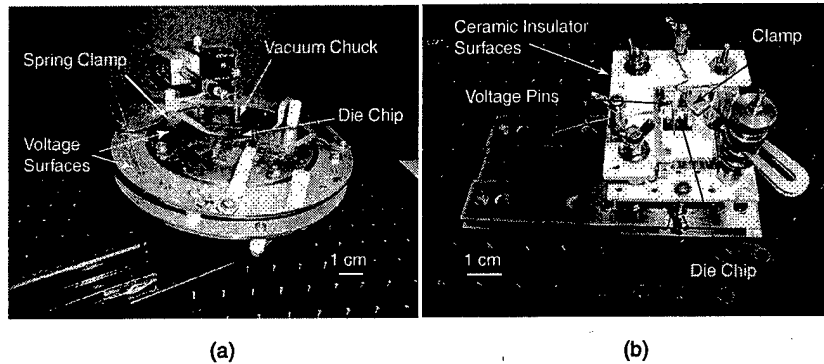
Figure 57: Die-level alignment and bonding jigs: (a) 1st-generation jig, (b) 2nd-generation jig.
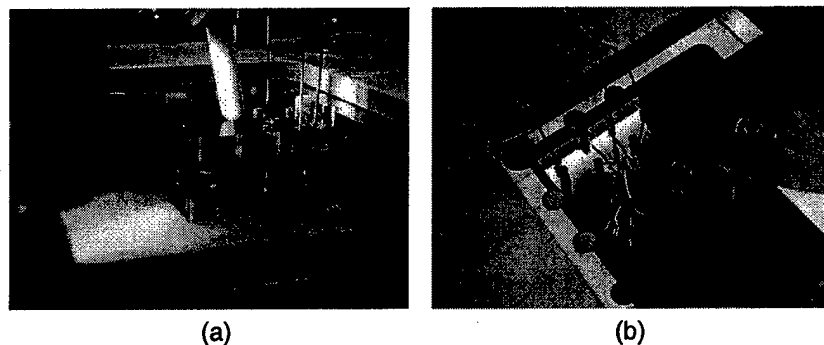
Figure 58: Electrical contact to an MHT device for anodic bonding: (a) side view of chip in jig and (b) top view of chip in jig. Electrical cantilever pins contact various layers of the device for bonding procedures.

fusion bonding and wafer-level silicon-glass anodic bonding, (3) preparation, integration, and bonding of the bulk piezoelectric material elements within the drive element structure, (4) die-level assembly and bonding of the silicon and glass layers, and (5) fluid filling and sealing of the hydraulic amplification chamber. With the developed procedures, multi-layer drive elements, active valves, and full MHT systems were successfully fabricated and assembled.

5.2 Chip-Level Harvesting Device Fabrication Process Flow

5.2.1 Overview

This section briefly outlines the fabrication approaches used to fabricate the silicon and glass layers of the MHT devices. The fabrication process required to produce a device can be divided into the following major subtasks:

- Silicon tethered membrane fabrication, using Silicon-On-Insulator (SOI) wafers.

- Structural silicon layer fabrication. Double-side polished wafers are used for this purpose.

- Glass layer fabrication by ultrasonic machining. The glass used was $Pyrex^{TM}7740$ by Corning.

- Wafer scale fusion bonding of silicon-silicon wafer pairs and anodic bonding of silicon-glass wafer pairs.

- Die-level alignment, integration of the piezoelectric material and anodic bonding to complete the assembly. (See Section 5.1)

5.2.2 Processes for the Silicon Layers

All silicon layers were fabricated in the MIT Microsystems Technology Laboratory facilities (MTL). The fabrication relied heavily on two ST Systems ICP plasma etchers for DRIE (Deep Reactive Ion Etching). The most challenging part of the silicon layer fabrication process proved to be the etching of the silicon tethered membrane structures that formed the moving parts of all the devices.

Start with SOI substrate.

After first deep etch and clean. Ready for second deep etch.

After oxidation. Align marks defined.

After second deep etch, fillet trimming and cleaning. Ready for oxide strip and bonding.

Silicon   Oxide
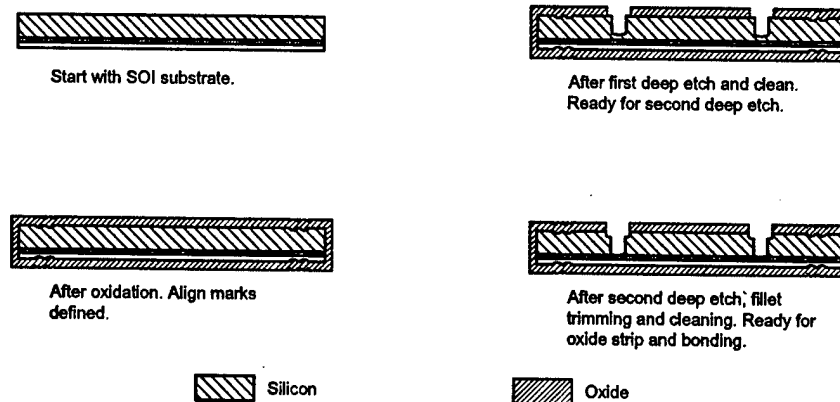
Figure 59: Selected steps of the process required to produce a tethered silicon membrane structure.

Figure 59 depicts the process used to produce the silicon membrane structures used in the devices characterized in this work. A scanning electron micrograph of such a structure is shown in Figure 47. The process flow for creating a structure like this from an SOI substrate can be summarized in the following steps:

1. Start with a Silicon on Insulator (SOI) wafer, double side polished. Device layer thicknesses of $7\mu m$ to $10\mu m$ were used. The wafer thicknesses ranged from 300 to $400\mu m$.

2. Grow first layer of protective thermal oxide at 1100^oC, $0.6\mu m$ thick.

3. Pattern align marks on both sides, using OCG825 standard thin photoresist. Etch in 7:1 Buffered Oxide Etch (BOE).

4. Etch align marks in Silicon using reactive ion etching (RIE)..

5. Grow second layer of protective thermal oxide at 1100^oC, to a total thickness of $1.7\mu m$.

6. Pattern oxide using BOE, to define the nested mask

7. Recoat with photoresist, using Clariant AZ4620 thick photoresist. A thickness of approximately $10\mu m$ after baking is desired. Define the first Deep Reactive Ion Etching (DRIE) etch mask. Mount the wafer on a handle substrate using AZ4620 photoresist.

8. Perform the first deep etch using an STS ICP DRIE tool to approximately $20\mu m$ away from the buried oxide. Dismount wafer in acetone and strip photoresist using a process consisting of burning the organic materials in an oxygen plasma ("ashing") and performing a chemical cleaning step, using a mixture of 3 parts H_2SO_4 added to 1 part of H_2O_2 ("Piranha cleaning").

9. Remount wafer on handle substrate and perform the final etch.

10. Dismount in acetone, and clean using again ashing and piranha. Just prior to fusion bonding, the oxide would be stripped with BOE and an RCA cleaning step would be performed.

The procedure described above will allow the fabrication of a basic tethered silicon membrane structure. It has been found that some amount of exposed silicon outside of the etched membrane features, as provided by the nested mask process, tends to simplify the fillet radius control procedure somewhat.

Additional features, e.g. flow channels, can be defined in the nested mask and the nested mask etch depth can be tailored (within the bounds of the wafer's structure) to suit the requirements of the features needed. In this work it has been found that features deeper than approximately $20\mu m$ (and of in-plane dimensions greater than $\sim 500\mu m$) will not be well suited to an additional lithography step involving the spin-casting of photoresist and subsequent exposure. Another observation is that the nested mask, a hard SiO_2 mask, will generally provide a smoother sidewall than the initial photoresist mask. This can be attributed to a phenomenon sometimes referred to as "micromasking"', where photoresist is removed from the top of the substrate by the DRIE process, and subsequently redeposited on the trench walls, leading to sidewall roughness.

Figure 60, shows, again, a cross-sectional view of all the layers of the MHT device. This figure is similar to Figures 4 and 52, and will be used to reference the process flows for the layers. An accompanying 3D sectional view is given in Figure 61, with the flow path for the working fluid shown in red, and the fluid of an hydraulic amplifier shown in yellow.

The process flows for the five silicon layers, Layers 2, 4, 5, 7 and 8, as shown in Figure 60 are now given in Figures 62, 63, 64, 65 and 66. For the mask layouts, the reader is referred to the appendices.

5.2.3 Glass Layers

The Pyrex glass layers were fabricated by ultrasonic machining. The masks for the glass layers (Layers 1, 3, 6 and 9) are also given in the appendices. This fabrication was performed by an outside vendor[5].

For this device, the glass layers had the following thicknesses:

---

[5]Bullen Ultrasonics, 4613 Camden Road Eaton, OH 45320 Phone: (937) 456-7133 Fax: (937) 456-2779, http://www.bullen-ultrasonics.com/

SOI   Si   glass   piezo
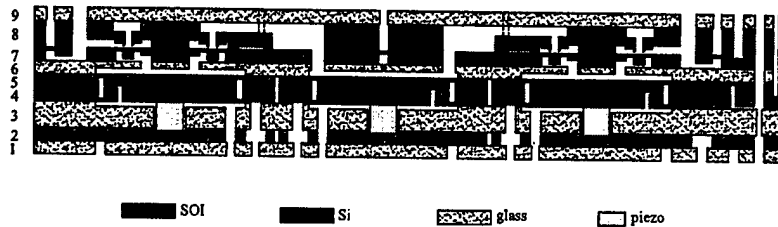
Figure 60: A schematic cross-sectional view of the 10-valve device. This figure is identical to Figures 4 and 52, except for the detail around the valves this figure will be used as a reference for discussion the process flows for fabricating the various layers.
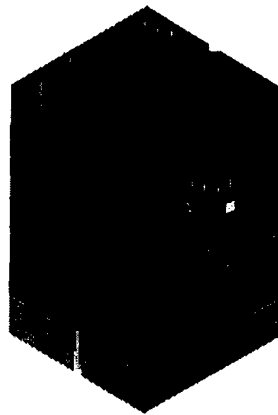
Figure 61: A 3D cross-sectional view of the MHT device with 10 small valves per valve unit. It is a more realistic 3-dimensional representation of the picture shown in Figure 60

1. Start with a 0.8 mm DSP Si wafer with low resistivity

2. Etch global align marks on top side_M2-1, and diasaw lines(not shown) and global align marks on bottom side_M2-2

3. Grow 2 μm thermal oxide

4. BOE both sides to define the holes and recess areas_M2-3 and M2-5 (optional)

5. DRIE bottom side (interface with layer 1) half way into the wafer_M2-5(optional depending on wafer thickness)

6. DRIE top side to finish the holes and isolating trenches_M2-4

7. DRIE top side with nested oxide mask for about 20 μm to form the piezo recesses

8. Bond to layer 1 anodically, die saw cut, and then trim the piezo seating with Plasmaquest

Figure 62: Process flow for Layer 2. This is the layer that provides the lower contact for the piezos.

84

1. Start with an SOI wafer with low resistivity in SOI layer

2. Etch diasaw marks, chip numbers and electrode recesses on SOI_M4-1, and align marks and chip number on handle side_M4-2 by using Etcher1 or STS

3. DRIE through SOI, (BOE buried oxide and some more DRIE into the handle if necessary)_M4-3

4. Grow 2 μm thermal oxide

5. BOE handle for membrane shadow masks and holes_M4-4

6. DRIE handle close to buried oxide for drive membranes_M4-5

7. DRIE handle using the nested oxide mask to finish the drive membranes

8. Strip oxide and the wafer is ready to bond to layer 5

Figure 63: Process flow for Layer 4. This layer forms the lower part of the two-layer drive piston structure. Each device had three such pistons.

1. Start with a 10 μm SOI wafer

2. DRIE handle 1-2 μm for venting channel_M5-1

3. DRIE SOI side for global align marks and through holes(+BOE of buried oxide and DRIE if needed)_M5-2

4. Grow 2 mm thermal oxide

5. BOE handle_M5-3

6. DRIE handle close to buried oxide_M5-4

7. DRIE hadle with nested oxide mask

8. BOE to strip oxide and the wafer is ready to bond to layer 4
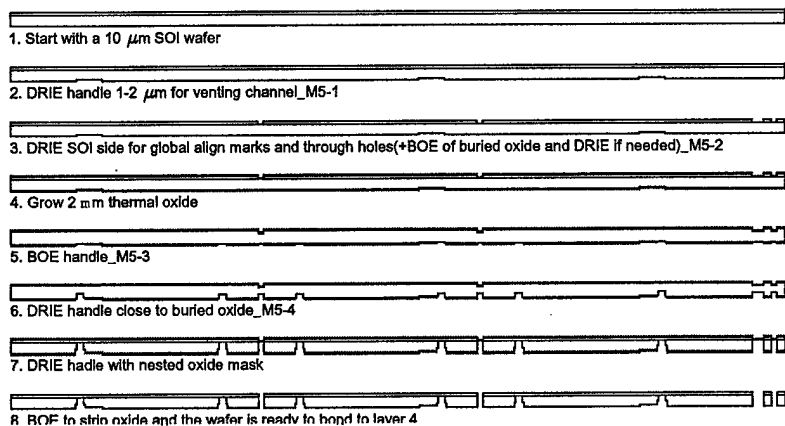
Figure 64: Process flow for Layer 5. This layer forms the upper part of the two-layer drive piston structure and mates to Layer 4.

1. Start with an 8 μm SOI wafer

2. DRIE handle for 10 μm to define the valve lower clearance_M7-1

3. DRIE through SOI side (BOE burried oxide and more DRIE if necessary)_M7-2

4. Grow 2 μm thermal oxide

5. BOE handle_M7-3

6. DRIE handle half way_M7-4

7. DRIE handle with nested oxide mask formed in step 5 to the buried oxide to form the membranes and holes

8. BOE to strip the oxide and the wafer is ready to bond to layer 8

Figure 65: Process flow for Layer 7. This layer contains the valve caps and membranes.

1. Start with a 800 μm thick double side polished Si wafer

2. DRIE bottom side 10 μm for valve seating_ M8-1 and DRIE top side for align marks_M8-2

3. Grow 2 μm thermal oxide

4. BOE top_M8-3 and bottom_M8-4

5. DRIE top side 450 μm_M8-5

6. DRIE bottom side 200 μm_M8-6

7. DRIE top side 200 μm with nested oxide mask

8. DRIE bottom side 10 μm with nested oxide mask

9. BOE strip the oxide and the wafer is ready to bond to layer 7

Figure 66: Process flow for Layer 8. This layer contains the flow paths for the various devices. For the valve test components, it provided two independent flow paths, and for the harvester, a flow path passing through the two valves and the harvesting chamber.

- Layer 1: $3mm$

- Layer 3: $970\mu m$, nominal

- Layer 6: $1mm$

- Layer 9: $3mm$

In the case of layer 3, a recess was machined to provide clearance for the motion of the piston. In the case of Layer 6, a similar recess was machined, but in this case it was used to form the hydraulic amplification chamber. The fabrication of the Pyrex layers was a robust process, and few problems were encountered. For all Pyrex layers, prior to sending the wafers for the ultrasonic machining, align marks were patterned on the glass using BOE and a thin resist (OCG825 resist). The ultrasonic machining was then performed, aligned to these alignment features.

5.2.4 Conclusions

This section presented the fabrication techniques used to produce the silicon and glass wafers for the MHT devices. The fabrication of multiple full wafersets of MHT devices was completed successfully to enable the fabrication of the devices discussed in later sections of this report. In terms of fabrication, this project had the following major achievements:

- Fabrication techniques for the fabrication of high-strength silicon-tethered membrane structures as moving parts.

- Multiple nested mask processes to form complex deep reactive ion etched structures. (See e.g. Figure 66)

By using a combination of silicon and glass layers, and by exploiting the benefits of both aligned wafer bonding and die-level bonding, it was possible, for these experimental devices, to avoid having to bond a full stack of wafers and thereby significantly reduce the risk in the fabrication process. For large-scale production, the assembly procedures could be refined to yield a full process flow on the wafer scale.

5.3 Contributions: Fabrication and Assembly

To summarize, the following was contributed in terms of fabrication and assembly of the MHT device:

1. Fabrication of fragile tethered membrane structures.

2. The fabrication of a nine-layer MEMS device.

3. Die level alignment and anodic bonding techniques.

4. Integration of bulk piezoelectric material in a microscale device.

6 Key Technology Demonstrations Through Device Sub-Component Development

6.1 Development of Testing Rigs and Procedures for Device Characterization

6.1.1 Overview

This section describes a testing system that was constructed to support the testing of the energy harvesting device and its subcomponents. This test system allowed for the filling of devices with the working fluid, silicone oil, as described in Section 3.2. Furthermore, it allowed for the pressurization of the devices, and also for full measurement of all relevant pressures in the fluid circuit. Displacements were measured with a laser vibrometer.

6.1.2 Test System Requirements

The testing system had the following requirements:

- Enable the bubble free filling of the portion of the devices that would see fluid flow. This was accomplished by a vacuum system and a vapor purging process similar to the process described in Section 3.2.

- Enable the static pressurization of both the parts of the devices that would see fluid flow (valve subcomponents and harvesters) as well as the hydraulic amplification chambers and also the upper part of the hydraulic amplification test units. Nitrogen was used to pressurize vessels containing the working fluid, and a regulator bank controlled the pressure.

- Accurate measurement of the relevant static pressures. Commercial pressure transducers were used.

- Measurement of the motion of both the valve caps and pistons of the devices. A scanning laser vibrometer was utilized for its high frequency capabilities and ease of use.

- Driving of the active valves and energy harvester devices. A combination of a computer data acquisition and signal generation system combined with a bank of amplifiers were used for this purpose.

6.1.3 The device test jigs

The purpose of a test jig is to provide an interface between the microfabricated device, in this case the MHT device, and the macroscale environment with which it has to interact. Figures 67, 68 and 69 show the test jig that was designed. Figures 67and 68 depict the test jig that was used to test the static hydraulic amplifiers, and Figure 69 shows the electrical clamp plate that was used instead of the one shown in Figure 68 (a) to test the active valve and harvester devices. In the design of this test jig the following aspects were considered:

- Provide reliable sealing of all fluid connections to the device. Accomplished by o-rings.

- Provide sufficient, but not excessive, clamping force. Accomplished by using springs for preload.
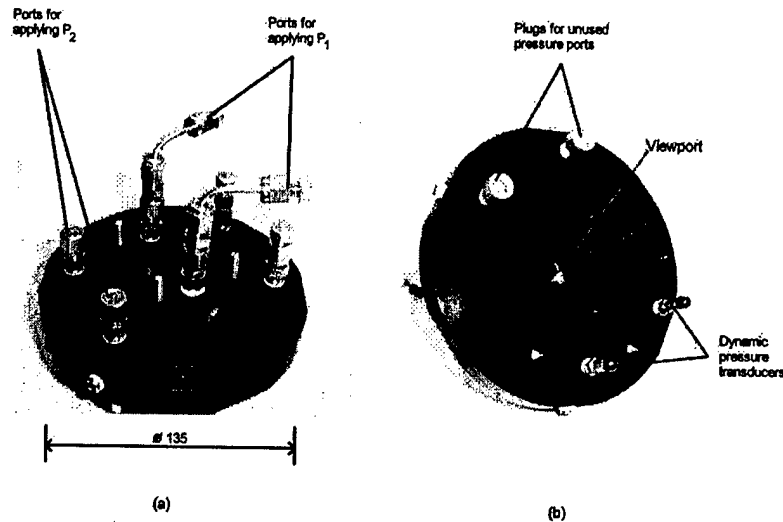
Figure 67: Two views of the test jig: Top view (a) and bottom view (b). Note the viewport for laser displacement measurement.

- Expose as much of the device area as possible for ease of laser displacement measurement. This was done. In addition, the jig was manufactured from aluminum and anodized black, to minimize reflection.

- Ensure proper electrical insulation. The device was insulated from the jig with an acetal-type plastic insert.

- Allow for measuring of dynamic pressure fluctuations near the device. Provision was made for the installation of PCB model 112A22 dynamic pressure transducers on the jig.

- Had to fit in the fluid filling system discussed in Section 3.2.

- Had to provide electrical connection capability for the Active Valve and Energy Harvester devices.

6.1.4 The fluid test system

Figures 70, 71 and 72 shows the entire fluid test rig that was built to test the MHT device and its subcomponents. All tubing was stainless steel. Nitrogen was used to pressurize the Dow Corning DC200 0.65cst silicone oil that was used for all tests where liquid was involved. More information about the fluid test systems can be found in [31].

6.1.5 Displacement measurement

All displacement measurements were performed with a Polytec PI PSV-300 Scanning Laser Vibrometry system, as shown in Figures 70 and 72 Using doppler principles, this system measures the velocity of a moving target. By integration, displacement is obtained. The system was outfitted with a precision displacement measuring board with a rated resolution of $2nm$. Testing has shown that the actual

90
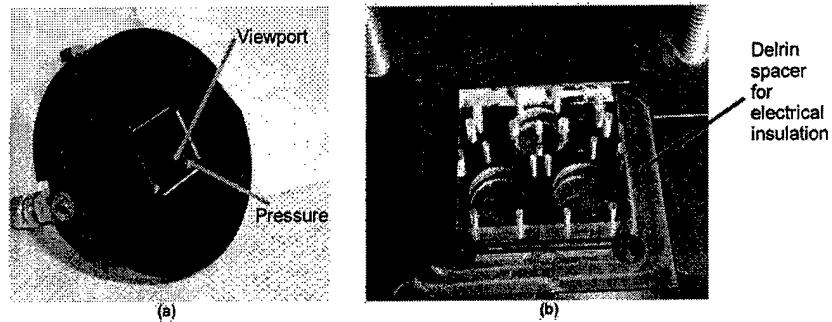
Figure 68: The top clamp (a) shows a recess for the device, two optical viewports and also two fluid pressurization ports. The device is inserted into the main jig (b) and then clamped with the top clamp.
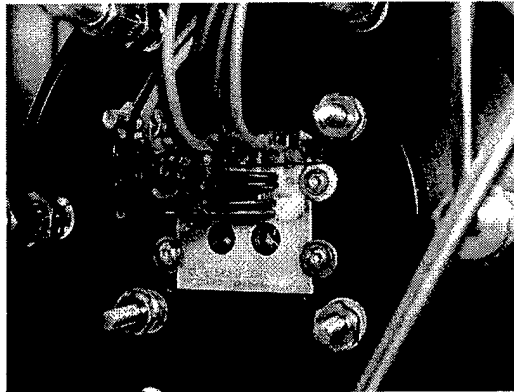
Figure 69: This picture shows the clamp that was used for the devices that required electrical connections. A printed circuit board was used, combined with spring-type contact pins, to make electrical contact. Each contact had two pins for redundancy. Viewports were made in the PC board to accommodate laser displacement measurement of the drive pistons.

Silicone oil tanks.

Vacuum module.

1/2" Tube for vacuum system

Flow measurement and
flow direction control
module

Pressure measurement and
control module.

Connection to device by
flexible lines.

Close-up attachment.

Scanning laser vibrometer.

Device test jig and mount,
held in place by adjustable
clamps.

Figure 70: The fluid test system.

Figure 71: Regulator bank.

Figure 72: Side angle photograph of the test rig, with more detail on the pressure measurement and control module.

resolution is dependent on the amount of ambient noise present, and also on the nature of the surface being measured. The best actual resolution obtained for near-zero frequency displacement measurements was found to be between 10 and $50nm$, depending on the noise present when the measurements were performed.

6.1.6 Data acquisition

All data acquisition was performed using two National Instruments PCI-6110 boards installed in a desktop computer with an Intel Pentium III $700MHz$ processor and 128MB RAM. The data acquisition system allowed the simultaneous, synchronized, measurement of up to eight input channels, at sampling rates of up to $4MHz$. In addition, it also allowed for simultaneous synchronized generation of four arbitrary waveform outputs at frequencies up to $25kHz$, using data acquisition software developed using the National Instruments LabView language.

6.1.7 Basic testing protocols

The various tests performed on the devices all had slightly different protocols, but the following general guidelines were followed in most cases to ensure that the devices are bubble-free and also that they would not be damaged during the startup of a particular test.

- *Filling of the flow circuit and the static pressurization systems:* The test rig was filled with silicone oil prior to inserting the device. This was done by evacuating the tubing system and then filling with silicone oil. The silicone oil itself was also outgassed by drawing a vacuum on the containing vessels.

- *Inserting the device:* During the mounting of the device in the test system care had to be taken not to introduce particles to the device. This was done by flowing silicone oil out of all connecting ports whilst connecting the device. This practice also ensured the minimum amount of entrapped bubbles in the system.
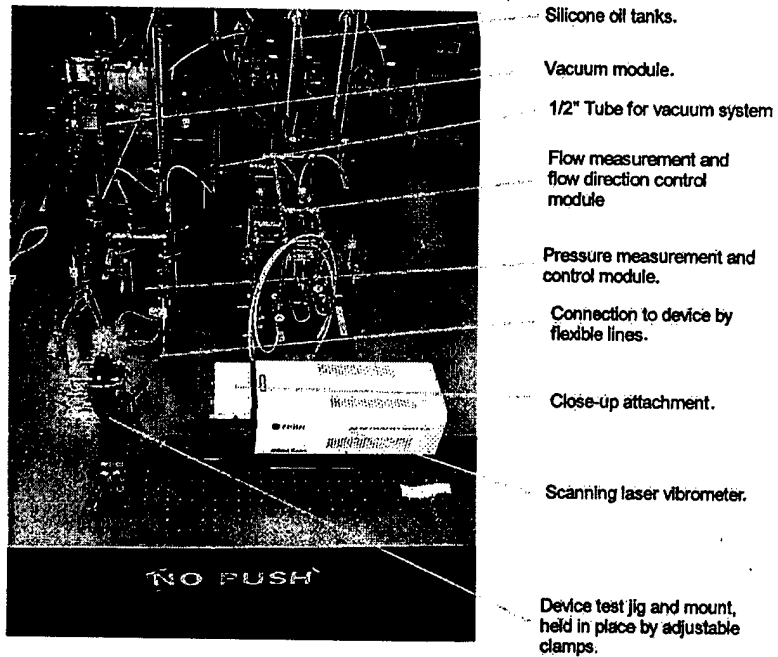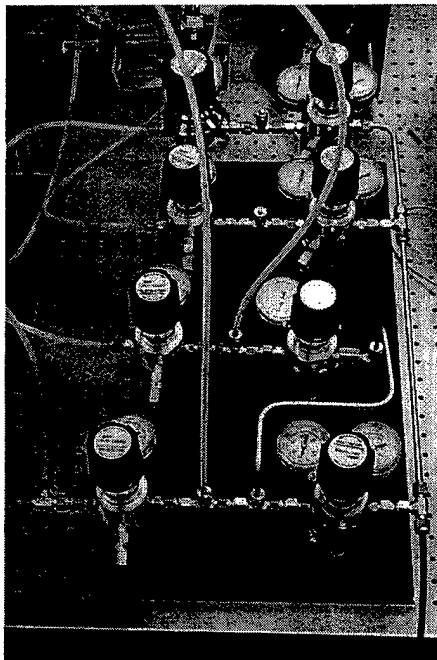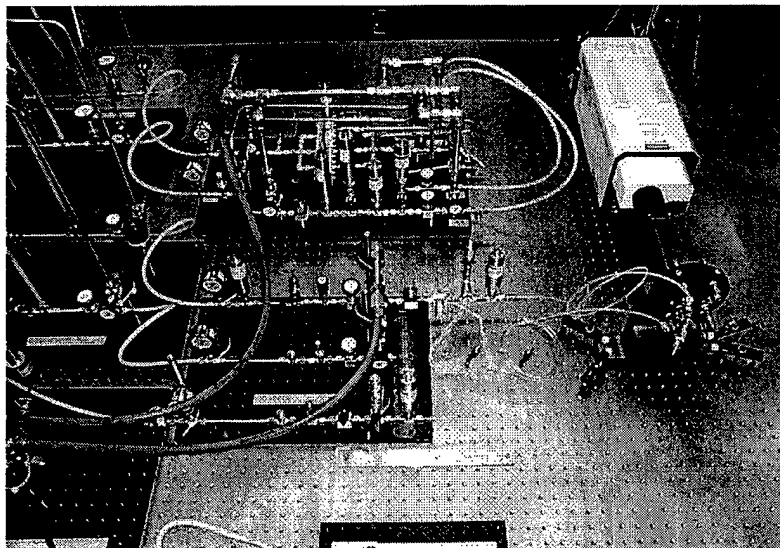
- *Preparing the device for operation:* Before any power could be supplied to the device, all the appropriate pressures had to be set to ensure that the valves were in the correct mean positions. This was done by setting the two P_{HAC}'s as well as P_{HPR} and ΔP to the correct values. These values were then checked by measuring the valve displacement with the laser vibrometer, and also by using the nonlinear membrane code that was developed as part of this project.

- *Testing* After all the pressures were set, the voltages were applied to set the valves in motion. The valve excitation was controlled by the computer data acquisition system, which meant that the valves were sometimes started and stopped abruptly, when a new dataset was being taken. This abrupt starting and stopping did not damage the valves.

6.1.8 Summary

This section described the layout of the test system that was used to test the microfabricated MHT device and its subcomponents. A modular approach was used to design and construct this test system and the same system was used to test all devices. It enabled the bubble-free filling and sealing of the "flow" portion[6] of the devices, as well as a complete measurement of all the relevant pressures and flows.

---

[6]excluding the hydraulic amplifiers, which were filled using the techniques described in Section 3.2.

6.2 Piezoelectric Drive Element Component Testing

6.2.1 Overview

The purpose of this sub-component study was to evaluate the fabrication and assembly process flow of the piezoelectric drive element structure and to obtain quasi-static and high-frequency experimental data on completed devices. Successful integration of polycrystalline PZT-5H material elements, as well as single-crystal PZN-PT material elements, within DRIE etched and bonded tethered piston structures would demonstrate the potential for high-frequency, high-stiffness actuation within the active valve and harvesting chamber portions of the full MHT harvesting device.

In this study, drive element devices were constructed with both single-layer and double-layer pistons, with both PZT-5H and PZN-PT piezoelectric material elements, and with both single and multiple (three) piezoelectric elements beneath the drive element piston. The drive element final design within the active valve and harvesting chamber portions of the full MHT harvesting device incorporates three PZN-PT elements spread out beneath a double-layer piston structure. PZN-PT was chosen due to its enhanced strain capabilities over the polycrystalline PZT materials [32], such as PZT-5H. Three elements were chosen, rather than a single element located at the chamber center, to enhance the stiffness of the actuator by eliminating bending and tilting effects. And a double layer piston structure was decided upon, rather than a single-layer design, to reduce piston compliance and potentially enable piston lightweighting in future design iterations. Within this sub-component study, a device with each of these design variations was built as a means to gradually achieve the final design geometry.

6.2.2 Test-Plan

A double-layer, three piezoelectric element drive element device is illustrated in Figure 73. Within this study, over 10 devices were built and tested. A comprehensive overview of this study is found in [33]. For the purposes of this report, four distinct devices that highlight the important experimental results will be focused on. Schematic cross-sections of these devices are shown in Figure 74(a) and top-view schematics are illustrated in Figure 74(b). The three major design variations contained within this sub-component study were: (1) use of a single-layer silicon drive piston structure versus use of a double-layer piston structure, (2) integration of PZT-5H material versus integration of PZN-PT material, and (3) incorporation of a single piezoelectric element beneath the piston versus integration of three elements spread out beneath the piston.
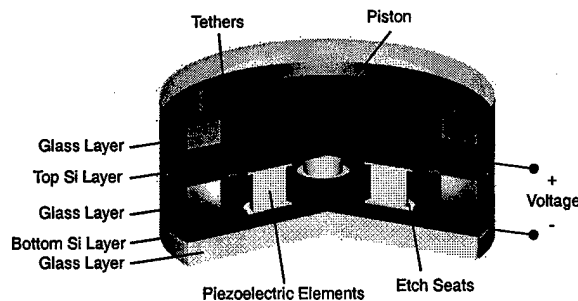

Figure 73: 3-D schematic of a piezoelectric element drive element device. Three piezoelectric cylinders are sandwiched between a lower support silicon layer and an upper double silicon layer tethered-piston structure. Voltage is carried along the upper and lower silicon layers.

Device 1 incorporated a single PZT-5H cylindrical piezoelectric element centrally located beneath the tethered piston. Device 2 incorporated a single PZN-PT cylindrical piezoelectric element also centrally located beneath the piston structure. Device 3 incorporated three PZT-5H cylindrical elements spread out uniformly beneath the piston. In these three devices, the piezoelectric cylinder thicknesses were $\sim 1mm$, while the drive piston had a thickness of $390\mu m$ and the tether had a thickness of $9\mu m$. Device 4 incorporated three square PZN-PT elements beneath a double-layer piston structure. The piston and tether radial dimensions were slightly larger than those in Devices 1-3. In fact, the Device 4 dimensions were exactly those used within the active valve and harvesting chamber components of the full MHT harvesting device. As was the case for Devices 1-3, the piezoelectric element thicknesses were $\sim 1mm$ in Device 4. Since the piston was comprised of two layers, its total thickness was $780\mu m$ with each tether having a thickness of $8\mu m$. A photograph of Device 4 is shown in Figure 75.
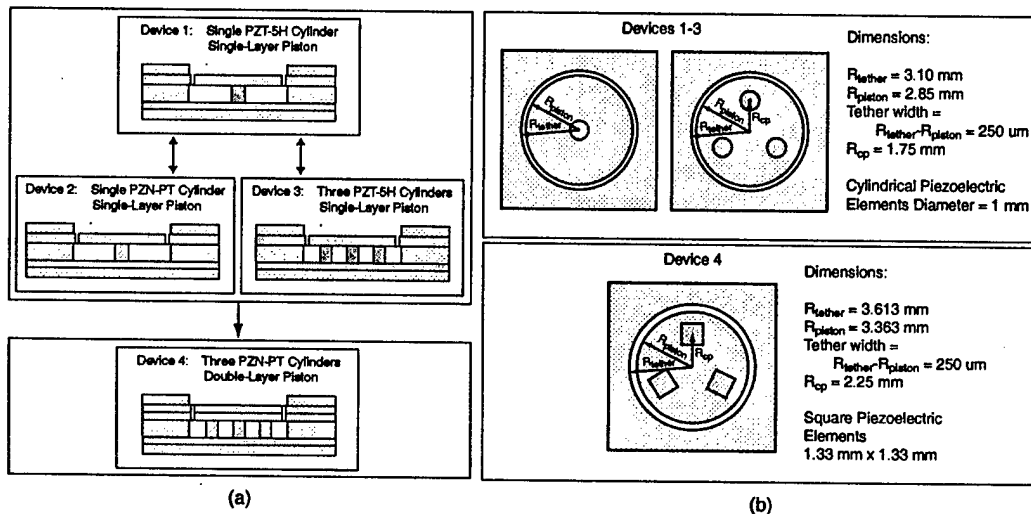
Figure 74: Overview of the drive element sub-component test plan. Devices incorporating single and three piezoelectric cylinders (both PZT-5H and PZN-PT) beneath single-layer and double-layer drive pistons were fabricated and tested.

The process of experimentally testing each drive element device consisted of three major steps. The first step involved careful microscopic inspection of the device to evaluate the fillet radius profile(s) along the etched drive element tether(s). These inspections were performed on the wafer-level prior to any bonding operations. Knowledge of the fillet radius sizes was important for later evaluation of device performance. The second step involved characterization of stand-alone piezoelectric material elements that originated from the same batch (plate) of material that yielded the elements that were integrated within the device. This was a critical procedure so that comparison of drive element device voltage-deflection behavior could be compared to that of representative piezoelectric material elements. The third step involved rigorous experimental testing of the device. Each device was rigidly clamped to a test-jig surface and experimentally evaluated using a scanning laser vibrometer system. Scan points were defined over the top surface of the tethered piston and along the circumferential boundary supporting the piston. Three measurement procedures were used to characterize device performance. In the first procedure, a low-voltage (0V±25V) sweep signal was applied to each device over a frequency range of 10kHz to 200kHz to determine the onset of dynamic modal characteristics. A transfer function of
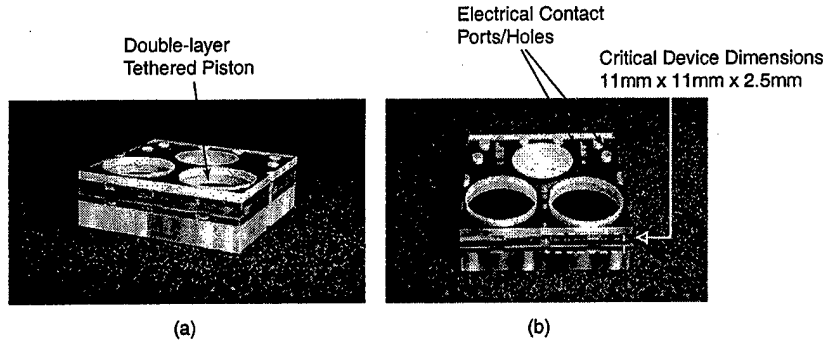
Figure 75: Photograph of an assembled three piezoelectric element, double-layer piston drive element device: thick glass packaging layers were used for clamping purposes during testing.

velocity (averaged over all scan points) versus frequency was recorded. Close-up frequency sweeps around dominant modal frequencies were then carried out to obtain high-resolution mode shape behavior. In the second procedure, a sinusoidal voltage of 500V±500V was applied to each device at selected frequencies of 15kHz and 7kHz to evaluate device behavior below the modal frequencies. At each of these low-frequencies, displacement time histories at the piston center and at an outer edge of the piston were recorded. In the third procedure, voltage-deflection curves (of the piston center) for varying levels of applied voltage were obtained at a frequency of 100Hz to determine the true quasi-static voltage dependent performance of the device.

6.2.3 Summary of Results

A detailed overview of the drive element sub-component study is found in [33]. The fillet radius inspection and the piezoelectric material voltage-deflection characterization steps discussed above, although detailed in [33], are not covered in this report. Rather, a concise overview of the experimental results and the impact of these results on the development of subsequent MHT active valve and harvester devices is provided.

Figure 76(a) plots the transfer function of averaged velocity over the scanned piston surface versus frequency for Device 1. Figure 76(a) presents experimental mode shapes of the device at select modal frequencies. Device 1 experiences a "$1 - \Theta$" tilt mode at $f = 31kHz$, followed by a "plunge" mode at $f = 80kHz$, and a "$2 - \Theta$" mode at $f = 131kHz$. As shown in Figure 76(c), these modal frequencies correlate well with finite-element models of the device. The frequency difference in the "$1 - \Theta$" mode between finite-element model and experiment is most likely attributed to imperfect placement of the piezoelectric cylinder beneath the piston or a non-uniform fillet radius around the tethered-piston. At a driving frequency of 15kHz and an applied voltage of 1000Vpp, the overall peak-peak deflection at the piston center was measured to be $\delta_{p-p} = 0.69\mu m$, slightly lower than the expected range of $\delta_{p-p} = 0.75 - 0.82\mu m$, based on the material characterization tests detailed in [33]. Most likely, this was a result of material property inconsistency within the batch of PZT-5H piezoelectric cylinders.

Dynamic tests on Device 2 resulted in very similar modal behavior to that of Device 1, however, the frequencies at which the modes occurred were shifted downward (see results in [33]). Device 2 experienced a "$1 - \Theta$" tilt mode at $f = 30kHz$, followed by a "plunge" mode at $f = 61kHz$, and a "$2 - \Theta$" mode at $f = 112kHz$. This frequency shift was expected since PZN-PT is a softer material than PZT-5H. At a driving frequency of 15kHz and an applied voltage of 1000Vpp, the overall peak-peak
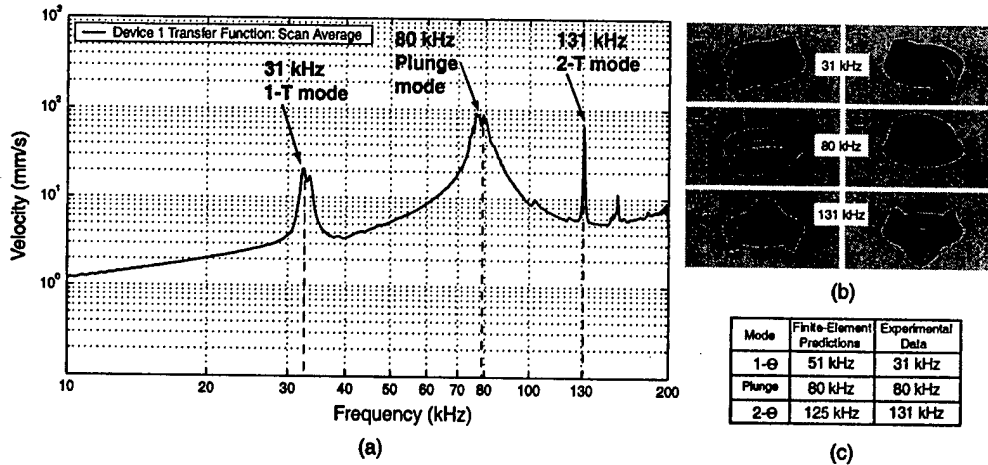
(a)   (b)   (c)

Figure 76: Device 2 dynamic behavior: (a) transfer function of piston velocity versus frequency for a sweep input from 10kHz to 200kHz and small signal drive voltage 0V±25V, (b) vibrometer scan images of mode shapes, and (c) model-experiment correlation for modal behavior. Phase information was not recorded for this device.

deflection at the piston center was measured to be $\delta_{p-p} = 1.42\mu m$, slightly lower than the expected range of $\delta_{p-p} = 1.35 - 1.55\mu m$, based on the material characterization tests detailed in [33]. This enhanced deflection capability is the reason for incorporation of PZN-PT material within the final MHT harvester systems. Devices 1 and 2 both perform well as actuator mechanisms, however, the presence of a tilting mode at a frequency near 30kHz results in the potential for non-ideal rocking behavior when driving with frequencies near 15kHz. It was for this reason that subsequent devices were built and tested with multiple piezoelectric elements spaced out beneath the piston.

Figure 77(a) plots the transfer function of averaged velocity over the scanned piston surface versus frequency for Device 3. In comparing this dynamic response to that of Device 1, modal behavior is not observed until frequencies near $f = 80kHz$. The placement of multiple cylinders beneath the piston eliminated tilting behavior at frequencies in the 30kHz to 80kHz range. As shown in Figure 77(b), initial modal behavior is characterized by non-symmetric motion of the piston surface, most likely due to unsymmetric placement of the piezoelectric elements beneath the piston, differences in material properties among the elements, or a non-uniform fillet radius profile along the tether circumference. A perfectly symmetric finite-element model of this device predicts 1st modal behavior at 225kHz. For low-frequency actuation, the multiple piezoelectric cylinder stiffening effect is justified in Figure 77(c) as the displacement profile at 15kHz experienced minimal tilting during actuation. As for Device 1, the magnitude of the piston center displacement in Device 3, $\delta_{p-p} = 0.72\mu m$, was slightly lower than the expected range of $\delta_{p-p} = 0.75 - 0.82\mu m$. Overall, integration of three PZT-5H elements within a single layer piston device was therefore proven. The next step was to validate incorporation of three PZN-PT elements beneath a double-layer piston structure, as required by the full MHT harvesting systems.

Figure 78(a) plots the transfer function of averaged velocity over the scanned piston surface versus frequency for Device 4. Modal behavior began near 50kHz and was characterized by non-symmetric tilting motion of the piston surface, most likely due to unsymmetric placement of the piezoelectric elements beneath the piston or differences in material properties among the elements. A perfectly symmetric finite-element model of this device predicted 1st modal behavior (piston plunge) at 155kHz
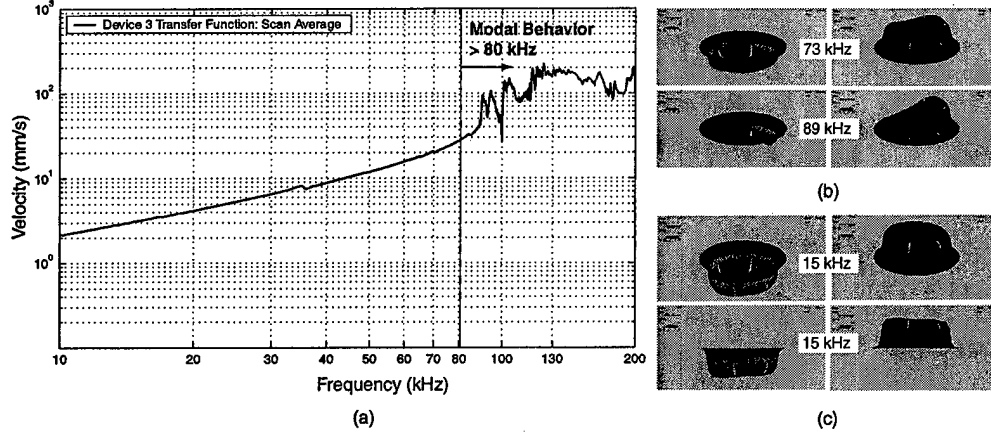
Figure 77: Device 3 dynamic behavior: (a) transfer function of piston velocity versus frequency for a sweep input from 10kHz to 200kHz and small signal drive voltage 0V±25V, (b) vibrometer scan images of mode shapes, and (c) vibrometer scan images of low-frequency motion. Phase information was not recorded for this device.

and 2nd modal behavior (1-Θ piston tilting) at 288kHz. For low-frequency actuation at 15kHz and at a voltage of 1000V peak-peak, the drive element piston experienced minimal tilting (as shown in Figure 78(b)), indicating a well-built and toleranced drive element device.

The degree of piston tilting is illustrated more clearly in Figure 79. The displacement time history at the piston center (Figure 79(a)) is very smooth with no higher order oscillations. Likewise, the displacement time histories at the piston edge locations with maximum peak-peak motions (Figure 79(b)) are also completely free from higher order oscillations. In comparing the peak-peak deflections of these opposite piston edges, the magnitude of tilt is estimated to be ~ 4% of the piston center deflection. The piston center displacement ($\delta_{p-p} = 1.41\mu m$) correlates well with the expected range of $\delta_{p-p} = 1.35 - 1.55\mu m$. As was the case for the first generation drive element devices, the deflection behavior under quasi-static driving conditions is linear with the applied voltage. Figure 80 illustrates this voltage dependent behavior at 100Hz. The deflection response is linear with increasing voltage and the hysteresis contained within the motion is minimal.

6.2.4 Conclusions

The previously described drive element devices were fabricated in an effort to demonstrate that both standard polycrystalline PZT-5H piezoelectric material as well as higher-strain single-crystal PZN-PT piezoelectric material could be incorporated beneath micromachined piston structures. The integration of both single and three piezoelectric elements beneath the drive piston was proven to be reliable. The dynamic low-voltage and quasi-static high-voltage experimental results clearly indicate that the fabrication and assembly process flow for these component structures can enable high frequency actuation capabilities within the active valve and harvesting chamber portions of full MHT harvesting systems.
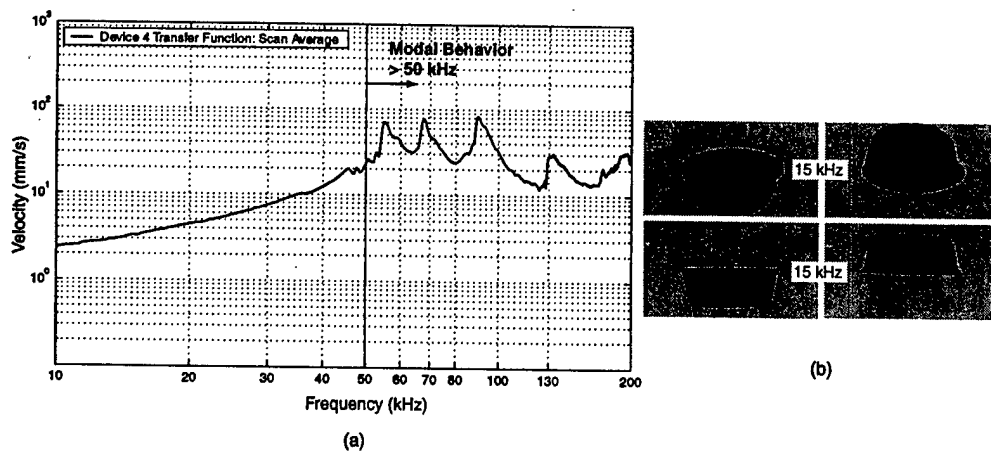
Figure 78: Device 4 dynamic behavior: (a) transfer function of piston velocity versus frequency for a sweep input from 10kHz to 200kHz and small signal drive voltage 0V±25V and (b) quasi-static behavior at 15kHz. Phase information was not recorded for this device.
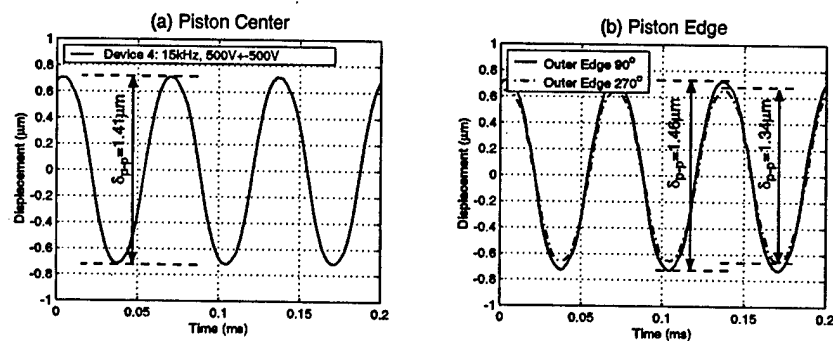
Figure 79: Device 4 displacement time histories for sinusoidal drive voltage of 500V±500V at $f = 15kHz$: (a) piston center displacement and (b) piston edge displacements. These results indicate a rigid well-toleranced device.

100
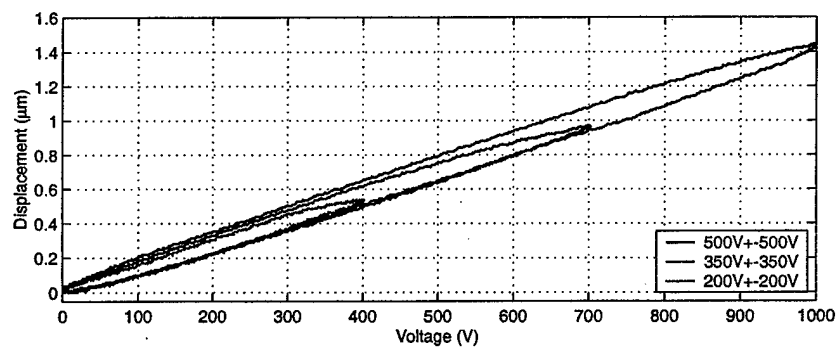
Figure 80: Device 4 piston center displacement versus applied voltage at 100Hz.

6.3 Hydraulic Amplification Component Testing

6.3.1 Objectives

Hydraulic amplification was chosen as the means for stroke amplification of the piezoelectric elements that actuate the valves of the MHT. This means of stroke amplification is both compact and stiff, provided that the hydraulic coupler that couples the small and large pistons can be made sufficiently stiff. This requires that the hydraulic amplifiers of the MHT be:

1. Properly evacuated prior to filling.

2. Filled without introducing any gas bubbles.

3. Sealed in an appropriate and reliable manner.

To this end, a study was performed on the hydraulic amplification units of the MHT device. This work is described in detail in [31], and is briefly summarized here. Using the test system described in Section 6.1, a series of static (pressure-actuated) tests were performed on the hydraulic amplifiers, in addition to dynamic tests that are described in Section 6.4. Tests were performed on two types of devices, namely:

- A device with one large piston of approximately $7mm$ in diameter, and a smaller one of approximately $0.5mm$ in diameter. (HAC Device 3)

- A device with one large piston, approximately $7mm$ in diameter, and ten smaller pistons, each with diameter of approximately $200\mu m$. (HAC Device 4)
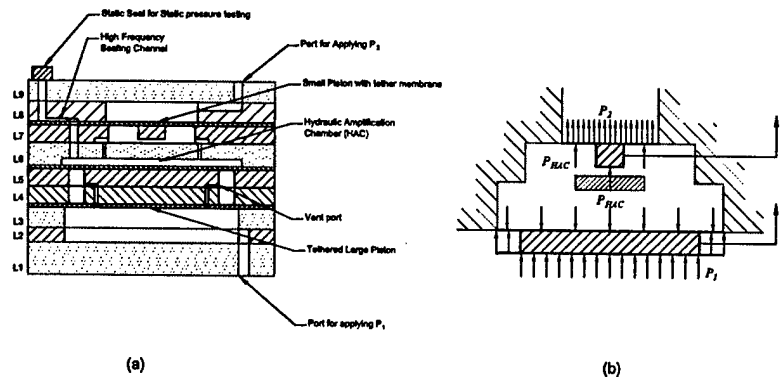
Figure 81: Two representations of the static hydraulic amplification device: (a) A detailed cross section schematic view, and (b) A simplified functional schematic, with nomenclature to be used.

6.3.2 Static hydraulic amplification tests

The static hydraulic amplification tests were performed on geometries schematically depicted in Figure 81. The nomenclature shown will be used for this section.

102

Figure 82: Motion of the large piston for varying pressure on the large piston (P_1) and various values of pressure on the small piston. HAC Device 3.

Tests performed, and correlation with nonlinear models: HAC Device 3   Figures 82 and 83 show the deflections of the large piston and one of the small pistons for P_1 varying from 0 to $500kPa$ and for P_2 having values 0, 92, 298 and $500kPa$. The large piston acts as a pressure transfer element with very little pressure differential across this piston for the deflections seen in these tests. The small piston in turn responds to the pressure transferred by the large piston.

Amplification ratio and amplification sensitivity: HAC Device 3   A suitable figure of merit in evaluating the performance of an hydraulic amplifier would be an amplification ratio or an amplification factor. This ratio can be computed using two different methods. The first method, which we will define as the amplification ratio, is defined as:

$$AR = \left(\frac{z_2(P_1) - z_2(0)}{z_1(P_1) - z_1(0)} \right)_{P_2 = const} \tag{40}$$

Figure 84 shows this amplification ratio. Note that the amplification ratio is always a maximum near the "linear region" of the operating regime. The second method, shown in Figure 85 uses the incremental displacement amplification which allows us to write an expression for the amplification sensitivity:

$$AS = \left(\frac{\partial z_2}{\partial z_1} \right)_{P_1, P_2 = const} \tag{41}$$

Tests performed, and correlation with nonlinear models: HAC Device 4   Both hydraulic amplifiers in HAC Device 4 were tested. The results of the two devices match closely, and only one set is discussed here. Figures 86 and 87 show the deflections of the large piston and the small piston for P_1 varying from 0 to $200kPa$ and for P_2 having values 0, 53, 105, 153, 206 and $253kPa$. As was the case for HAC Device 3, the large piston deflects significantly more than model predictions, indicating a reduced stiffness of the HAC.

103
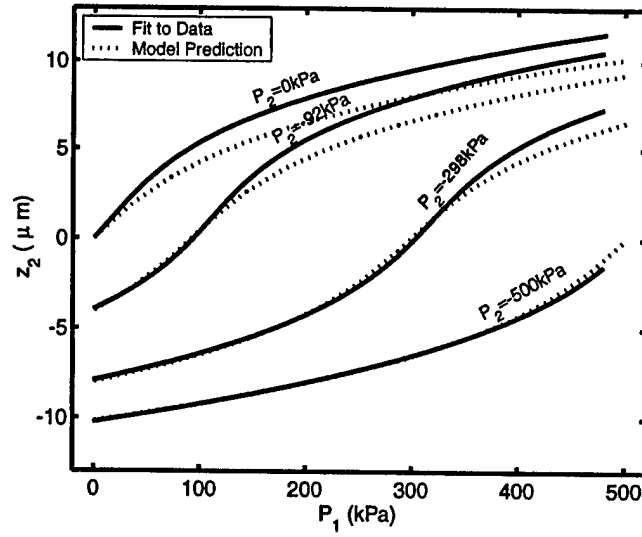
Figure 83: Motion of the small piston for varying pressure on the large piston (P_1) and various values of pressure on the small piston. HAC Device 3.

Figure 84: Amplification ratios for the tests performed. HAC Device 3.
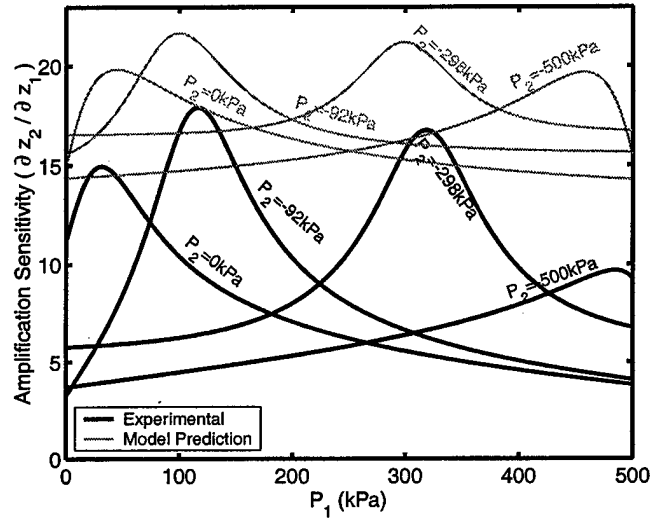
Figure 85: Amplification sensitivities for the tests performed. HAC Device 3.
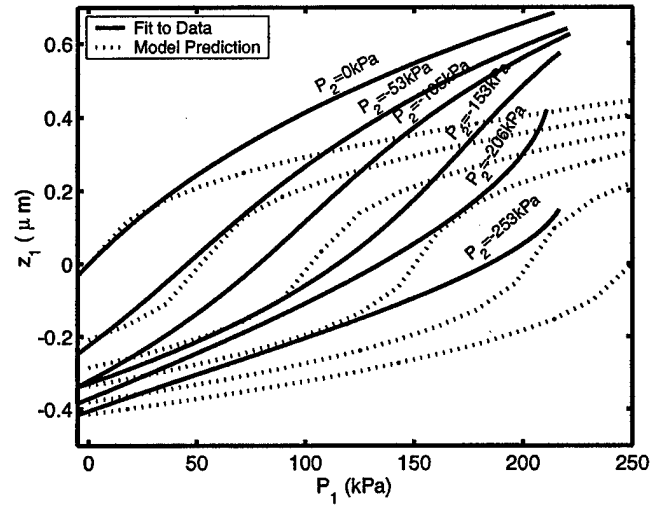
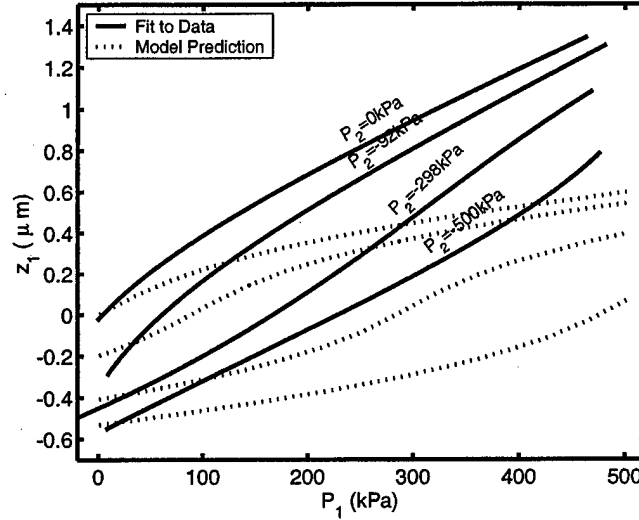Figure 86: Motion of the large piston for varying pressure on the large piston (P_1) and various values of pressure on the small piston. HAC Device 4.
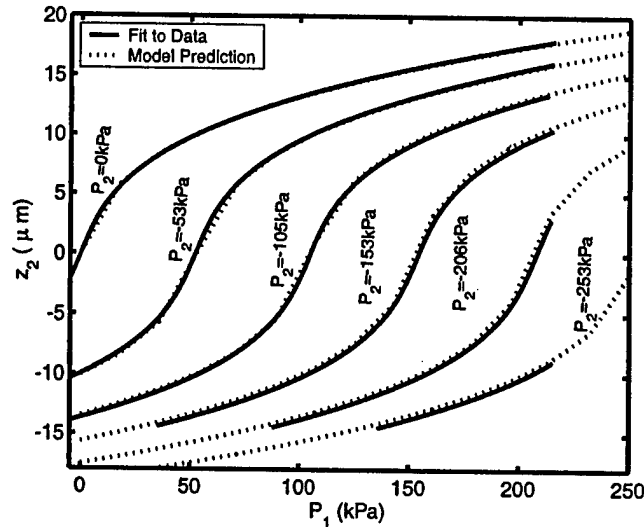
Figure 87: Motion of the small piston for varying pressure on the large piston (P_1) and various values of pressure on the small piston. HAC Device 4. The good correlation is attributed to the fact that the large piston sees a very small ΔP.

Amplification ratio and amplification sensitivity: HAC Device 4 Using Equations 40 and 41, we proceed to compute the amplification ratio and amplification sensitivity for HAC Device 4. The results are shown in Figures 88 and 89. The amplification ratio is higher than predicted for $P_2 = 0kPa$. This could probably attributed to a measurement irregularity. Also, in this case, the amplification sensitivity is higher for the experimental case. This is due to a smaller incremental change in z_1 for the measured values.

In summary, two static hydraulic amplifiers with different theoretical amplification ratios have been tested. The same trends have been seen in the tests of both HAC Device 3 and HAC Device 4, with the latter device, HAC Device 4, appearing to be the one that was better filled and sealed. Amplification ratios of up to 40:1 were observed, when ignoring the $P_2 = 0kPa$ result for HAC Device 4. In addition, amplification sensitivities of approximately 80:1 were obtained.

6.3.3 Accomplishments

The hydraulic amplification subcomponent testing yielded the following accomplishments:

- Hydraulic amplification with sufficient stiffness for piezoelectric active valve actuation were demonstrated.

- These devices also displayed acceptable amplification ratios which compared well with theoretical predictions.

- As technology subcomponents hydraulic amplifiers such as these show potential for use in microscale actuation, not limited to the actuation of valves in an MHT device
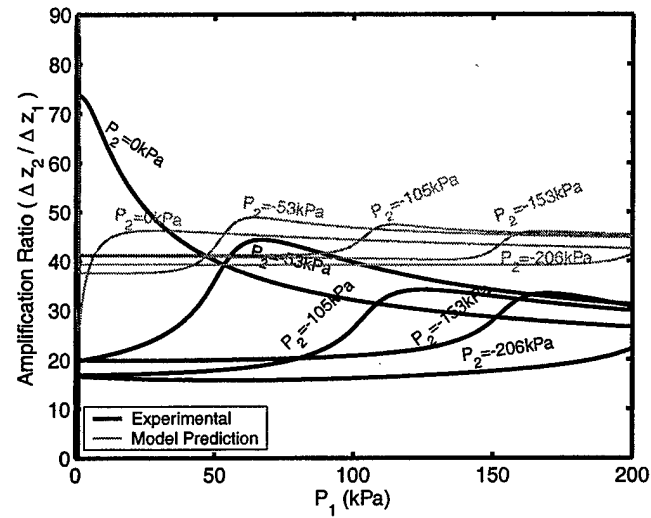
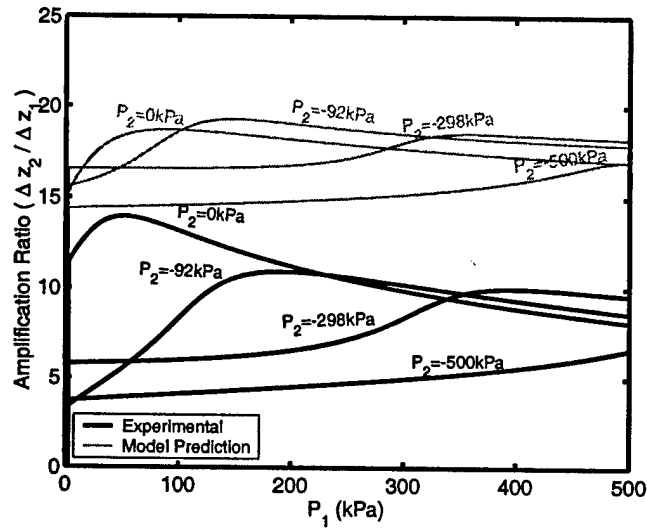Figure 88: Amplification ratios for the tests performed. HAC Device 4.
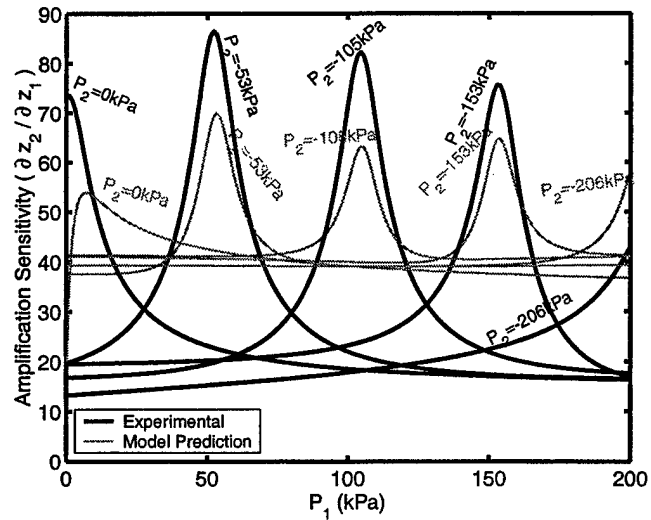
Figure 89: Amplification sensitivities for the tests performed. HAC Device 4.

107

6.4 Piezoelectric Active Valve Component Testing

6.4.1 Overview

The purpose of this component study was to evaluate the quasi-static and dynamic structural performance of the complete active valve device and to determine its limitations in regulating the flow of fluid against imposed differential pressures. Specifically, the four primary objectives of this study were:

1. To understand the dynamic behavior of the active valve device and to determine the range of driving frequency for which the valve behaves in a quasi-static manner.

2. To evaluate the amplification ratio of the active valve structure under a variety of voltage levels and internal and external bias pressures for a driving frequency below resonance to ensure quasi-static operation.

3. To characterize the differential pressure-flow rate curves for the valve cap and orifice geometry of the active valve device.

4. To characterize the dynamic capability of the active valve structure in regulating fluid flow against a preset differential pressure across the valve at a driving frequency below resonance to ensure quasi-static operation.

Successful operation of the valve structure in this manner proves its capabilities as a flow regulation device. A further goal is to identify the limiting differential pressures against which the active valve can function.

The dimensions of the fabricated final active valve device are illustrated in Figure 90. The device incorporated three PZN-PT piezoelectric square elements (each with cross-sectional area 1.06mm x 1.06mm) beneath a double-layer tethered piston structure. The top and bottom tethers of the piston were each $250\mu m$ in width and each had a thickness of $8\mu m$. A valve cap and membrane structure was positioned above the hydraulic amplification chamber, with a structural stop (formed by the glass Layer 6 within the HAC chamber) $\sim 16.5\mu m$ below the equilibrium position of the valve cap. Glass Layer 6 contained a series of "HAC through-holes" to carry the fluid from the lower to upper portion of the HAC chamber. The valve cap had a diameter of 500 μm and the valve membrane had an outer diameter of 1400 μm and thickness of 6 μm. A valve orifice was located $\sim 16.5\mu m$ above the valve cap equilibrium position. The orifice had an inner diameter of $450\mu m$.

6.4.2 Test-Plan

Testing of the active valve device was divided into two primary efforts. The first effort focused on characterizing the actuation capabilities of the valve structure without the effects of differential pressure and flowing fluid above the structure. In this effort, the dynamic behavior of the active valve device was evaluated and the range of driving frequency for which the valve behaved in a quasi-static manner was determined. Additionally, at the determined maximum quasi-static operational frequency, the structural amplification ratio of the valve device was characterized as a function of applied voltage to the piezoelectric drive element. Once the device was proven to be a successful actuator, the second effort focused on evaluating its flow regulation capabilities and limitations. In this effort, the flow regulation capability of the valve device at the maximum quasi-static operational frequency of the structure was evaluated as a function of increasing differential pressure across the valve orifice. In this manner, the valve performance limitations could be determined as the differential pressure was increased.

108
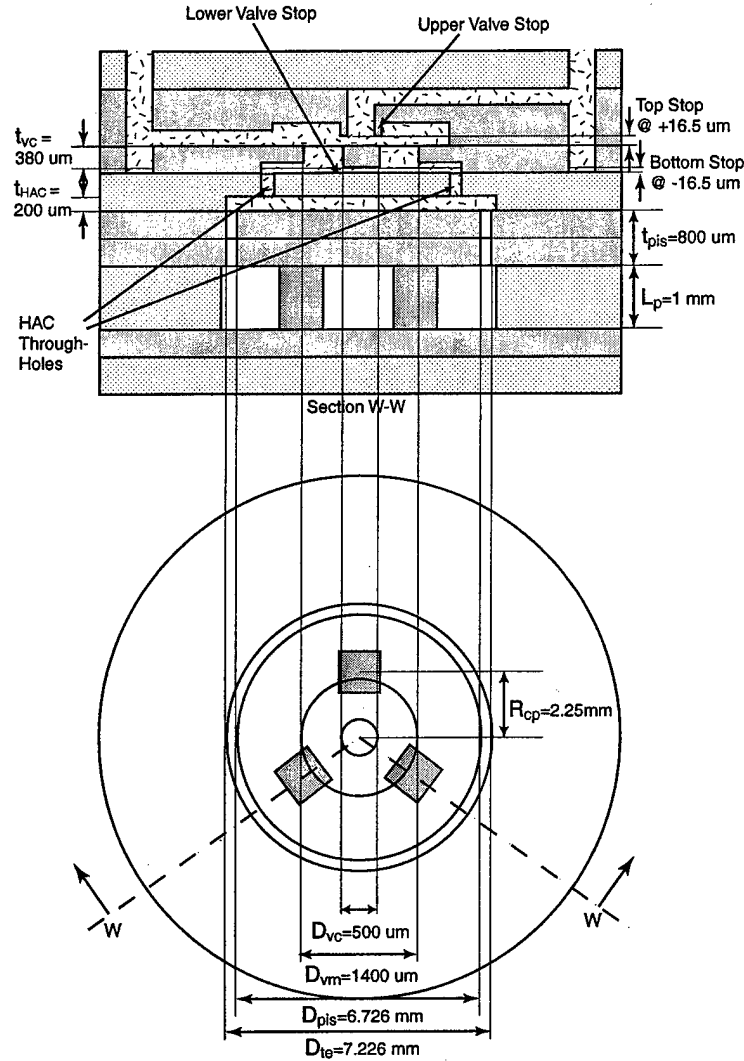
Figure 90: Dimensions of the fabricated active valve devices. Three square PZN-PT elements were incorporated beneath a double-layer tethered piston. A valve cap and membrane structure interacts with the fluid orifice structure at $Z_{vc} = +16.5\mu m$ and with the glass Layer 6 structure within the HAC chamber at $Z_{vc} = -16.5\mu m$.

6.4.3 Summary of Results

Device Actuation Capabilities To characterize the frequency-dependent behavior of the active valve device, a low-voltage $(0V \pm 5V)$ sweep signal from 500Hz to 100kHz was applied to the piezoelectric drive element structure. The corresponding valve cap and piston displacements were measured using the laser vibrometer system. Figure 91 overlays the frequency response of the drive element piston with

that of the valve cap, for the case in which oil is present above the valve structure but for which no differential pressure or flowing fluid occurred across the valve orifice. These tests were performed with $P_{bias} = 500kPa$ to eliminate the possibility of cavitation within the HAC chamber. Additionally, the pressures above the valve cap and membrane were maintained at $P_{IN} = P_{OUT} = 500kPa$.
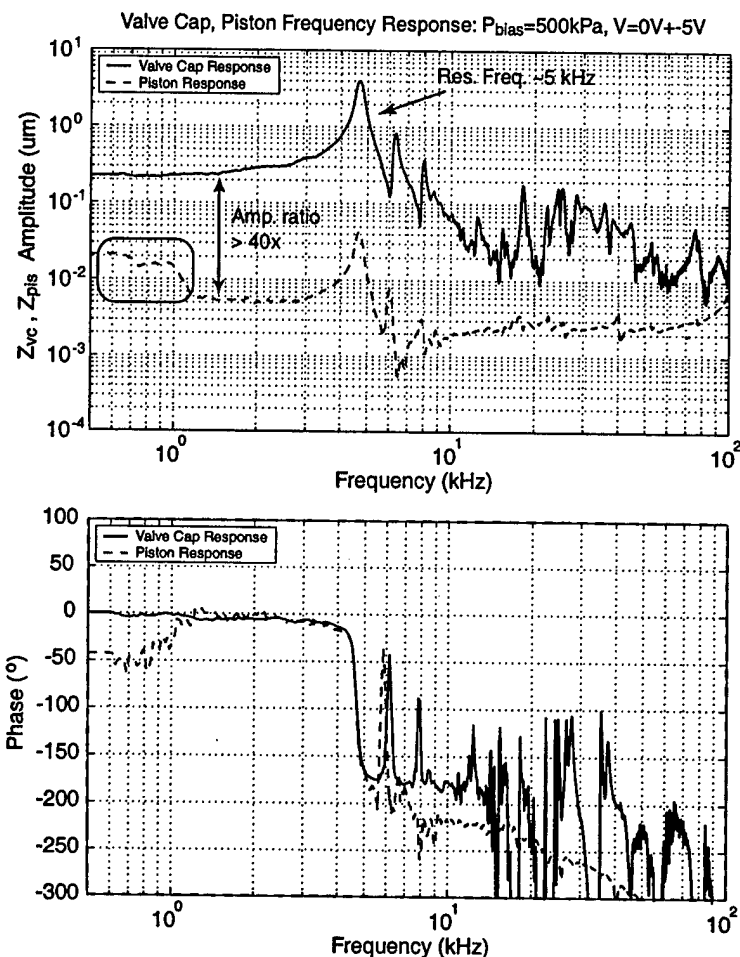
Figure 91: Low-voltage $(0V \pm 5V)$ piston and valve cap frequency responses from 500Hz to 100kHz, with oil present above the valve structure. The top figure plots the valve cap and piston amplitudes, while the bottom figure plots the corresponding phase. The bias pressure in these tests was maintained at $P_{bias} = 500kPa$. An amplification ratio between 40x-50x is observed for frequencies below 5kHz.

The piston and valve responses both followed the same patterns across the frequency range. The valve 1st modal frequency was observed to occur at ~5kHz. The additional peaks in the response were most likely a result of fluid-structure interactions between the oil and the experimental test-jig flow tubes external to the device or between the oil and the flow channels internal to the device. The increase in piston displacement amplitude at frequencies below 1kHz was due to measurement limitations in the

110

vibrometer system (essentially the magnitude of the measured velocities and displacements were of the same order as the noise floor of the system). The results indicate that the amplification ratio of the valve device was steady (between 40x-50x) over the range of frequencies below resonance.

The previous frequency sweep experimental tests found the 1st modal frequency of the device to be ~5kHz. In order to evaluate the quasi-static performance of the structure under the larger drive voltage levels at which the valve was designed to operate, a frequency of operation of 1kHz was chosen. Figure 92 plots the valve cap and piston displacement time histories, respectively, at this drive frequency over a range of applied voltages from 50Vpp to 800Vpp. In Figure 92(a), the dotted lines at $+16.5\mu m$ and $-16.5\mu m$ indicate the position of the upper and lower valve stops, respectively. For an applied voltage of 50Vpp, the response of the valve cap was purely sinusoidal. As the voltage was increased to 800Vpp, the resulting valve cap displacement time history contained small amplitude higher frequency (~5kHz) oscillations due to the non-linear nature of the valve membrane structure. These oscillations became more pronounced as the voltage was increased. In Figure 92(b), the drive element deflection time histories were somewhat rough in nature due to the noise level of the measurement system. As the deflections increased in amplitude, the effect of this noise floor diminished. It is important to note that for a voltage of 800V, the valve was not deflected sufficiently to close against the valve orifice. This was due to the fact that the actual piezoelectric material coefficient was only ~ 75% of the expected value used for the original valve design (see further discussion in next paragraph).

Figure 93 takes these deflection time histories and plots the valve cap peak-peak displacement, piston peak-peak displacement, and corresponding device amplification ratio as a function of applied voltage to the piezoelectric drive element. The amplification ratio was observed to decrease from 50 to 40 as the voltage was increased. This decrease was a result of increased pressurization within the HAC chamber due to the non-linear increase in the valve membrane stiffness. As the voltage was increased, a smaller percentage of the drive element swept volume was transferred to the valve membrane since more volume was lost in the chamber compliances.

Figure 93 also includes model predictions for this behavior. Shown on this plot are three curves generated from the active valve simulation tools discussed previously. The first curve is the predicted response based on the assumed piezoelectric material coefficient value of $d_{33} = 2000pC/N$ used in the original design of the active valve device. The second two model curves are based on limiting values of $d_{33} = 1300 - 1500pC/N$ determined by measuring a large number of individual piezoelectric elements and observing the range of piezoelectric coefficients. Active valve performance was therefore compared to these limiting model cases rather than the ideal case since the piezoelectric elements were determined to be inferior to original design assumptions. The model correlation indicates that the experimental valve cap deflection curve falls slightly short (at 800Vpp for example, the cap deflection was $26\mu m$P-P versus the predicted $31\mu m$P-P) of the prediction limits for $d_{33} = 1300 - 1500pC/N$, while the experimental piston deflection curve falls within these limits for large enough applied voltage. Based on these results, it can be concluded that an additional compliance mechanism must exist within the HAC chamber, most likely due to a smaller than expected value of fluid bulk modulus. A fluid bulk modulus of $K_f = 2GPa$ was assumed in the active valve models and simulations [33]. The corresponding device amplification ratio, as shown in Figure 93(c) decreased slightly from ~50x for a low voltage of 100Vpp to ~40x for a high voltage of 800Vpp, consistently within 5-10% of the limiting model predictions.

Table 5 summarizes the critical actuation capabilities of the active valve device in comparison to model predictions. As discussed previously, the valve 1st modal frequency occurred at ~5kHz. Finite-element models of this valve structure had predicted a 1st modal frequency of 14kHz, however, these models did not include the presence of oil above the valve cap and membrane structure. It was this added mass of the oil that reduced the 1st modal frequency of the valve structure. Future modeling of the valve should more carefully include this added mass effect when predicting modal behavior. As for quasi-static operation at 1kHz, as already discussed, the measured device valve cap deflection fell
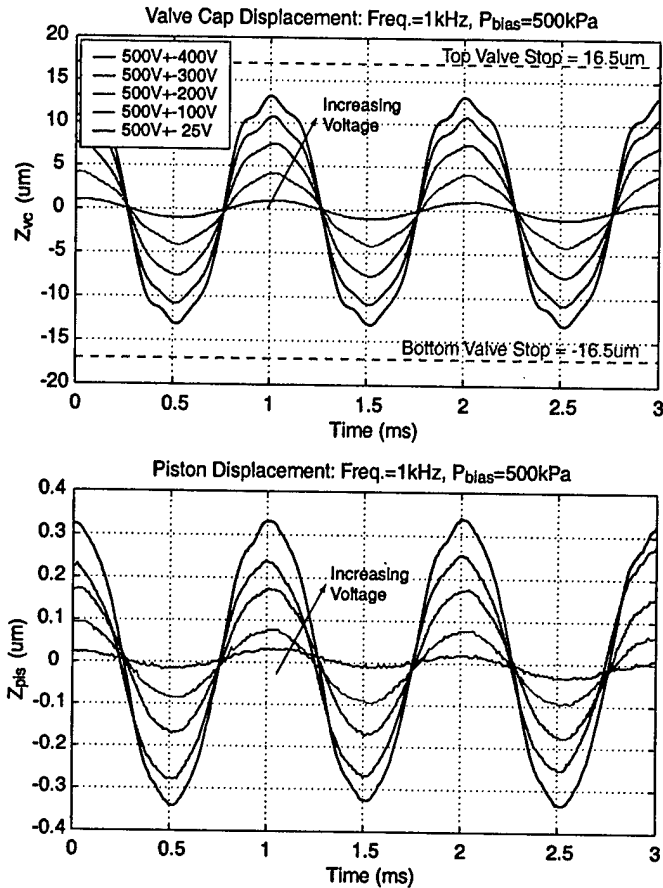
Figure 92: Valve cap and piston deflection time histories for a series of 1kHz sinusoidal drive voltage levels. As the voltage was increased, small amplitude 5kHz oscillations appeared in the deflection responses. Note that a voltage of 800Vpp was not sufficient to close valve cap against the valve orifice.

slightly short of predictions. However, the amplification ratio was in excellent agreement with model predictions. Overall, this encouraging device performance enabled further investigations into the valve's flow regulation capabilities.

Device Flow Regulation Capabilities To evaluate the capability of the active valve device to regulate flow at 1kHz, a series of tests was carried out for increasing imposed differential pressure across the valve orifice. Flow regulation tests were performed for differential pressures $P_{IN} - P_{OUT} = 24$kPa, 95kPa, 145kPa, 200kPa, 260kPa, and 340kPa. By controlling P_{HAC} with respect to the magnitude of P_{IN} and P_{OUT} (using the high-frequency channel and corresponding bias pressure regulator set-up discussed previously), the valve cap was displaced statically upward to a deflection of $Z_{vc} = 11\mu m$. A sinusoidal voltage of 500Vpp was then applied to the piezoelectric drive element at 1kHz to actuate the valve cap

112
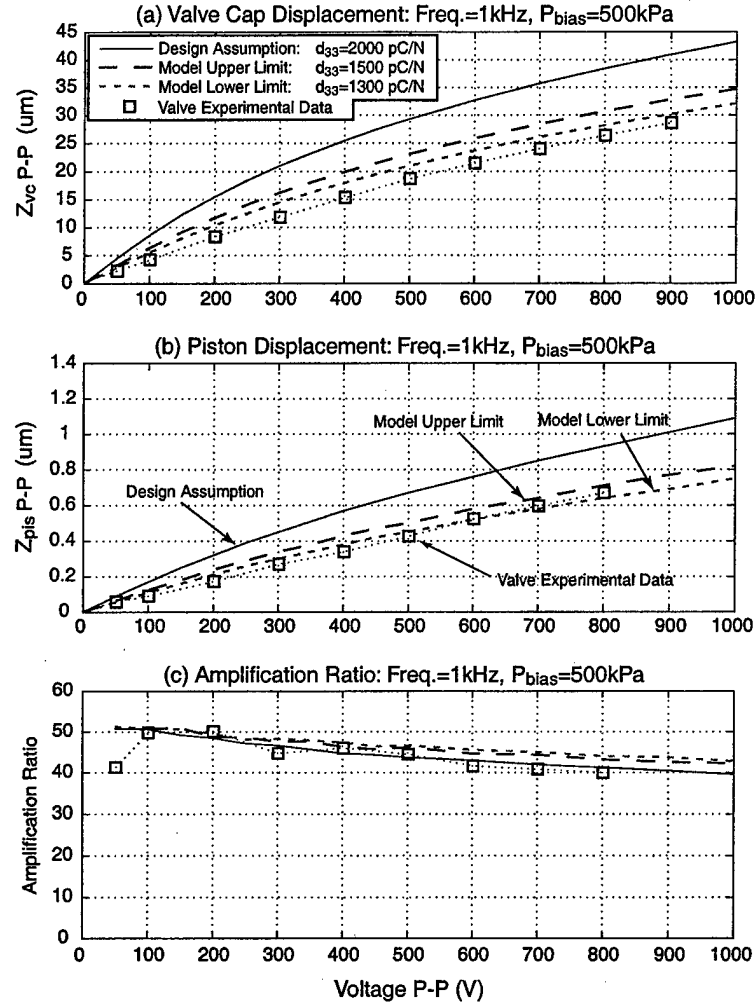
Figure 93: Active valve quasi-static 1kHz model correlation for increasing applied voltage: (a) the valve cap deflection curve was $5 - 10\%$ below the limiting bounds for $d_{33} = 1300 - 1500 pC/N$, (b) the piston deflection curve fell within the limiting bounds for large voltage, and (c) the device amplification ratio (between 40x and 50x) agreed very closely with the predicted limiting bounds.

upward against the valve orifice and downward toward the original equilibrium position of the valve cap. In all test runs, it was desired to just barely close the valve cap against the orifice at its maximum displacement, and to maintain $Z_{vc} = 0$ at its minimum displacement. In others words, it was desired to always ensure a valve opening stroke of $16.5 \mu m$.

Figure 94 plots the experimentally measured flow rates for each of the differential pressure test cases. An applied voltage of 500Vpp was held constant for all of the test cases, and the corresponding measured stroke of the valve cap during actuation is printed inside of each data bar. Figure 94 also

Performance Characteristics	Experimental Results	Model Predictions
1st Modal Frequency	5 kHz	14 kHz
Piston Deflection (@1kHz, 800Vpp)	$0.65\mu m$ pp	$0.72\mu m$ pp
Valve Cap Deflection (@1kHz, 800Vpp)	$26\mu m$ pp	$31\mu m$ pp
Amplification Ratio (@1kHz, 800Vpp)	40x	43x

Table 5: Active Valve Actuation Capabilities
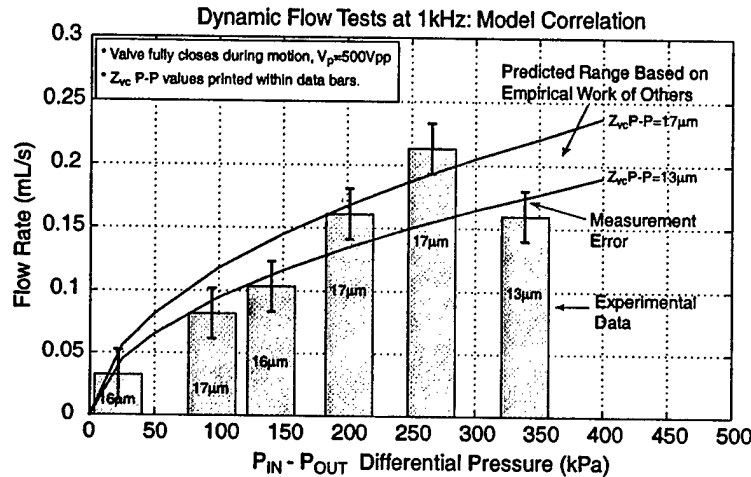
Figure 94: Dynamic flow regulation model correlation at 1kHz for varying differential pressures. Correlation is good over range of differential pressures. Error bars on the data indicate the measurement error, which was estimated based on the flow sensor calibration error and the accuracy of the applied differential pressure.

plots the experimental results versus the model expectations obtained using the active valve simulation tools detailed previously. Model predictions for chosen limiting valve strokes of $Z_{vc,PP} = 13\mu m$ and $Z_{vc,PP} = 17\mu m$ are shown. The model correlation indicates that the active valve regulates flow in excellent correlation with the model predictions. Since the flow loss coefficients are based on a compilation of empirical work from other researchers, the line of predicted behavior in Figure 94 is understood to be of only "limited accuracy", in other words, it is not based on exact theory.

Subsequent test runs at differential pressures in excess of $P_{IN} - P_{OUT} = 340kPa$ resulted in unstable oscillatory motion of the valve cap structure, and eventually fracture of the valve membrane. The nature of the flow behavior (based on Reynolds number) was investigated for a variety of valve opening situations in subsequent studies. The results indicated that these self-excited valve cap oscillations were most probably a result of transitional flow (between laminar and turbulence) through the valve orifice structure, a regime which limited the valve operation to relatively low differential pressures of no more than 340kPa. A comprehensive overview of these unstable oscillatory valve cap experiments is detailed

114

in [33]. Future research work should focus on a better understanding of the flow regimes through these microscale orifice structures and on a redesign effort to develop a valve geometry which is less sensitive to the flow behavior passing through the orifice. Additionally, this redesign should include an effort to increase the 1st modal frequency of the device, to potentially enable operation at or above a frequency of 10kHz. With these redesign efforts, a higher frequency, higher flow rate microvalve could be achieved.

6.4.4 Conclusions

The piezoelectrically-driven hydraulic amplification microvalve, for use in full MHT systems, was successfully fabricated and tested. This concept of hydraulically amplifying the limited stroke of a miniature bulk piezoelectric material into a significantly larger motion of a valve cap structure enabled the valve to simultaneously meet a set of high frequency ($\geq$ 1kHz), high pressure($\geq$ 300kPa), and large stroke (20-30μm) requirements not previously satisfied by other microvalves. The active valve structural behavior and flow regulation capabilities were evaluated over a range of applied piezoelectric voltages, actuation frequencies, and differential pressures across the valve. For applied piezoelectric voltages up to 500Vpp at 1kHz, the valve devices demonstrated amplification ratios of drive element deflection to valve cap deflection of 40x-50x. These amplification ratios correlated within $5 - 10\%$ of the model expectations. Flow regulation experiments proved that a maximum average flow rate through the device of 0.21mL/s for a 1kHz sinusoidal drive voltage of 500Vpp, with valve opening of 17μm, against a differential pressure of 260kPa could be obtained. Tests revealed that fluid-structural interactions between the valve cap and membrane components and flow instabilities (due to transition between the laminar and turbulent flow regimes through the valve orifice) limited the valve performance capabilities. These limitations have an effect on the capabilities of full MHT devices.

As a discrete valve, this device compares favorably with other microvalves reported in the literature in terms of flow rate, frequency of operation and maximum pressure. These tests have shown that it is possible to develop a high flow rate high pressure piezoelectric microvalve. A redesign to stiffen the valve and change its dynamics should allow it to operate at its initial design specifications.

6.5 Contributions: Subcomponent Devices

The evaluation of the MHT subcomponents proved to be quite valuable, and the following contributions can be summarized:

1. The drive piston subcomponent as the first MEMS device to use bulk piezoelectric material integrated by means of thin film bonding.

2. An understanding of the drive piston and its use as a fluidic actuator.

3. The first demonstration of hydraulic stroke amplification on the microscale, with amplification ratios as high as 40:1

4. The hydraulically amplified piezoelectric microvalve, capable of high flow rates and high frequencies of operation.

7 Harvesting Device Testing

7.1 Overview and objectives

The previous sections described tests performed aimed at characterizing the subcomponents of the energy harvesting device. With these results in hand, the harvesting device itself could be evaluated. According to Figure 13, and also according to Equation 1, restated here as Equation 42, the power generated by the harvesting chamber piezoelectric element is proportional to the frequency and the square of the stress on the piezo and, therefore, the square of the pressure swing on the piezo.

$$W = \frac{1}{4}(s_{33}^E - s_{33}^D)\sigma^2 V_p f \tag{42}$$

In addition, the pressure swing on the piezo also governs the *optimum battery voltage* at which maximum power will be generated. Therefore, for maximum power from the piezoelectric element, the pressure swing in the chamber had to be maximised and, at this maximum pressure swing, the optimum battery voltage had to be found. These two concepts governed the testing protocol of the energy harvesting device.

The above tests were performed over a range of frequencies from $100 - 1000 Hz$ and a pressure differential ($P_{HPR} - P_{LPR}$) of $0 - 450 kPa$, using the testing system described in Section 6.1

7.2 Experimental test setup used for energy harvester testing

The test setup used to test the energy harvesting device, along with the key measurements, is shown in Figure 95. The test setup had two principal modes of operation:

1. Chamber pressure measuring mode, using a charge amplifier connected to the piezoelectric element. In this case, the chamber piston acted as a pressure sensor to provide the pressure-time history in the chamber by measuring the closed-circuit charge on the piezo.

2. Energy harvesting mode. In this mode, the energy generated by the piezo was measured.

7.3 Standard testing protocol

The following protocol was followed to ensure that, for a given ΔP, the pressure swing in the chamber was such that the piezo saw maximum pressures equal or approximately equal to P_{HPR} and minimum pressures equal or approximately equal to P_{LPR}, and that the battery voltage was optimal. This would ensure that Equation 42 holds.

1. *Determine the valve drive voltages.* The valve drive voltages, for this experimental investigation, were chosen to be as low as possible while still allowing for sufficient valve stroke to provide for a full chamber pressure swing. As described in the next step, it was preferred to have nonsinusoidal valve drive waveforms in order to minimise both the valve voltage and also the valve membrane stress

2. *Determine the desired pressure differential (ΔP).* The pressure differential governs, to a large extent, the "stress levels" in the device. For the experimental investigations, this pressure was chosen for a given set of experiments, and then maintained.
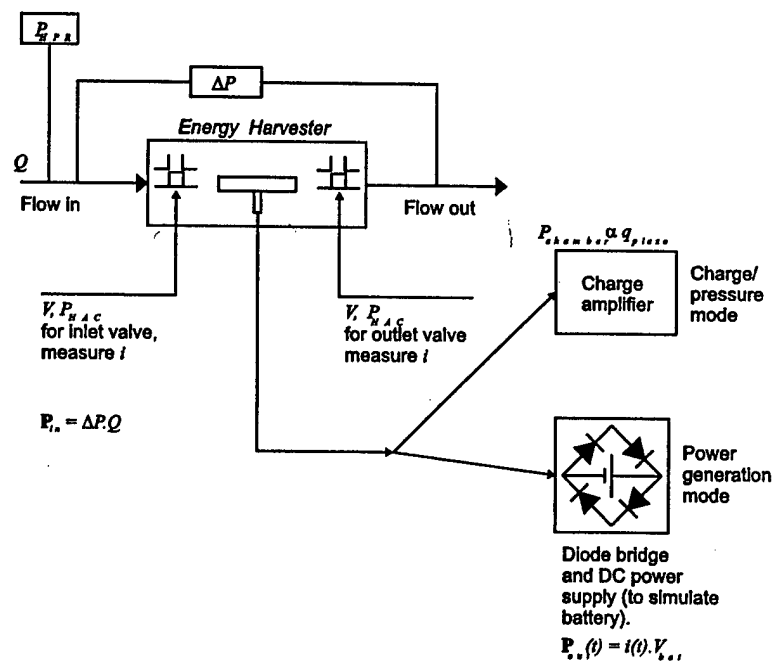
117

Figure 95: Schematic of the energy harvester test setup. The setup had two modes of operation: Charge measurement for chamber pressure validation and power measurement using a diode bridge and a DC power supply to simulate a battery.

3. *Determine the correct valve drive waveforms and valve strokes.* Although the valves were initially designed to be driven by half-sine type waveforms, it was later found to be beneficial, especially at lower pressures of operation, to have a stationary region in the valve motion as is depicted in Figure 96. This would give a "full" pressure swing in the chamber, between P_{HPR} and P_{LPR}. A higher valve drive voltage with a smaller stationary part could also have been used, at the expense of a greater risk of electrical breakdown, and also higher stresses on the valve membranes.

4. *Determine the correct valve steady positions.* The valve steady position is the rest position of the valve. It is given by the steady (or static) pressures acting on it, hence: P_{HAC}, the static pressure in the hydraulic amplification chamber, the pressure on the valve membrane, which is either P_{HPR} or P_{LPR}, and the pressure on the valve, P_{EHC}, the pressure in the energy harvesting chamber. By assuming that $P_{EHC} \approx (P_{HPR} - P_{LPR})/2$, all the pressures on the valve caps were known, and, using the nonlinear valve membrane deflection code described in [33], the position of the valve could be predicted and then set using the various pressures. This estimation method was verified against the direct displacement measurement of the valve using a Polytec PSV-300H scanning laser vibrometer, and was proven to be accurate.

5. *Chamber pressure verification.* Verify that, by using the previous two steps, the device is operating at the proper chamber pressures for a given ΔP.

6. *Determine the optimum battery voltage.* This is done by testing the device, with the now determined drive waveforms and pressures, under "energy generation mode" of operation. The battery voltage that yields the maximum power is then chosen as the operating battery voltage.

7. *Frequency sweep.* For validation, the device is then operated at various frequencies and the linear dependence on frequency is verified.

The above tests were performed over a range of frequencies from $100 - 1000Hz$ and a pressure differential ($P_{HPR} - P_{LPR}$) of $0 - 450kPa$, using the testing system described in Section 6.1

7.3.1   Limitations of the harvester testing

In the tests performed, some limitations of the device were encountered. These are mentioned here.

Additional effects at low ΔP   The procedure described in Section 7.3 works well for moderate and high device pressure differentials. Initially, the device was tested at lower pressure differentials, where the model and experimental result did not agree very well. The reason for this was attributed to the fact that, at these very low pressures, the pressure exerted on the chamber by the outlet valve cap, and also, to a lesser extent, the inlet valve cap, proved to be significant compared to the ΔP of operation. The models did not capture this phenomenon, because at the design conditions of $\Delta P \sim 2MPa$ it can be neglected. This effect is shown in Figure 97.

Difficulties at high ΔP   At very high (but not yet design level) pressure differentials, another limit for device operation was found. This was initially observed in the active valve tests, described in Section 6.4.3. When operated under very high pressure differentials, excessive valve oscillation was observed. In [33], this phenomenon is explained and is attributed to flow induced vibration in the transition flow regime between laminar and turbulent flow. Device operation under these conditions was not possible, and, indeed, this was also the cause of failure of the best performing device. This phenomenon, also not captured by models, placed a fundamental limit on the capabilities of the devices tested here. A suitable redesign to eliminate this suspected mode of vibration should enable the devices to perform
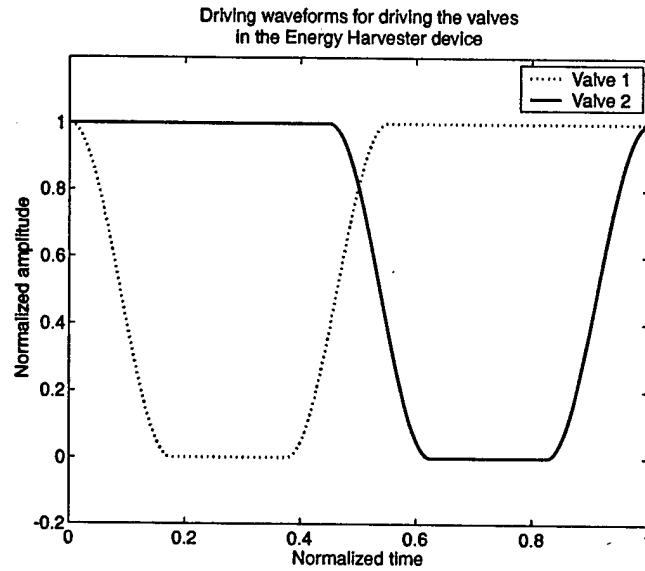
Figure 96: Active valve driving waveforms for the energy harvester. The values are all normalized. Note the flat regions where the valves are kept fully open. The valves can be seen to operate in a "normally closed" state, and they are opened to fill and evacuate the chamber.
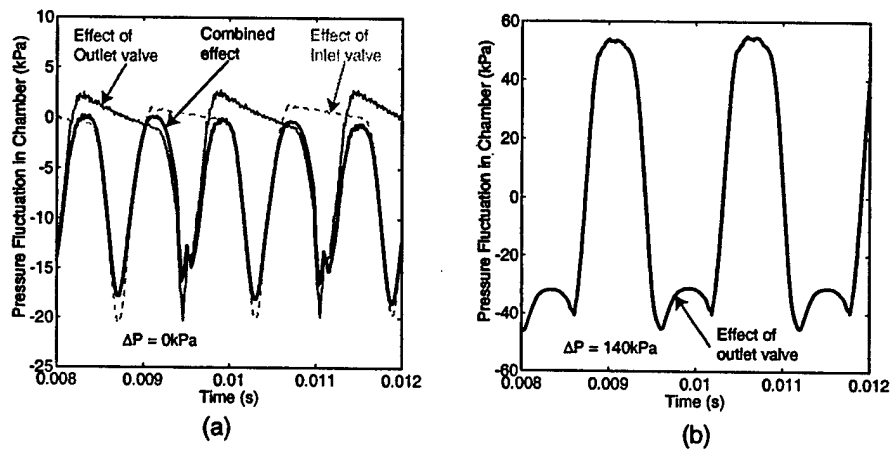
Figure 97: Effect of the valves on the chamber pressure at low[8] ΔP. In a $\Delta P = 0kPa$, and in (b) $\Delta P = 140kPa$. In both cases, the valve driving voltage is $350V_{p-p}$. This effect is only significant at low pressure differentials. At the design values of $\sim 2MPa$ it can be neglected.

120
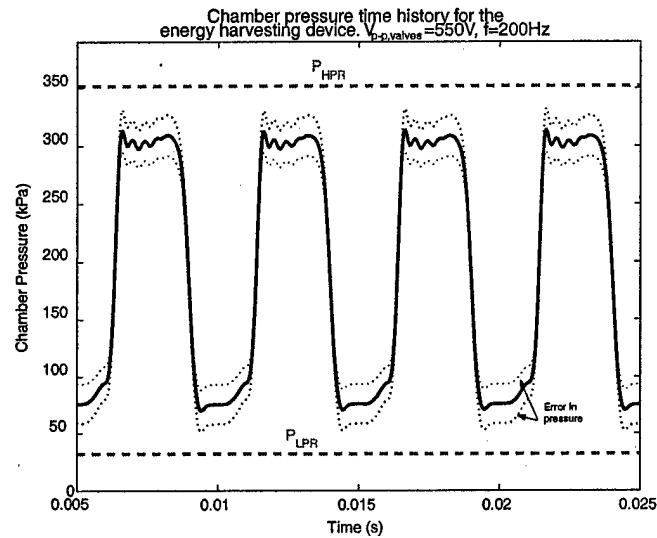
Figure 98: Chamber pressure time history for the harvesting device. Note the flat sections in the time history, indicating a steady pressure in the chamber. The fact that this pressure does not appear to be equal to the actual P_{HPR} and P_{LPR} values can be attributed to measurement errors. ($d_{33} \approx 1500pC/N$) (assumed)

to their initial, quasi-steady design limits. It should be noted that under static loading conditions, the valve membranes saw deflections with associated stresses in the membranes close to the 1GPa design limits of the device. Therefore, if the flow-vibration problem could be eliminated, the devices should be able to perform as designed.

7.4 Chamber pressure time history validation

The first test, before any harvesting testing was done, was to ensure proper filling and evacuation of the chamber. This was done by connecting the harvester chamber piezo to a charge amplifier and measuring the closed circuit charge. This charge was assumed to be proportional to the stress on the piezo. Through geometry, by knowing the diameter of the harvesting piston, the equivalent chamber pressure could be estimated. Figure 98 shows a typical chamber-pressure history for a run that produced a maximum power of $220\mu W$ at $1kHz$ and a ΔP of approximately $320kPa$.

7.5 Energy harvesting results

This section presents results from the tests performed on two energy harvester devices. Both devices had a single inlet and a single outlet valve, identical to the valves that were described in Section 6.4. Therefore, these two energy harvesting devices were tested within the limits set by the capabilities of those active valves. Using the second configuration, with the bridge rectifier and diode circuitry, as described in Figure 95, current-time results such as those shown in Figure 99 were obtained. From the current-time history, the output power was calculated. Note that there is a current spike that follows the inlet and outlet valve motions, when the rate of change of pressure in the chamber is a maximum.
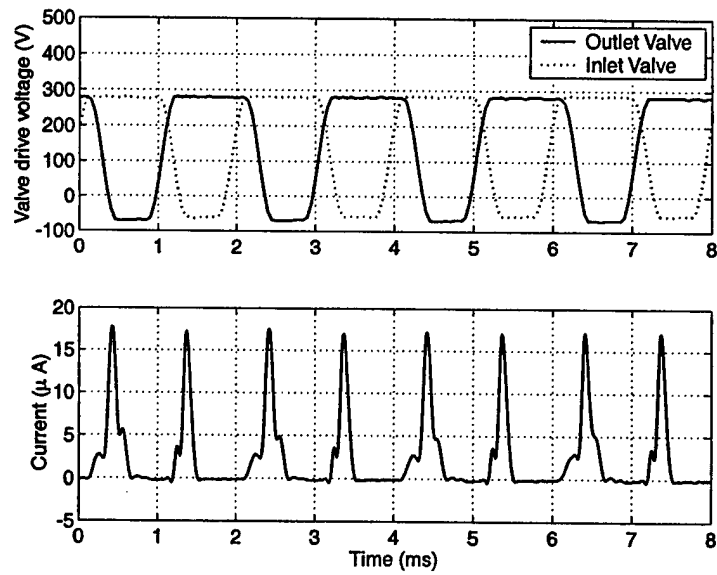
Figure 99: Time history of the valve drive signals and the current from the rectifier bridge. The valve motion is in phase with the valve drive voltages. There is a current spike resulting from the opening and closing motions of the valves when the rate of change of pressure on the piezoelectric element is a maximum.

7.5.1 Power generated

The first results under consideration are those of the harvesting chamber alone. Tests were done at frequencies of $100Hz$, $200Hz$, $500Hz$ and $1kHz$ and various pressure differentials. For each given ΔP, the battery voltage was determined as described earlier. Figures 100 and 101 show power obtained from the piezoelectric harvesting element for various pressures and frequencies. Important points about the experiments and correlation can be summarized as follows:

- An overall electromechanical energy conversion efficiency of 70% was assumed to account for material losses and diode losses. It should be noted that this is not the system efficiency. It is only an indication of how much of the mechanical energy of the piston is converted into electrical energy via the piezoelectric element and the circuitry.

- It should be noted that, even if perfect filling and evacuation is achieved in open circuit case, measuring the chamber pressure as describe in Section 7.3, there is no guarantee that it will be achieved if the circuit is attached, which results in decrease of piezoelectric element stiffness, if averaged over one period. For a stiffer chamber, it is easier to fill and evacuate.

- For each data point the optimum battery voltage was determined by varying the voltage and measuring the generated power. The optimum battery voltage is an indication of the pressure time history in the chamber since it is proportional to the pressure band within the chamber. At 46kPa, the measured optimum battery voltage is very close to the expected value, which means that the chamber pressure fluctuates between the low and high reservoir pressures. However, at larger pressure differentials, the measured optimum battery voltages are less then the expected values, which indicates that the pressure band is less than expected. In other words, the chamber couldn't be filled and evacuated in the required time interval. Since the power heavily depends on the pressure band in the chamber, the generated power is less than predicted by the model, as expected, which can be observed in Figure 100. However the pressure bands suggested by the measured battery voltages at higher pressures(the pressure band can be calculated using the battery voltage) were consistent with the measured power levels. This can be attributed to two factors: either the valves are more resistant than predicted, or the chamber is more compliant than predicted. Tests performed on the valves showed that the pressure flow relationships correlate well with the experimental results. This suggests that the smaller pressure band at high differential pressures is due to the compliance of the chamber.

- The battery voltages measured and obtained powers do not correlate well in the case of the larger pressure differentials which are shown in Figure 101. The source of the inconsistency between the pressure differentials suggested by the measured battery voltages and the generated power can be attributed to the fact that the operation conditions at which these results were taken are beyond the safe operation limit of the active valves and the device suffered from some unwanted oscillations and vibration due to the active valves which introduces additional dynamics to the system.

For obtaining the data in Figures 100 and 101 the following additional operational parameters were used:

- Valve drive voltage: $350V_{p-p}$ for $\Delta P < 150kPa$, $550V_{p-p}$ otherwise.

- Mean deflection of the valves: $\sim 8\mu m(p-p)$

- Motion of the valves: $8 - 12\mu m(p-p)$

- Inlet pressure (P_{HPR}): $\sim \Delta P + 50kPa$
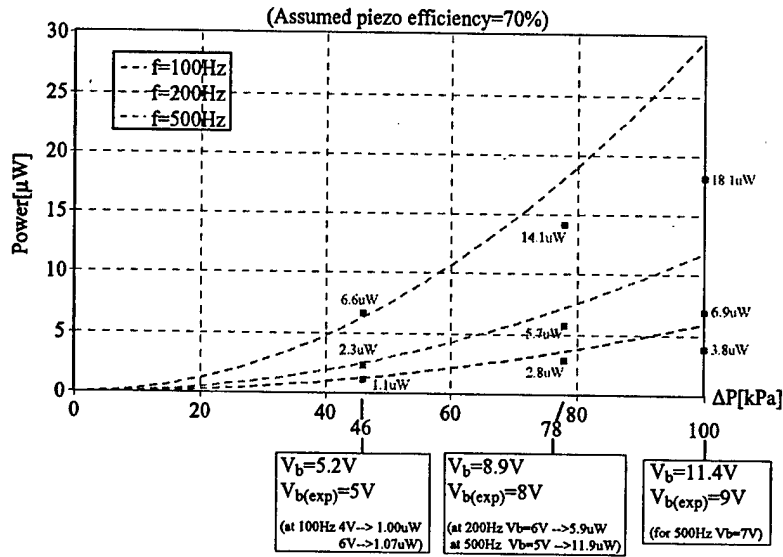
Figure 100: Model-experiment correlation of the harvester at low pressure differentials. These tests show good correlation in terms of battery voltage and power produced.
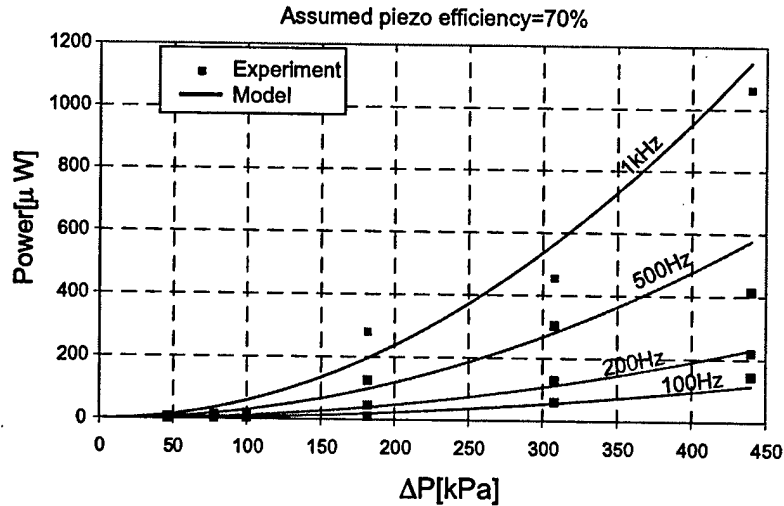

Figure 101: Model-experiment correlation of the harvester at higher pressure differentials. These tests show good correlation in terms or power generated. There are some discrepancies w.r.t the battery voltage.

It was found that obtaining sufficient valve motion for filling and evacuating of the chamber was important. However, excess valve motion did not seem to have an additional significant effect on the device performance. This can be attributed to the fact that, once the harvesting chamber is "filled", any additional valve motion is not necessary. Therefore, the device benefitted most from large valve motion at the higher pressure differentials and higher frequencies.

7.5.2 Power consumed and comparison of power supplied, produced and consumed

It was found that the valves consumed a significant amount of power, on the order of $1 - 10mW$. The valve power consumption was found to be in this range for most of the tests conducted, as shown in Figure 102. Therefore, this energy harvesting device has a negative efficiency, where the efficiency is defined as:

$$\eta = \frac{P_{out,net,elec}}{P_{in,fluid}} = \frac{P_{out,chamber} - P_{in,valves}}{P_{in,fluid}} \tag{43}$$

However, Figure 102 seems to indicate that there exists a fixed minimum power consumption of the valves, and that this consumption does not increase dramatically with increasing fluid power. The power generated, however, does appear to increase. The results seems to indicate that, if the device could be operated with approximately $100mW$ of fluid power, defined as $\Delta P \times Q$, the power produced by the harvesting chamber may equal that required by the valves. Furthermore, recall that good model correlation was obtained with respect to the power harvested from the piezoelectric element, suggesting that, had it been possible to operate the device at its design pressure ($\sim 2MPa$), design frequency of $\sim 10kHz$ and corresponding flow, the design power of approximately $0.5W$ could be attained. To reach this goal, a redesign of the valve would be required to eliminate the offending structural modes that caused premature resonance of the valve at lower flow rates and pressures.

7.6 Conclusions: Harvesting device testing

The following accomplishments and other significant items were realized during testing of the energy harvesting device:

1. Two energy harvesting devices were tested, with a maximum power level of 1mW being obtained from the harvesting chamber at a ΔP of $440kPa$

2. Good correlation was obtained with models for energy harvesting at low pressures. If this trend could be continued at high pressures, and high frequencies, the design power output of the chamber could be attained.

3. It has also been shown that net positive power output should be possible if higher flow rates and pressure differentials could be attained across the device. This would be made possible with a valve redesign that would allow the device to operate at the design pressures.
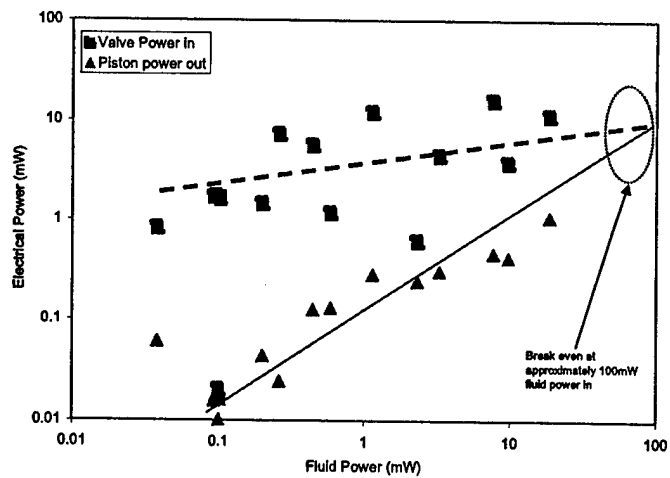
Figure 102: Comparison of electrical power and fluid power. The graph seems to indicate that the power consumption of the valves does not increase at the same rate as the power generated by the harvesting chamber, as the fluid power into the device goes up. The "break-even point" appears to be at approximately 100mW of fluid power in.

8 Conclusions and Recommendations

8.1 Conclusions: An overview

Although a fully integrated heel-strike energy harvesting mechanism was not achieved in this project, several significant advancements were made in the following areas:

1. Systems modeling

2. Flow losses through annular poppet valves

3. Determining piezoelectric material power generation capabilities for commercially available compositions as well as two advanced materials, single crystal PMN-PT and single crystal PZN-PT.

4. Microfabrication techniques for silicon tethered membrane structures.

5. Integration of bulk piezoelectric material on the microscale.

6. Evaluation of the strength of silicon membranes for use as flexural seals, and the requirements placed on the fabrication of these structures.

7. Filling small micromachined dead volumes with liquids and sealing them.

8. Hydraulic amplification was proven on the microscale for the first time.

9. For the first time, an hydraulically amplified high-pressure high-frequency valve was demonstrated on the microscale.

10. Energy harvesting from a pulsing fluid pressure acting on a piezoelectric harvesting element was demonstrated.

11. The final MHT device is a true bi-directional transducer that can operate in both harvesting and pumping modes of operation.

These accomplishments will now be discussed in detail.

8.2 Systems modeling

- A full lumped parameter system modeling scheme was introduced, taking into account all the relevant material properties.

- To this lumped model was attached the results of a nonlinear membrane deflection code in the form of lookup tables to accurately model the valve motions of this device.

- All the devices tested showed good correlation with the models. Effects not captured by existing models - i.e. flow induced vibration of the valves prevented the device to be tested at its ultimate design level.

A redesign should enable the device to be tested at its ultimate design levels, and the existing models are expected to still provide a good approximation at those operating conditions.

8.3 Valve flow loss modeling

- A macroscale test setup was constructed to measure the loss coefficients of annular poppet microvalves. These loss coefficients correlated well with measured values from experiments of the microfabricated valve devices.

8.4 Piezoelectric material capabilities

- The energy generating capabilities of various piezoelectric materials were evaluated and it was proven that significant energy can be extracted from piezoelectric materials at high frequency.

- The energy extraction can further be enhanced through the use of appropriate electronics, as described in Section 2.2.2.

- Detailed nonlinear material models were derived for PZT-5H, PZN-PT and PMN-PT piezoelectric materials.

- Techniques were developed for incorporating small bulk piezoelectric actuation elements into a microfabricated structure with micron-size tolerances. This enabled the fabrication of power-MEMS devices with superior performance compared to similar devices attempting to use thin film piezoelectric materials.

8.5 Thin silicon membrane structures - strength and manufacturability

- Techniques were developed for the fabrication and testing of small silicon tethered membranes structures. The microfabrication techniques were centered around an increased emphasis on cleanliness during processing to minimize point defects, as well as careful inspection and covering of etched features during the final stages of deep etching.

- A testing apparatus was built, and strength numbers were obtained which were subsequently used in the design of the final energy harvester device.

8.6 Fluid filling and sealing capabilities

- Techniques were developed for reliably filling and sealing micromachined dead volumes, bubble free. By using a silicone oil that wetted the silicon surfaces well, and by using proper evacuation an purging prior to filling, a robust filling process was obtained.

- This project introduced a novel dynamic sealing technique using a flow restriction to isolate high frequency pressure fluctuations in the hydraulic amplification chambers from an external static pressure.

8.7 Microscale hydraulic amplification

- This project marked the first demonstration of hydraulic stroke amplification on the microscale.

- Good correlation with models were obtained, and it was shown that hydraulic amplification can be a stiff, compact means of stroke amplification, primarily as designed, for valve actuation, but with potential for other small-scale positioning and actuation applications.

8.8 Microvalve development

- This project presented the first hydraulically amplified piezoelectrically driven valve.

- In terms of combined pressure, flow and frequency capability, this valve addresses a niche area of applications for which until now there has not been such a device reported in the literature.

- Again, good correlation was seen with models.

- The device was limited by flow induced vibration. With a suitable geometric redesign, it should be possible to eliminate this problem.

8.9 The microfabricated energy harvester

- This project marked the fabrication of the first microfabricated piezohydraulic energy harvesting device.

- Two devices were tested and the results correlated well with model predictions. A maximum harvesting chamber power output of $1mW$ was attained at a pressure differential of $440kPa$ with the device operating at $1kHz$. This device, too, would benefit from a redesign of the active valve.

8.10 The MHT device as a bi-directional transducer

- In addition to performing harvesting testing, the device was also tested as a pump. A maximum flow rate of $4000\mu l/min$ and a maximum pressure differential of $320kPa$ was attained.

Indeed, the final MHT device is bi-directional is more than one sense: It can be operated as either a pump or as a harvester, hence having bi-directional energy flow. In addition, thanks to its active valves and the symmetric design presented here, the pump itself is also capable of delivering flow in both directions, by simply changing the phasing of the valve drive signals.

8.11 Recommendations for future work

8.11.1 Recommendations for advancement of the technologies that were developed

For the technologies and achievements mentioned in the previous sections, the following steps are recommended should future work be undertaken:

- *Modeling:* The system modeling can benefit from additional work to better understand the chosen piezoelectric material and its capabilities. An efficiency of 70% was assumed for the piezo and its circuitry, and this assumption should be better accounted for. In addition, the dynamic design of the valve needs to be revisited to design a valve that (a) has a higher first natural frequency and (b) does not have any structural modes of vibration that can couple with fluid oscillations to create an unstable operating regime below the design frequencies and pressures. This need not necessarily be accounted for in the lumped parameter model, because this redesign will ensure that the initial assumptions in the lumped system model will still hold.

- *Piezoelectric materials:* It was shown that, under high loadings, the performance of single crystal piezoelectric materials currently available deteriorates. Bearing in mind that the power output scales as the square of the stress on the piezo, more investigation into the selection of the correct

piezoelectric material is warranted. Results from [34] seem to indicate that the hard ceramic PZT-8 has a higher energy density than the single crystal materials PZN-PT and PMT-PT.

- *Bulk piezoelectric integration on the microscale:* This project has proven that there are tangible benefits to be had from using bulk piezoelectric material in a microfabricated device where superior actuation or energy conversion is needed. Therefore, it is recommended that an easier manufacturable approach for the integration of piezoelectric actuation elements be developed. A wafer-scale approach with active elements would be beneficial for a large number of small-scale actuation applications.

- *Silicone membrane fabrication:* This process needs to be improved to allow for the batch fabrication of these structures whilst maintaining good structural properties. Design changes have been proposed that involve an additional isotropic shallow etch from the SOI device side to form the fillet. A wider deep trench etch is the performed. By choosing the correct geometry, the maximum stress still occurs at the fillet, but in this case the fillet is much easier to etch.

- *Hydraulic amplification devices:* The hydraulic amplification devices can benefit from an exploration of different application prospects such as microactuation and positioning. In addition, further work is required to make the piezoelectrically driven hydraulic amplifiers self-contained in the sense that an external static pressurization is not required. Although this feature proved exceptionally useful during testing, it may not be practical for a real non-fluidic device such as a simple hydraulically amplified actuator. (In the case of a fluidic device, a design could be conceived where the dynamic seal connects directly to the low and high pressure reservoirs, hence making it self-contained).

- *Fluid filling:* The fluid filling techniques worked well for these experimental devices. However, for productions systems further refinement will be needed.

- *Microfabricated active valve:* It has been mentioned a number of times before, but the single biggest benefit from future work on the active valves would be a design effort that attempts to increase the natural frequency of this device. In addition, this device could also benefit from a good "static" sealing approach that would open a wide range of additional applications for this valve as a fast-acting, high pressure, high performance valve.

- *Energy harvesting device:* This device would benefit most from a redesign of the active valves. In addition, with the current understanding of the capabilities of available piezoelectric materials a redesign for these materials is in order.

8.11.2 Recommendations for development of additional technologies

The following aspect were not fully addressed in this project, but would need further study to enable MHT technology to become a practical technology for typical real-life applications:

- *Drive electronics:* The devices discussed in this report used conventional linear amplifiers and macro-scale drive electronics. This certainly has to change for MHT devices, and also valves and hydraulic amplifiers, to become feasible. Depending on the final voltage and current requirements that would result from a redesign of the harvesting device, suitable power electronics need to be developed to match this device.

- *Heel packaging:* Time did not permit the detailed design of a heel packaging system for the MHT harvesting device. The device presented here was designed with bench top testing considerations

in mind. A proposed development sequence would be to build a second generation bench top harvesting device, and then as a final step design a device that could be packaged into the heel of a boot.

8.12 Feasibility of MHT technology for heel strike power generation

This project has gone to great lengths to develop the core technologies that are required to produce an MHT device that can function as a power generator. In the final analysis the question of whether this technology would be feasible for heel strike power generation remains to be answered. The following aspects have to be considered:

- The device and system complexity have to be matched to their intended application. It cannot be denied that the devices presented here, in their current format, are quite complex in construction and operation, and simplifications will have to be made to make these devices feasible for use in the boot of a person. The argument that microfabrication enables the incorporation of highly complex devices into a "robust environment" does not hold for this MEMS example in the same manner as it would for e.g. a microprocessor.

- The complexity of the heel strike mechanism. In an MHT heel strike power harvesting system, the MHT forms part of a system that will incorporate a pump, a high pressure reservoir and a low pressure reservoir. Although an hydraulic system comprising of these components is relatively simple to design, it might not be feasible to have a mechanical system of such complexity in the heel of a boot.

If the above concerns can be addressed, the device presented here would serve well as a heel strike energy generating device. But even if heel strike energy generation will not be feasible using this technology, there are other potential applications for such a small, compact energy conversion device in terms of is capabilities in the role of:

- A compact discrete hydraulic energy generator

- A compact bi-directional micropump for small-scale servohydraulic actuation purposes.

In conclusion it can be said that although heel strike power generation was not achieved in this project, a number of significant technological breakthroughs have been made to provide a basis for designing and building MicroHydraulic Transducers and other high-power microelectromechanical devices that rely on these technologies.

9 References

[1] H. Van Lintel, F. van de Pol, and A. Bouwstra, "Piezoelectric micropump based on micromachining of silicon", Sensors and Actuators, 15, pp. 153-167, 1988.

[2] M. Stehr, S. Messner, H. Sandmaier, and R. Zengerle, "The VAMP - a new device for handling liquids or gases," Sensors and Actuators A, 57, pp. 153-157, 1996.

[3] V. Gass, B. van der Schoot, S. Jeanneret, and N. de Rooij, "Integrated flow-regulated silicon micropump," Sensors and Actuators A, 43, pp. 335-338, 1994.

[4] S. Shoji and M. Esashi, "Microflow devices and systems," Journal of Micromechanics and Micro-engineering, 4, pp. 157-171, 1994.

[5] K. Ikuta, T. Hasewaga, and T. Adachi, "The Optimized SMA Micro Pump Chip Applicable to Liquids and Gases," Proceedings of the 2001 International Conference on Solid-State Sensors and Actuators (Transducers '01), 2001.

[6] M. Koch, N. Harris, R. Maas, A. Evans, N. White, and A. Brunnschweiler, "Novel micropump design with thick-film piezoelectric actuation," Measurement Science and Technology, v.8 n.1, pp. 49-57, Jan 1997.

[7] P. Watler and M. Sefton, "A Piezoelectric Driven Controlled Release Micropump for Insulin Delivery," Trans Am Soc Artif Intern Organs, Vol. XXXVI, pp. 70-77, 1990.

[8] B. Wagner, H. Quenzer, S. Hoerschelmann, T. Lisec, and M. Juerss, "Micromachined bistable valves for implantable drug delivery systems," Proceedings of the 18th Annual International Conference of the IEEE Engineering in Medicine and Biology Society," pp. 254-255, 1997.

[9] N.W. Hagood, D.C. Roberts, L. Saggere, K.S. Breuer, K.-S. Chen, J.A. Carretero, H.Q. Li, R. Mlcak, S. Pulitzer, M.A. Schmidt, S.M. Spearing, and Y.-H. Su, "Micro Hydraulic Transducer Technology for Actuation and Power Generation," Proceedings of SPIE: SPIE's 7th Annual International Symposium on Smart Structures and Materials, Vol. 3985, pp. 680-688, 2000.

[10] H.Q. Li, D.C. Roberts, J.L. Steyn, K.T. Turner, J.A. Carretero, O. Yaglioglu, Y.-H. Su, L. Saggere, N.W. Hagood, S.M. Spearing, M.A. Schmidt, R. Mlcak, and K.S. Breuer, "A High Frequency High Flow Rate Piezoelectrically Driven MEMS Micropump," Proceedings of the IEEE Solid-State Sensor and Actuator Workshop, Hilton Head, SC. pp. 69-72, 2000.

[11] D.C. Roberts, J.L. Steyn, H.Q. Li, K.T. Turner, R. Mlcak, L. Saggere, S.M. Spearing, M.A. Schmidt, and N.W. Hagood, "A High-Frequency, High-Stiffness Piezoelectric Micro-Actuator For Hydraulic Applications," Proceedings of the 2001 International Conference on Solid-State Sensors and Actuators (Transducers '01), 2001.

[12] D.C. Roberts, N.W. Hagood, Y.-H. Su, H.Q. Li, and J.A. Carretero, "Design of a Piezoelectrically-Driven Hydraulic Amplification Microvalve for High Pressure, High Frequency Applications," Proceedings of SPIE's 7th International Symposium on Smart Structures and Materials, Vol. 3985, pp. 616-628, 2000.

[13] D.C. Roberts, O. Yaglioglu, J. Carretero, Y.-H. Su, L. Saggere, and N.W. Hagood, "Modeling, Design, and Simulation of a Piezoelectric Microvalve for High Pressure, High Frequency Applications," Proceedings of SPIE's 8th International Symposium on Smart Structures and Materials, Vol. 4327, 2001.

[14] J.M. Hollerbach, I.W. Hunter, J. Ballantyne, "A comparative analysis of actuator technologies for robotics," *Robotics Review* 2, Eds. Khatib and Oussama, MIT Press, pp. 299-342.

[15] J.E. Huber, N.A. Fleck, and M.F. Ashby, "The selection of mechanical actuators based on performance indices," Proceedings of the Royal Society of London, Series A, Vol. 453, No. 1965, p. 2185.

[16] S.W. Pulitzer III, "Feasability Assessment and Design of Micro Hydraulic Solid-State Transducers," MIT Master's Thesis. June 1998.

[17] S. Park and T. Shrout, "Characteristics of Relaxor-Based Piezoelectric Single Crystals for Ultrasonic Transducers," IEEE Transactions on Ultrasonics, Ferroelectrics, and Frequency Control, Vol. 44, No. 5, pp. 1140-1147, 1997.

[18] M. Esashi, S. Shoji, and A. Nakano, "Normally Closed Microvalve and Micropump Fabricated on a Silicon Wafer," Sensors and Actuators 20, pp. 163-169, 1989.

[19] M. Esashi, "Integrated Micro Flow Control Systems," Sensors and Actuators, A21-A23, pp. 161-167, 1990.

[20] S. Shoji, B. Van der Schoot, N. de Rooij, and M. Esashi, "Smallest Dead Volume Microvalves for Integrated Chemical Analyzing Systems," Proceedings of the 1991 International Conference on Solid-State Sensors and Actuators (Transducers '91), pp. 1052-1055, 1991.

[21] A.A. Ayon, K-S. Chen, K.A. Lohner, S.M. Spearing, H.H. Sawin, and M.A. Schmidt, "Deep Reactive Ion Etching of Silicon," *Materials Research Society Symposium Proceedings.* v. 546, pp.51-61, 1999.

[22] K-S. Chen, A. Ayon, and S.M. Spearing, "Controlling and Testing the Fracture Strength of Silicon on the Mesoscale," *Journal of the American Ceramic Society*, 83 [6], pp.1476-84, 2000.

[23] J.C. Arnold and H.H. Sawin, "Charging of pattern features during plasma etching," *J. Appl. Phys.*, vol. 70, no. 10, pp.5314-5317, 1991.

[24] T. Kinoshita, M. Hane, and J.P. McVittie, "Notching as an example of charging in uniform high-density plasmas," *J. Vac. Sci. Techol. B, Microelectron. Process. Phenom.*, vol. B14, no. 1, pp.560-565, 1996.

[25] T. Nowaza, T. Kinoshita, T. Nishizawa, A. Narai, T. Inoue, and A. Nakaue, "The electron charging effects of plasma on notch profile defects," *Jpn. J. Appl. Phys.*, vol. 34, pt. 1, no. 4B, pp.2107-2113, 1995.

[26] U. Gosele and Q.-Y. Tong. Semiconductor wafer bonding. *Annual Review of Materials Science*, 28, pp. 215-241, 1998.

[27] K.T. Turner, "An Evaluation of Critical Issues for Microhydraulic Transducers: Silicon Wafer Bonding, Strength of Silicon on Insulator Membranes and Gold-Tin Solder Bonding," Master's Thesis, Massachusetts Institute of Technology, Cambridge, MA, June 2001.

[28] R. Mlcak, Numerous presentations at MIT on the development of a bonding technology between piezoelectric material and silicon for use in MHT technology, 1997-2000.

[29] M. Ohring. *The Materials Science of Thin Films.* Academic Press, New York, 1992.

[30] R. Mlcak. *Wafer-scale Fluid Filling System: Standard Operating Procedure and Manual.* Document was provided to MIT from Boston Microsystems, Inc. in October 2000.

134

[31] J.L. Steyn, "Hydraulic Amplification for Actuation in MicroElectroMechanical Systems," Master's Thesis, Massachusetts Institute of Technology, Cambridge, MA, February 2002.

[32] S.E. Park and T.R. Shrout, "Characteristics of Relaxor-Based Piezoelectric Single Crystals for Ultrasonic Transducers," *IEEE Trans. Ultrasonics, Ferroelectrics, and Frequency Control, Vol.44, No.5, Sept. 1997, pp. 1140-1147.*

[33] D.C. Roberts, "Design, Modeling, Fabrication, and Testing of a Piezoelectric Microvalve for High Pressure, High Frequency Hydraulic Applications," Ph.D. Thesis, Massachusetts Institute of Technology, Cambridge, MA, February 2002.

[34] O. Yaglioglu, "Modeling and Design Considerations for a Micro-Hydraulic Piezoelectric Power Generator", S.M. Thesis, Massachusetts Institute of Technology, Cambridge, MA, June 2002.

[35] J. A. Carretero. "Measurement and Modeling of the Flow Characteristics of Micro Disc Valves". *SM Thesis, Massachusetts Institute of Technology, 2001.*

[36] S. Timoshenko. "Theory of Plates and Shells". McGraw-Hill, NewYork, NY, 1940.

[37] I.E. Idelchik. "Handbook of Hydraulic Resistance", FL, 1994

[38] Lin, Ching-Yu "Material Characterization and Modeling for Piezoelectric Actuation and Power Generation under High Electromechanical Loading", Doctoral Thesis, Massachusetts Institute of Technology, Cambridge, MA, June, 2002.

[39] B. Jaffe, W. Cook, and H. Jaffe, *Piezoelectric Ceramics,* 1971, pp. 279

[40] M. Goldfarb and L. D. Jones, "On the Efficiency of Electric Power Generation with Piezoelectric Ceramic." Journal of Dynamic Systems, Measurement, and Control. Transaction of ASME, vol. 121, September 1999, pp. 566 - 571.

135

10 Summary of Publications Generated under this Project

This section summarizes the publications that were produced as part of this project. They are attached in the appendices.

1. N.W. Hagood, D.C. Roberts, L. Saggere, M.A. Schmidt, S.M. Spearing, K.S. Breuer, R. Mlcak, J.A. Carretero, F. Ganji, H.Q. Li, K.S. Chen, Y.H. Su, S.W. Pulitzer, "Development of Micro Hydraulic Transducer Technology," *Proceedings of the 10th International Conference on Adaptive Structures and Technologies*, pp. 71-81, Paris, France, Oct. 11-13, 1999.

2. N.W. Hagood, D.C. Roberts, L. Saggere, K.S. Breuer, K.-S. Chen, J.A. Carretero, H.Q. Li, R. Mlcak, S. Pulitzer, M.A. Schmidt, S.M. Spearing, and Y.-H. Su, "Micro Hydraulic Transducer Technology for Actuation and Power Generation," *Proceedings of the SPIE 7th Annual International Symposium on Smart Structures and Materials*, Vol. 3985, pp. 680-688, Newport Beach, CA, March 5-9, 2000.

3. D.C. Roberts, N.W. Hagood, Y.-H. Su, H.Q. Li, and J.A. Carretero, "Design of a Piezoelectrically-Driven Hydraulic Amplification Microvalve for High Pressure, High Frequency Applications," *Proceedings of the SPIE 7th Annual International Symposium on Smart Structures and Materials*, Vol. 3985, pp. 616-628, Newport Beach, CA, March 5-9, 2000.

4. H.Q. Li, D.C. Roberts, J.L. Steyn, K.T. Turner, J.A. Carretero, O. Yaglioglu, Y.-H. Su, L. Saggere, N.W. Hagood, S.M. Spearing, M.A. Schmidt, R. Mlcak, and K.S. Breuer, "A High Frequency High Flow Rate Piezoelectrically Driven MEMS Micropump," *Proceedings of the IEEE Solid-State Sensor and Actuator Workshop*, Hilton Head, SC. pp. 69-72, June 4-8, 2000.

5. L. Saggere, N.W. Hagood, D.C. Roberts, H.Q. Li, J.L. Steyn, K.T. Turner, J.A. Carretero, O. Yaglioglu, Y.H. Su, R. Mlcak, S.M. Spearing, K.S. Breuer, and M.A. Schmidt, "Design, Fabrication, and Testing of a Piezoelectrically Driven High Flow Rate Micro-Pump," *Proceedings of the 12th IEEE International Symposium on the Applications of Ferroelectrics*, Honolulu, Hawaii, July 30-Aug. 2, 2000.

6. Y.H. Su and S.M. Spearing, "Large Deflection Analysis of an Annular Plate with a Rigid Boss Under Axisymmetric Loading," *Proceedings of the International Congress of Theoretical and Applied Mechanics 2000*, Chicago, IL, Aug. 29, 2000.

7. J.A. Carretero and K.S. Breuer, "Measurement and Modeling of the Flow Characteristics of Micro Disk Valves," *Proceedings of the 2000 International Mechanical Engineering Congress and Exposition: Microfluidics Symposium.* Orlando, FL, Nov. 2000.

8. D.C. Roberts, O. Yaglioglu, J. Carretero, Y.-H. Su, L. Saggere, and N.W. Hagood, "Modeling, Design, and Simulation of a Piezoelectric Microvalve for High Pressure, High Frequency Applications," *Proceedings of the SPIE 8th Annual International Symposium on Smart Structures and Materials*, Vol. 4327, pp. 366-380, Newport Beach, CA, March 4-8, 2001.

9. D.C. Roberts, J.L. Steyn, H.Q. Li, K.T. Turner, R. Mlcak, L. Saggere, S.M. Spearing, M.A. Schmidt, and N.W. Hagood, "A High-Frequency, High-Stiffness Piezoelectric Micro-Actuator For

Hydraulic Applications," *Proceedings of the 11th International Conference on Solid-State Sensors and Actuators (Transducers '01)*, Munich, Germany, pp. 686-689, June 10-14, 2001.

10. J.A. Carretero. "Measurement and Modeling of the Flow Characteristics of Micro Disc Valves", S.M. Thesis, Massachusetts Institute of Technology, Cambridge MA. February 2001.

11. K.T. Turner, "An Evaluation of Critical Issues for Microhydraulic Transducers: Silicon Wafer Bonding, Strength of Silicon on Insulator Membranes and Gold-Tin Solder Bonding." S.M. Thesis, Massachusetts Institute of Technology, Cambridge, MA, June 2001.

12. K.T. Turner, R. Mlcak, D.C. Roberts and S.M. Spearing, "Bonding of Bulk Piezoelectric Material to Silicon Using a Gold-Tin Eutectic Bond", *2001 MRS Fall Meeting*, Boston, MA.

13. Y.H. Su, K.S. Chen, D.C. Roberts, and S.M. Spearing, "Large Deflection Analysis of a Pre-Stressed Annular Plate With a Rigid Boss Under Axisymmetric Loading", *Journal of Micromech. Microeng.* 11 (2001) pp. 645-653.

14. D.C. Roberts, "Design, Modeling, Fabrication, and Testing of a Piezoelectric Microvalve for High Pressure, High Frequency Hydraulic Applications," Ph.D. Thesis, Massachusetts Institute of Technology, Cambridge, MA, February 2002.

15. D.C. Roberts, H.Q. Li, J.L. Steyn, K.T. Turner, R. Mlcak, L. Saggere, S.M. Spearing, M.A. Schmidt, and N.W. Hagood, "A High-Frequency, High-Stiffness Piezoelectric Actuator For Micro-hydraulic Applications," *Sensors and Actuators: A. Physical.* Accepted for publication.

16. O. Yaglioglu, Y.H. Su, D.C. Roberts, J. Carretero, N.W. Hagood, "Modeling, Simulation and Design of Piezoelectric Micro-Hydraulic Transducer Devices," *To be presented at the Fifth International Conference on Modeling and Simulation of Microsystems*, April 21-25, San Juan, Puerto Rico, 2002.

17. J.L. Steyn, H.Q. Li, D.C. Roberts, R. Mlcak, K.T. Turner, O. Yaglioglu, Y.-H. Su, M.A. Schmidt, S.M. Spearing, N.W. Hagood, "Hydraulic Amplification Devices for Microscale Actuation," *IEEE Solid-State Sensor and Actuator Workshop*, Hilton Head, SC, USA, 2002.

18. J.L. Steyn, "Hydraulic Amplification for Actuation in MicroElectroMechanical Systems," S.M. Thesis, Massachusetts Institute of Technology, Cambridge, MA, June 2002.

19. O. Yaglioglu, "Modeling and Design Considerations for a Micro-Hydraulic Piezoelectric Power Generator," S.M. Thesis, Massachusetts Institute of Technology, Cambridge, MA, June 2002.

20. C.-Y. Lin, "Material Characterization and Modeling for Piezoelectric Actuation and Power Generation under High Electromechanical Loading," Doctoral Thesis, Massachusetts Institute of Technology, Cambridge, MA, June, 2002.

21. H.Q. Li, D.C. Roberts, J.L. Steyn, K.T. Turner, O. Yaglioglu, N.W. Hagood, S.M. Spearing, and M.A. Schmidt, "Fabrication of a microvalve with piezoelectric actuation," *To be presented at the MEMS '03 conference*, Kyoto, Japan, 2003.

22. David C. Roberts, Hanqing Li, J. Lodewyk Steyn, Onnik Yaglioglu, S. Mark Spearing, Martin A. Schmidt, Nesbitt W. Hagood, "A Piezoelectric Microvalve for Compact High-Frequency, High Differential Pressure Hydraulic Micropumping Systems", Accepted for publication in the Journal of Microelectromechanical Systems.

11 Personnel

11.1 Principal Investigator

Hagood IV, Nesbitt W.

11.2 Faculty

Breuer, Kenny S.
Schmidt, Martin A.
Spearing, S. Mark

11.3 Scientific Staff

Atalla, Mauro J.
Li, Hanqing
Roberts, David C.
Robertson, David C.
Saggere, Laxminarayan
Su, Yu-Hsuan

11.4 Graduate Students

Carretero, Jorge A. - S.M. in Aeronautics and Astronautics
Lin, Ching-Yu - Ph.D. in Aeronautics and Astronautics
Pulitzer III, Seward W. - S.M. in Mechanical Engineering
Roberts, David C. - Ph.D. in Mechanical Engineering
Steyn, J. Lodewyk - S.M. in Aeronautics and Astronautics
Turner, Kevin T. - S.M. in Mechanical Engineering
Yaglioglu, Onnik - S.M. in Mechanical Engineering

11.5 Undergraduate Students

Bennett, David
Berte, Mark
Chang, Rick
Connelly, Blair
Daniels, Jeff
Gupta, Geeta
Gustafson, Peter A.
Hawrylchak, Michael Y.
Lu, James
Manka, Alexander K.
McKenny, Kurtis G.
Oliver, Todd

Sandoval, Daniel
Stockham, Erik

12 Patents

"Microactuator Having Amplified Actuation Stroke," by D.C. Roberts, N.W. Hagood, S.W. Pulitzer, M.A. Schmidt, H.Q. Li, J.L. Steyn, R. Mlcak, K.T. Turner, S.M. Spearing, K.S. Chen, Patent pending with United States Patent and Trademark Office. Filing Date: October 11, 2001

Appendix - Masks

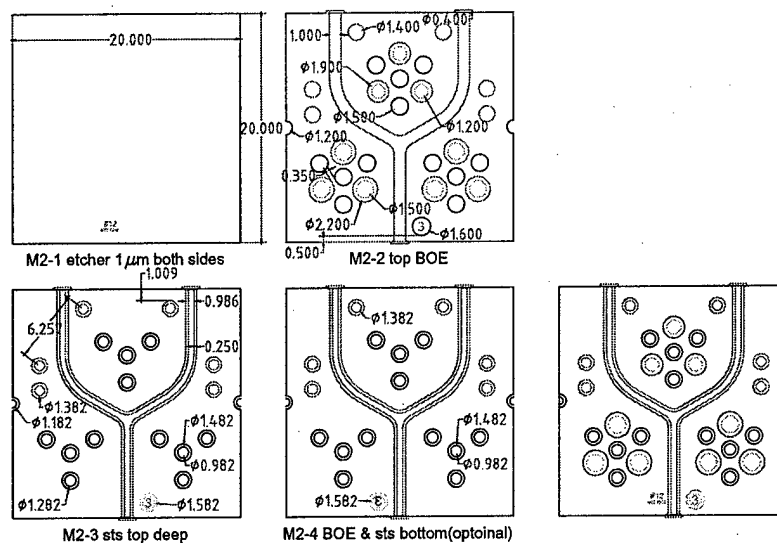This appendix contains all the masks of the MHT 10 valve device and its subcomponents.
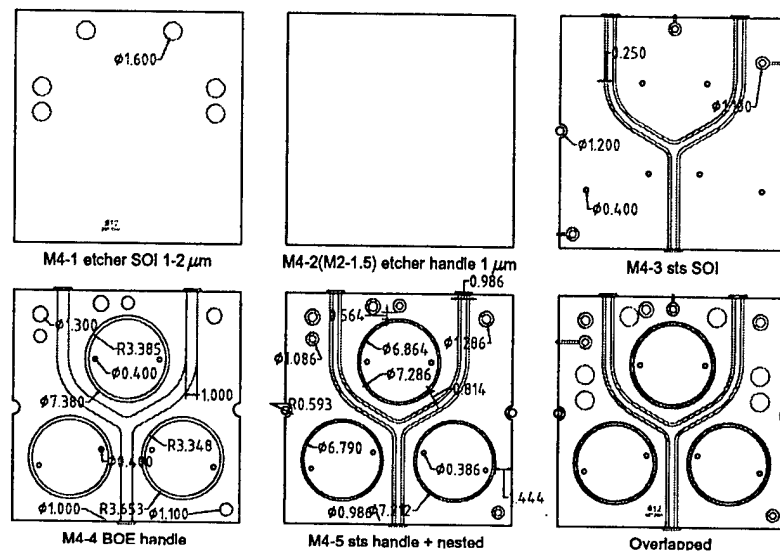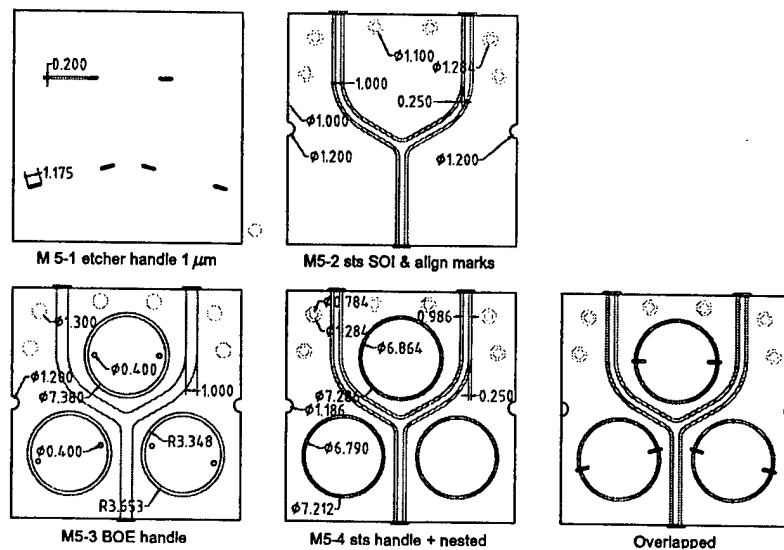

Figure 103: Layer 2 masks.

Figure 104: Layer 4 masks.
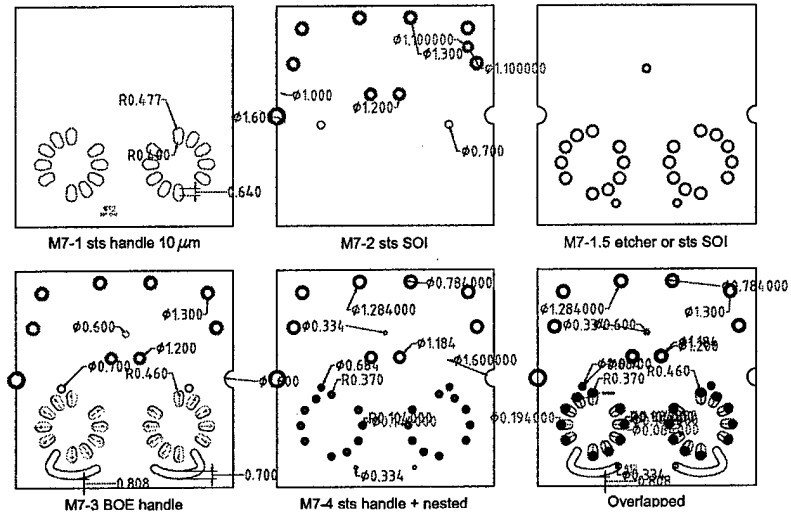

Figure 105: Layer 5 masks.

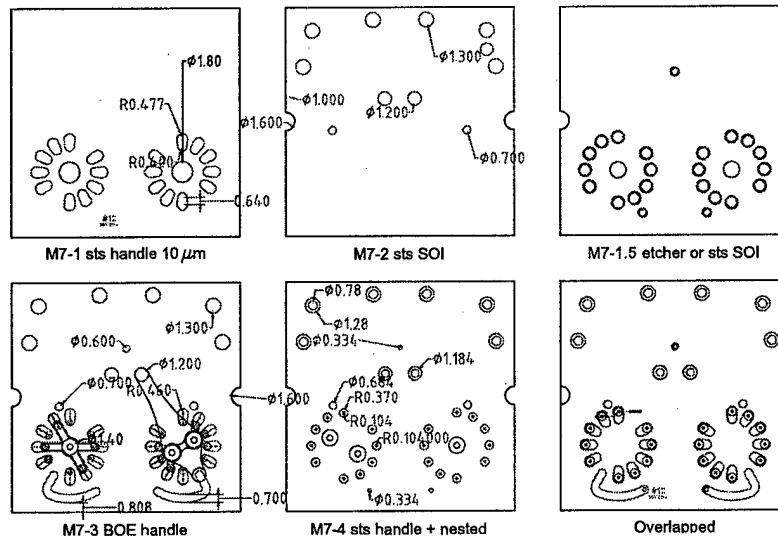Figure 106: Layer 7 masks. MHT device with 10 small valves per valve unit

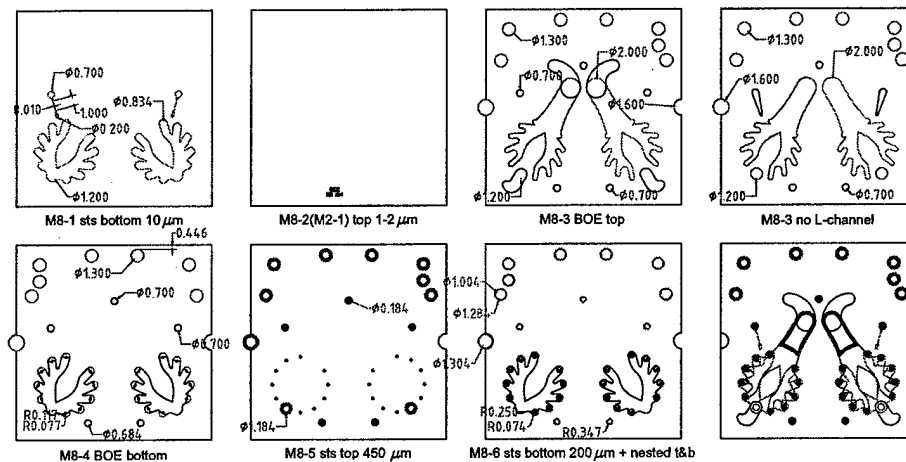Figure 107: Layer 7 masks. MHT subcomponents with 1, 2 and 10 valve devices.

Figure 108: Layer 8 masks. MHT device with 10 small valves per valve unit

Figure 109: Layer 8 masks. MHT subcomponent device with 10 small valves per valve unit. The only difference is the inlet and outlet hole positions.

148

Figure 110: Layer 8 masks. MHT subcomponent device with 10 small valves per valve unit. This device has two discrete valve test units, and cannot function as a harvester.
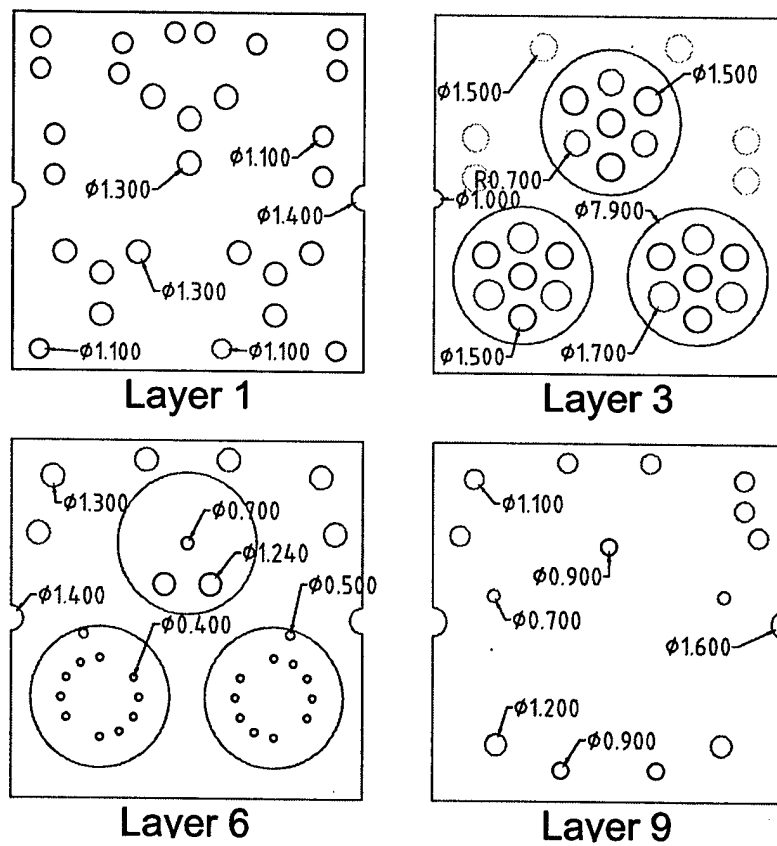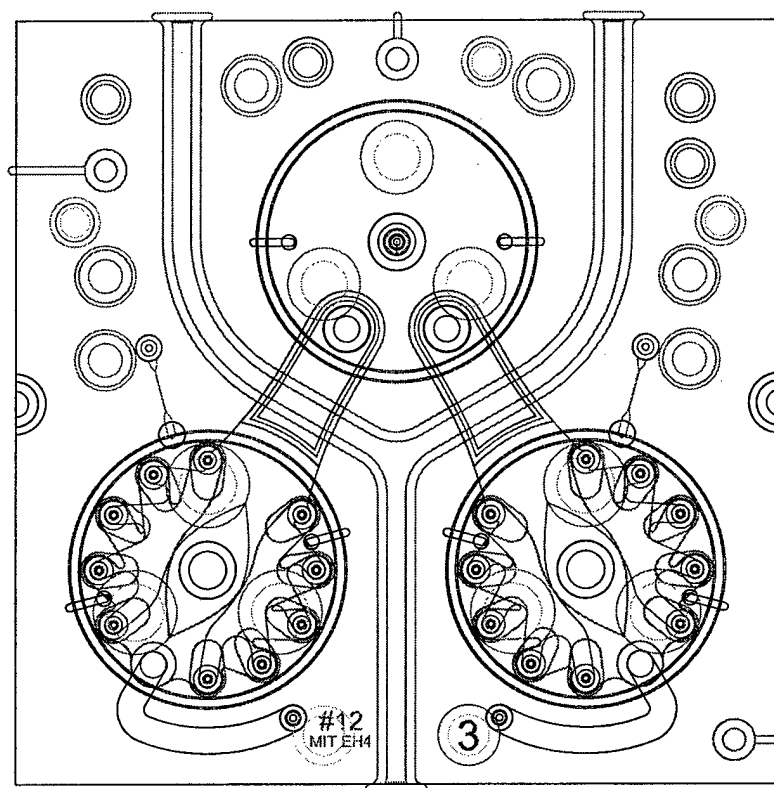
Figure 111: Glass layer masks.

Overlapped

Figure 112: Overlay of all the masks of the MHT device